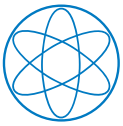

Technische Universität München

Max-Planck-Institut für Plasmaphysik

The role of the radial electric field in the development of the edge transport barrier in the ASDEX Upgrade tokamak

Marco Cavedon

Vollständiger Abdruck der von der Fakultät für Physik der Technischen Universität München zur Erlangung der akademischen Grades eines

Doktors der Naturwissenschaften

genehmigten Dissertation.

Vorsitzender:	Prof. Dr. Björn Garbrecht
Prüfer der Dissertation:	1. Prof. Dr. Ulrich Stroth
	2. Prof. Dr. Aliaksandr Bandarenka

Die Dissertation wurde am 06.04.2016 bei der Technischen Universität München eingereicht und durch die Fakultät für Physik am 18.05.2016 angenommen.

DEPARTMENT OF PHYSICS
TECHNISCHE UNIVERSITÄT MÜNCHEN

The role of the radial electric field in the development of the edge transport barrier in the ASDEX Upgrade tokamak

Marco Cavedon

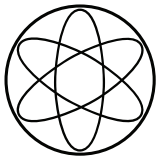

DEPARTMENT OF PHYSICS
TECHNISCHE UNIVERSITÄT MÜNCHEN

The role of the radial electric field in the development of the edge transport barrier in the ASDEX Upgrade tokamak

Author:	Marco Cavedon
Supervisor:	Univ.-Prof. Dr. U. Stroth
Advisors:	Priv.-Doz. Dr. T. Pütterich
	Dr. E. Viezzer
Submission Date:	11th March 2016

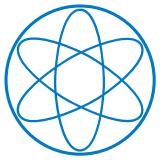

Abstract

The release of fusion power exceeds the power required to produce and confine the plasma if approximately the product of density n, temperature T and energy confinement time τ_E is greater than $nT\tau_\mathrm{E} \gtrsim 3 \times 10^{21}\,\mathrm{keVs/m^3}$. While the maximum attainable pressure is limited by instabilities, the fusion capability of magnetically confined plasmas will be largely improved if they can operate in the high confinement regime (H-mode), where τ_E is a factor of two larger compared to the low confinement mode (L-mode). The transition from L- to H-mode correlates with the generation of an edge transport barrier (ETB) which gives rise to steep gradients in the edge plasma profiles, thus enhancing particle and energy confinement. It is widely accepted that the $\mathbf{E}\times\mathbf{B}$ velocity shear is responsible for the suppression of the edge turbulence, thus leading to the formation of the ETB. However, the origin and the evolution of the edge radial electric field (E_r) profile and the accompanying $\mathbf{E}\times\mathbf{B}$ flow is still debated. The $\mathbf{E}\times\mathbf{B}$ flow may be generated by turbulence stresses or collisional (neoclassical) processes via the main ion pressure gradient. A better understanding of the interplay between macroscopic flows, edge profile gradients and turbulence is of crucial importance to enable a better control of the L–H transition and the transport at the plasma edge.

In order to study the evolution of the edge gradients and flows, the edge charge exchange recombination spectroscopy (CXRS) diagnostic has been upgraded during this work. A new high temporal and spatial resolution CXRS system has been designed and installed at the outboard midplane of the ASDEX Upgrade tokamak. The diagnostic provides a full reconstruction of the impurity density, temperature and flow profiles with unprecedented temporal resolution ($\approx 50\,\mu\mathrm{s}$). These data allow the reconstruction of the E_r profile. The fast time resolution is fundamental for investigating fast transient phenomenas such as the L–H transition or edge localized modes (ELMs) and this work provides new insights into the spatio-temporal dynamics of the L–H transition and ELMs.

The relation between the macroscopic input power required to access the H-mode and the microscopic $\mathbf{E}\times\mathbf{B}$ shear has been investigated at various toroidal magnetic fields, different electron densities, and in both hydrogen and deuterium plasmas. For the H-mode onset, a threshold in the $\mathbf{v}_{\mathrm{E}\times\mathrm{B}}$ minimum, a proxy of the $\mathbf{E}\times\mathbf{B}$ flow shear, has been found across the whole database. This suggests that the ion channel plays a key role in the L–H transition physics and identifies $\mathbf{v}_{\mathrm{E}\times\mathrm{B}}$ and not E_r as the important player for the H-mode onset.

The fast dynamics of $\mathbf{v}_{\mathrm{E}\times\mathrm{B}}$ and the ion profiles are compared in time scales of 100 µs during different phases of the L–H and H–L transition process. In the radial force balance, the main ion pressure gradient is found to be the dominant contribution to the total $\mathbf{E}\times\mathbf{B}$ flow, supporting the idea that $\mathbf{v}_{\mathrm{E}\times\mathrm{B}}$ is mostly established by neoclassical processes. As a conclusion, the turbulence induced flow may play a role on timescales shorter than 100 µs or must be phase locked into the neoclassical flow. Thus, the neoclassical flow could actively contribute to turbulence shear. The experimental findings obtained in this work reveal the fundamental role of the main ion pressure gradient in the L–H transition physics.

Moreover, ELMs were investigated and, for the first time, the recovery of the ion and electron channel after the ELM crash could be compared. The ion temperature gradient is re-established on similar timescales as the electron density (≈ 4 ms), whereas the electron temperature gradient recovery takes longer (≈ 7 ms). The radial electric field profile is also restored to the pre-ELM profile in about 4 ms and the comparison with the neoclassical prediction shows again good agreement within the experimental uncertainties.

Zusammenfassung

Das Freiwerden von Fusionsleistung übertrifft die zum Erzeugen und Einschließen des Plasmas benötigte Leistung, wenn nahërungsweise das Produkt aus Dichte n, Temperatur T und Energieeinschlusszeit τ_E größer ist als $nT\tau_\mathrm{E} \gtrsim 3 \times 10^{21}\,\mathrm{keVs/m^3}$. Der maximal erreichbare Druck ist zwar durch Instabilitäten beschränkt, jedoch kann τ_E durch den Übergang zu einem Regime hohen Einschlusses (H-Mode) im Vergleich zum Regime niedrigen Einschlusses (L-Mode) verdoppeltet werden. Der Übergang von der L- zur H-Mode korreliert mit dem Entstehen einer Randtransportbarriere, die zu steilen Gradienten in den Randplasmaprofilen führt und damit den Teilchen- und Energieeinschluss verbessert. Es ist allgemein akzeptiert, dass die verscherte $\mathbf{E}\times\mathbf{B}$ Plasmaströmung für die Unterdrückung der Randturbulenz verantwortlich ist und damit zum Entstehen der Randtransportbarriere führt. Der Ursprung und die Entwicklung des radialen elektrischen Feldes (E_r) am Rand ist jedoch nach wie vor umstritten. Die $\mathbf{E}\times\mathbf{B}$ Plasmaströmung kann durch turbulente Spannungen auf das Fluidelement oder durch kollisionale (neoklassische) Prozesse über den Hauptionendruckgradienten verursacht werden. Ein besseres Verständnis des Wechselspiels zwischen makroskopischen Strömungen, Randprofilgradienten und Turbulenz ist von entscheidender Bedeutung um eine bessere Kontrolle des L–H Übergangs und des Plasmarandtransports zu ermöglichen.

Um die Entwicklung der Randgradienten und der Plasmaströmungen zu untersuchen wurde die Randladungsaustauschspektroskopie-Diagnostik während dieser Arbeit verbessert. Ein neues System mit hoher zeitlicher und räumlicher Auflösung wurde an der äußeren Mittelebene des ASDEX Upgrade Tokamaks installiert. Es erlaubt eine vollständige Rekonstruktion der Verunreinigungsdichte, der Temperatur und des Strömungsprofils mit noch nie dagewesener Zeitauflösung ($\approx 50\,\mu\mathrm{s}$). Mithilfe des radialen Kraftgleichgewichts kann das E_r Profil direkt aus den Messdaten bestimmt werden. Die schnelle zeitliche Auflösung ist eine Voraussetzung für die Untersuchung von transienten Phänomenen wie dem L–H Übergang oder randlokalisierten Moden (ELMs). Diese Arbeit liefert neue Einblicke in die räumliche und zeitliche Dynamik des L–H Übergangs und der ELMs.

Das Verhältnis zwischen makroskopischer Eingangsleistung, die benötig wird um in die H-Mode zu gelangen und der mikroskopischen $\mathbf{E}\times\mathbf{B}$ Verscherung wurde bei verschiedenen toroidalen Magnetfeldern und Elektronendichten in Wasserstoff- und Deuteriumplasmen untersucht. In der gesamten Datenbank wurde für den Übergang in die H-mode ein Schwellenwert im $\mathbf{v}_{\mathrm{E}\times\mathrm{B}}$ Minimum gefunden. Dies deutet darauf hin, dass der Ionenkanal

eine Schlüsselrolle in der Physik des L–H Übergangs spielt und dass $\mathbf{v}_{\mathrm{E}\times\mathrm{B}}$ und nicht E_r selbst wichtig ist für den Übergang in die H-Mode.

Die schnelle Dynamik von $\mathbf{v}_{\mathrm{E}\times\mathrm{B}}$ und der Ionenprofile wurde in verschiedenen Phasen des L-H und H-L Übergangs untersucht. Es konnte experimentell nachgewiesen werden, dass der Hauptionendruckgradient der dominante Beitrag für die $\mathbf{E}\times\mathbf{B}$ Strömung ist. Dies unterstützt die Hypothese, dass $\mathbf{v}_{\mathrm{E}\times\mathrm{B}}$ vor allem durch neoklassische Prozesse hervorgerufen wird. Die durch Turbulenz erzeugten Strömungen können auf Zeitskalen kürzer als 100 µs relevant sein oder sie sind an die neoklassische Strömung phasengekoppelt. Die experimentellen Ergebnisse dieser Arbeit zeigen, dass der Druckgradient der Hauptionen-Spezies eine entscheidende Rolle in der Physik des L-H Übergangs spielt.

In dieser Arbeit wurden auch ELMs untersucht und zum ersten Mal konnte das Verhalten der Ionen- und Elektronenprofile am Plasmarand während dem ELM-Zyklus verglichen werden. Der Ionentemperaturgradient wird auf ähnlichen Zeitskalen (≈ 4 ms) wie die des Elektronendichtegradienten aufgebaut, im Gegensatz zum Aufbau des Elektronentemperaturgradienten (≈ 7 ms). Das radiale elektrische Feld baut sich auch innerhalb von ≈ 4 ms wieder auf und zeigt innerhalb der Messungenauigkeiten eine sehr gute Übereinstimmung mit der neoklassischen Vorhersage.

Contents

1 Introduction

The present world economic system intrinsically requires ever-increasing amounts of energy to maintain economy raise, increase living standards, and reduce poverty. But today's energy consumption rates are not sustainable. As the total world's population grows and economies become more industrialized, nonrenewable energy sources are inevitable becoming scarcer and therefore more expensive. While an alternative system would limit the energy demand, it is clear that an option for producing energy featuring limited ecological impact and large availability is highly attractive. The controlled nuclear fusion has the potential to provide such an alternative.

Nuclear fusion is a reaction where two nuclei fuse to form a heavier nucleus. The nuclear rearrangement results in a reduction of the total mass and consequently in release of energy. In particular, the especially low mass of ^{4}He compared to his unbound constituents of the nucleus yields to one of the largest energy gain. On Earth, the ^{4}He most prominent reagents are deuterium (D) and tritium (T) whose cross-section σ is already relatively large at energies of 20–30 keV:

$$^2_1\mathrm{D} + ^3_1\mathrm{T} \longrightarrow ^4_2\mathrm{He} + \mathrm{n} + 17.6\,\mathrm{MeV} \tag{1.1}$$

High kinetic energy is required to overcome the Coulomb potential enabling the strong interaction. Due to the large Coulomb cross section, a beam–target concept can not achieve net energy gain. The scattering of the accelerated ions with mostly electrons transfers energy into the thermal velocities, while the fusion reactions are small. Hence, a confined, thermalized plasma at high temperature in the range of 10–30 keV, such that a considerable fraction of collisions leads to fuse, is a more promising approach. The advantage of the D−T fusion in comparison with other reactions is illustrated in figure 1.1 where reaction rates coefficients $\langle \sigma v \rangle$ of different reactions, i.e. the Maxwellian average of the velocity-weighted cross-section, are presented. At this temperature atoms can be partially or fully ionised resulting in a high temperature plasma. To achieve self-sustained fusion reactions the plasma has to be confined in order to minimize particle and energy losses. A figure of merit of fusion energy production based on power balance consideration is the Lawson criterion [1] which defines plasma properties for the fusion ignition, i.e. for a self sustained fusion plasma: $n\,T\,\tau_E > 3 \times 10^{21}\,\mathrm{m}^{-3}\,\mathrm{keV\,s}$, where n is

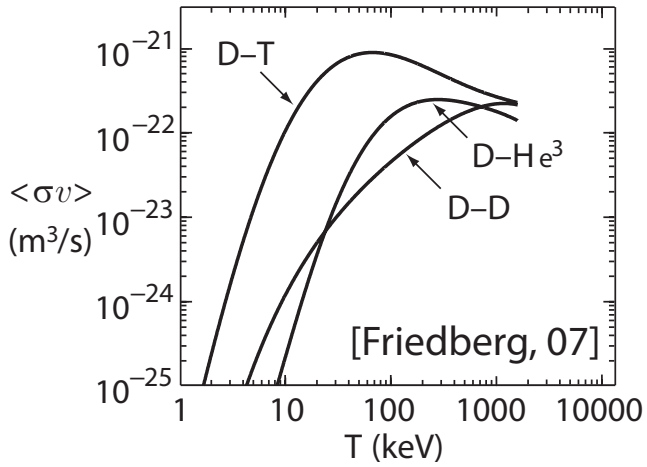

Figure 1.1: Fusion reaction rates for different reactions as a function of the ion energy (adapted from [3])

.

the plasma density, T is the plasma temperature and τ_E the energy confinement time. The range of acceptable temperatures is clearly defined by the cross-section whereas the choice of n and τ_E depends on the used confinement technique. All sort of technical solutions can be adopted to fulfill the Lawson criterion and a variety of approaches have been attempted at professional and amateur level. The major division is between inertial confinement and magnetic confinement. In inertial confinement fusion, small D−T ice pellets are isotropically and homogeneously heated by lasers or ion beams leading to a compression and a fast ignition which provide at the same time confinement and heating [2].

In magnetic confinement fusion, strong magnetic field are used to counteract the hot plasma expansion by means of the Lorentz force [3].

At present, the device which is regarded as the most promising solution for a future fusion reactor is the tokamak. This thesis was carried out on a tokamak device with main focus on its confinement regimes.

1.1 The tokamak confinement regimes

The tokamak is a magnetic confinement fusion concept where particles are confined on magnetic field lines closed in a torus shape. Figure 1.2 illustrates a schematic of a tokamak device. Here, the toroidal magnetic field B_ϕ intrinsically presents a radial gradient resulting in losses perpendicular to the magnetic field due to the ∇B-drift. This can be avoided by inducing a current into the plasma, I_p, to generate a poloidal

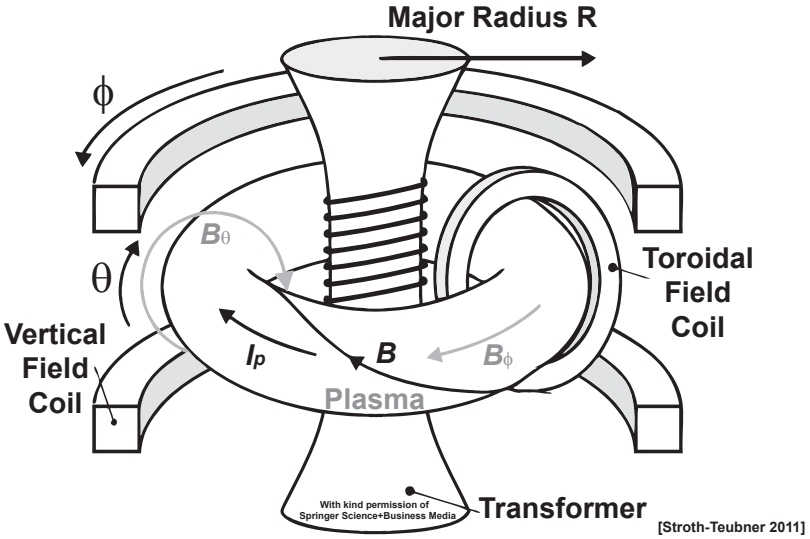

Figure 1.2: Schematic of the minimum requirement for a tokamak device: the toroidal field coils produce the toroidal field B_ϕ, while the poloidal field B_θ is generated by the induced plasma current I_p (adapted from [4]).

field, B_θ, thus leading to helical field lines. Thus, the ∇B-drift, which has a constant direction (either upward or downward), causes a drift away from plasma column center for particles below/above the plasma center, whereas particle above/below the center drift away. Hence, the ∇B-drift is averaged out. Finally, vertical field coils are required to prevent the radial expansion of the plasma and to compensate the force due to the radial B_ϕ gradient.

The plasma topology in a tokamak is defined by the magnetic field geometry. The normalized poloidal flux ρ_{pol} can be used to label the magnetic flux surfaces:

$$\rho_{\mathrm{pol}} = \sqrt{\frac{\Psi - \Psi_{\mathrm{axis}}}{\Psi_{\mathrm{separatrix}} - \Psi_{\mathrm{axis}}}} \tag{1.2}$$

where Ψ is the poloidal magnetic flux, $\Psi_{\mathrm{separatrix}}$ corresponds to the poloidal flux at the last closed flux surface (LCFS) and Ψ_{axis} is the poloidal flux at the magnetic axis. ρ_{pol} ranges from $\rho_{\mathrm{pol}} = 0$ in the plasma center to $\rho_{\mathrm{pol}} = 1$ at the LCFS, also called separatrix. The major radius R can also be used as a geometric coordinate and describes the distance from the toroidal axis of symmetry (figure 1.2). This thesis was performed at the ASDEX[1] Upgrade (AUG) tokamak which is a mid-size device located at the Max Planck Institute for Plasma Physics in Garching, Germany.

[1] Axial Symmetric Divertor EXperiment

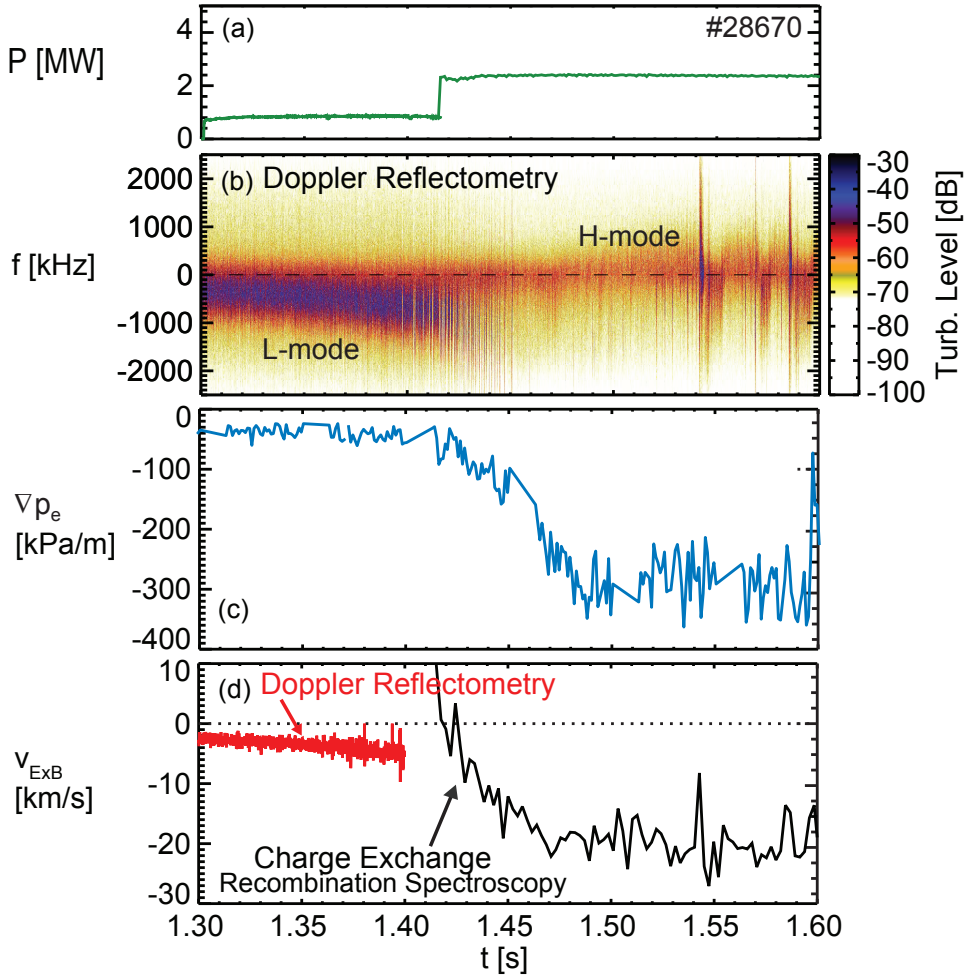

Figure 1.3: Discharge evolution from L-mode to H-mode at ASDEX Upgrade: (a) input power P, (b) spectrogram of the Doppler reflectometry (DR) signal: dark colors indicate a stronger turbulence amplitude, (c) edge electron pressure gradient, (d) $\mathbf{v}_{\mathrm{E}\times\mathrm{B}}$ from DR (red) and from the charge exchange recombination diagnostic (black) (adapted from [5]).

In 1982 a regime of improved confinement, the high confinement mode (H-mode), was described for the first time [6]. The importance of the H-mode was clear from the very beginning: the energy confinement time is about a factor of two higher compared to that in the low-confinement mode (L-mode). Energy, particle and momentum transport losses are reduced simultaneously at the L–H transition making this regime highly favourable for a reactor. The plasma spontaneously transits from L-mode into H-mode above a certain input heating power threshold, more explanation in section 2.4. This threshold has a scaling based on a database which includes the most world wide relevant tokamaks and is used to predict the L–H power threshold P_{thr} and thus sets one of the

design requirements for future devices. A physics based model could offer more reliable predictions, but the understanding of the L–H transition physics is still incomplete. The H-mode correlates with the establishment of an edge transport barrier (ETB) where turbulence is strongly reduced and a steep pressure gradient builds up. It is widely accepted that the $\mathbf{E}\times\mathbf{B}$ drift velocity ($\mathbf{v}_{\mathrm{E}\times\mathrm{B}} = (\mathbf{E}\times\mathbf{B})/B^2$) shear is responsible for the reduction of the edge turbulence, thus sustaining the ETB [7]. However, this does not explain the most important challenge of the H-mode physics: the abrupt shearing of the edge turbulence takes place while its driving force – the gradients – increases. The evolution of an AUG discharge from L-mode to H-mode is illustrated in Figure 1.3. While the input power P is increased (a), the plasma transits from a high turbulent regime (L-mode) to an H-mode where turbulence is strongly reduced (b). Here, the turbulence amplitude is measured by Doppler reflectometry (DR) and in the spectrogram of the reflected microwave signal (figure 1.3(b)) dark colors indicate a higher turbulence amplitude. At the same time, the electron pressure gradient ∇p_e at the edge of the plasma steepens up (c) while the $\mathbf{E}\times\mathbf{B}$ flow gets stronger (d). The $\mathbf{v}_{\mathrm{E}\times\mathrm{B}}$ velocity is measured by two different diagnostics, the charge exchange recombination spectroscopy diagnostics (CXRS, black) and DR (red), whereas ∇p_e is obtained from a combination of the data from different diagnostics according to the integrated data analysis algorithm (IDA). Details about the diagnostics are given in chapter 3.

In the past years, several theories have been developed to explain the L–H transition, however, the underlying physics mechanism which drives the radial electric field is still an open issue. This calls for an improvement of the diagnostics monitoring the three essential players in the L–H transition physics at the plasma edge: (i) the turbulence, (ii) the flows and (iii) the profile gradients. In particular high temporal and spatial resolution are required since the edge transport barrier extends only about 2 cm at AUG [8] and the timescale of the L–H transition is around 100 µs [9].

1.2 Thesis goals and outline

To address the spatio-temporal interaction between turbulence, flows and profile gradients, the edge charge exchange recombination spectroscopy diagnostic (CXRS) at ASDEX Upgrade has been upgraded in the framework of this thesis. This diagnostic provides localized measurements of impurity ion flows v_α, temperature T_α, and density n_α. While the main plasma component is deuterium, impurities are present in small contribution and sometimes added to improve the diagnostic capabilities. By measuring the poloidal (θ) and toroidal (ϕ) projections of the impurity ion velocity, it is possible

to determine the radial electric field E_r, i.e. $\mathbf{v}_{\mathrm{E}\times\mathrm{B}}$, through the radial force balance:

$$E_r = \mathbf{v}_{\mathrm{E}\times\mathrm{B}} \cdot \mathbf{B} = \frac{\nabla_r p_\alpha}{e Z_\alpha n_\alpha} - v_{\theta,\alpha} B_\phi + v_{\phi,\alpha} B_\theta \tag{1.3}$$

where Z_α is the charge number and e the elementary charge. Fifty-two newly installed lines of sight (LOS) provide a full characterization of the edge profiles while a new spectrometer, developed as part of this work, allows to acquire nine channels at a maximum acquisition rate of 20 kHz. This new setup, combined with the other edge diagnostics at AUG, gives the opportunity to understand the underlying physics of the L–H transition.

In **Chapter 2**, an introduction to the background theory on the plasma transport and flows is given, illustrating the turbulence shearing mechanism. The possible contributions to $\mathbf{v}_{\mathrm{E}\times\mathrm{B}}$ are discussed and the neo-classical approximation of E_r and the zonal flow generation is described. A brief introduction of the latest L–H transition theories is given. **Chapter 3** describes a description of the AUG diagnostics used in this work while in **Chapter 4** a detailed characterization of the edge CXRS system is presented. Here, upgraded system is described and the design of the new spectrometer is illustrated. **Chapter 5** is devoted to the study of the background condition for the H-mode onset. The relation between the L–H transition power threshold and the $\mathbf{v}_{\mathrm{E}\times\mathrm{B}}$ shear is investigated experimentally. In **Chapter 6** the fast dynamics of the L–H transition is presented. Here, the fluctuations observed close to the L–H transition are characterized and possible triggering mechanism are studied. **Chapter 7** investigates the dynamics of the edge profiles and of the radial electric field through an edge localized mode cycle. A comparison between the evolution of the ion and the electrons is presented. In **Chapter 8** the results of this work are summarized and proposals for future work are outlined.

2 Background of the L–H transition

The $\mathbf{E}\times\mathbf{B}$ velocity and its associated shear are believed to be responsible for the turbulence shear at the plasma edge and thus connected to L–H transition physics. In this chapter, the explicit relation between the plasma flows, the profile gradient and the $\mathbf{E}\times\mathbf{B}$ velocity is derived and the mechanisms of the turbulence shearing is discussed. The general features of the H-mode are discussed and a short overview of the L–H transition models is given.

2.1 Transport processes in a fusion plasma

2.1.1 Guiding centre approximation

The starting point for the development of a description for the plasma confinement is the guiding centre approximation and in particular the equations of motion. For plasma physics applications only the magnetic and electric forces, given by the Lorentz force are required whereas gravity can be neglected. The equations to be solved are:

$$m_\alpha \frac{d\mathbf{v}}{dt} = q_\alpha(\mathbf{E} + \mathbf{v}\times\mathbf{B}) \qquad \frac{d\mathbf{r}}{dt} = \mathbf{v}. \tag{2.1}$$

where $\mathbf{E} = \mathbf{E}(\mathbf{r}, t)$, $\mathbf{B} = \mathbf{B}(\mathbf{r}, t)$, and m_α and q_α are mass and charge of the particle. The basic idea of magnetic confinement can be understood from the behaviour of a charged particle in a uniform, time independent, magnetic field, i.e. $\mathbf{E} = 0$ and $\mathbf{B} = B\mathbf{e_z}$, where $B = \text{const}$. The resulting orbit corresponds to a helical trajectory where the particles exhibit good confinement perpendicular to the magnetic field and no confinement parallel to it. The gyro-frequency (or cyclotron frequency) $\omega_{c,\alpha}$ and the gyro-radius $r_{L,\alpha}$ (also called Larmor radius) of a particle around the magnetic field line are:

$$\omega_{c,\alpha} = \frac{|q_\alpha|B}{m_\alpha} \qquad r_{L,\alpha} = \frac{v_{\perp,\alpha}}{\omega_{c,\alpha}} = \frac{m_\alpha v_{\perp,\alpha}}{|q_\alpha|B} \tag{2.2}$$

where $v_{\perp,\alpha}$ is the velocity component perpendicular to the magnetic field. The gyro motion of charged particles in a static, homogeneous magnetic field serves as the basic building block for magnetic confinement of a fusion plasma. Typically, the centre of

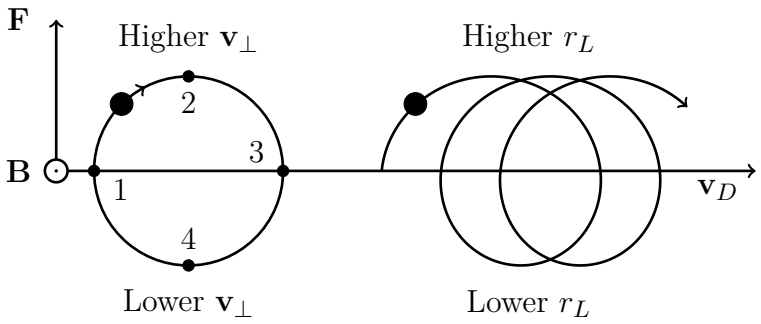

Figure 2.1: Schematic of the effect of a force **F** perpendicular to **B** on the particle gyro-motion: on average $\mathbf{v}_\perp$, and consequently r_L, is higher in upper part of the plot than in the lower part. This generates the guiding centre drift. (adapted from [3])

gyration and not the gyro-motion is of interest and the corresponding approximation, which ignores the gyro-motion, is called guiding centre approximation.

Plasma drifts

In addition to the static magnetic field there are different terms which can contribute to the equation of motion (2.1). In particular, any driving term representing a constant acceleration $\mathbf{F}/m$ with a component perpendicular to the magnetic field gives rise to a drift [3]. A physical picture of this effect can be deduced from figure 2.1. As a particle moves from point 1 to point 2, due to the force **F**, it is accelerated and therefore its gyro-radius is increased (see equations (2.2)). On the other hand, while it moves from point 2 to point 3 it slows down to the original velocity. These effects are mirrored in the motion of the particle from point 3 to point 1 but the overall $v_\perp$ is smaller compared to the original perpendicular velocity whereas from point 1 to point 3 it is always higher. The difference in the averaged r_L leads to a drift perpendicular to both **B** and **F** and the general form is given by the expression:

$$\mathbf{v}_D = \frac{\mathbf{F} \times \mathbf{B}}{q_\alpha B^2}. \tag{2.3}$$

In the following section the most relevant drifts for this work are discussed: the **E**×**B** drift, the ∇B-drift, the curvature drift and the diamagnetic drift.

In addition to the constant magnetic field in equations (2.1), a constant electric field **E** is introduced. The resulting drift velocity, also called **E**×**B** velocity, is:

$$\mathbf{v}_{\mathrm{E}\times\mathrm{B}} = \frac{\mathbf{E} \times \mathbf{B}}{B^2}. \tag{2.4}$$

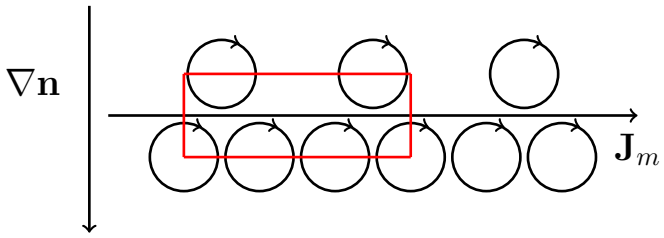

Figure 2.2: Schematic of the magnetization current $\mathbf{J_m}$ generation: due to ∇n there are more particle gyrating to right than to the left causing a net current $\mathbf{J}_{\text{dia}}$.

Note that since electrons and ions have the same $\mathbf{v}_{\text{E}\times\text{B}}$ this corresponds to a macroscopic fluid flow, without any generation of current. It is however not straightforward to demonstrate why a perpendicular electric field with spatial scales larger than the plasma quasi-neutrality can exist. This requires the solution of a self-consistent plasma model shown in section 2.3. The $\mathbf{E}\times\mathbf{B}$ velocity is considered to be responsible for the turbulence suppression at the plasma edge and consequently of the H-mode onset. Details on the shearing mechanism are given in section 2.2.

As mentioned in chapter 1, the tokamak configuration intrinsically presents a gradient in the magnetic field opposite to the R direction. Recalling that $r_L \sim v_\perp / B$, ∇B acts in modifying the gyro-motion leading to a drift due to the same mechanism as shown in figure 2.1. The resulting generalized 2-D ∇B-drift is:

$$\mathbf{v}_{\nabla B} = -\frac{m_\alpha v_{\perp,\alpha}^2}{2q_\alpha}\frac{\nabla B \times \mathbf{B}}{B^3}. \tag{2.5}$$

The ∇B drift makes an important contribution to the flow of current and the associated self-consistent magnetic field in a fusion plasma.

The field line curvature also leads to a guiding centre drift perpendicular to both curvature and field. The drift arises from the centrifugal force due to free streaming of particles along curved field lines and is therefore called curvature drift:

$$\mathbf{v}_{k,\alpha} = -\frac{m_\alpha v_{\parallel,\alpha}^2}{q_\alpha B^3}\nabla B \times \mathbf{B}. \tag{2.6}$$

In addition to the guiding centre drifts, fluid drifts can be found in a plasma. The fluid velocity is defined by a certain particle flow passing through a certain area. In case of an asymmetry in the counting a drift could arise. One of these is the diamagnetic drift $\mathbf{v}_{\text{dia},\alpha}$. The origin of $\mathbf{v}_{\text{dia},\alpha}$ is illustrated in figure 2.2. Note that the particles do not experience any guiding centre drift, i.e. they are not displaced by $\mathbf{v}_{\text{dia},\alpha}$. However, due to the density gradient in given a volume (red box) there are more particles rotating

to the right than to the bottom. This results in a net current, called magnetization current $\mathbf{J_m}$. Temperature gradients also cause a magnetization current since hotter particles have a higher velocity than colder particles. The general formula for the diamagnetic drift is:

$$\mathbf{v}_{\mathrm{dia},\alpha} = -\frac{\nabla p_\alpha \times \mathbf{B}}{q_\alpha n_\alpha B^2} \tag{2.7}$$

where p_α is the pressure of the considered species α and n_α the density. In conclusion, a gradient in the pressure causes a macroscopic drift even though none of the particles needs to have a guiding centre drift.

2.1.2 Collisional and Turbulent Transport

The most obvious source of radial transport in a magnetically confined plasma are the Coulomb collisions. Here, radial transport means a displacement of a particle perpendicular to the magnetic field. The classical transport is due to Coulomb collisions affecting the movement of the guiding center of the particle while the neoclassical transport includes the geometry, i.e. the collisions in a toroidal magnetic confinement system.

Binary collisions can be modelled as a random-walk diffusion process. The typical scale length (Δx) is given by the Larmor radius while the collision time τ – the inverse of the collisional frequency ν – is used as the characteristic time scale (Δt). Therefore the classical diffusion coefficient is given by [10]:

$$D_{\mathrm{classical}} = \frac{(\Delta x)^2}{2\Delta t} = \frac{r_L^2}{2\tau} = \frac{r_L^2 \nu}{2}. \tag{2.8}$$

The main effect of the toroidal geometry in terms of transport is the possibility of a particle to get trapped in a magnetic mirror due to ∇B along the field lines [11]. The orbits of the trapped particles are usually called banana orbits due to their typical shape on the poloidal plane. Collisions act as a de-trapping process and therefore different regimes are established depending on the collisional frequency and on the field line geometry. A convenient scaling parameter for the different regimes is the collisionality:

$$\nu_* = \frac{\nu}{2\,\epsilon\,\omega_b} = \frac{\nu q_s R}{\epsilon^{3/2} v_{th}} \tag{2.9}$$

where $\epsilon = r/R$ is the inverse of the aspect ratio, $q_s = m/n$ is the safety factor, ω_b the trapped particle bounce frequency and v_{th} is the thermal velocity[1]. The low collisionality

[1] Here, r is the minor radius, R the major radius, n and m the number of toroidal and poloidal turns

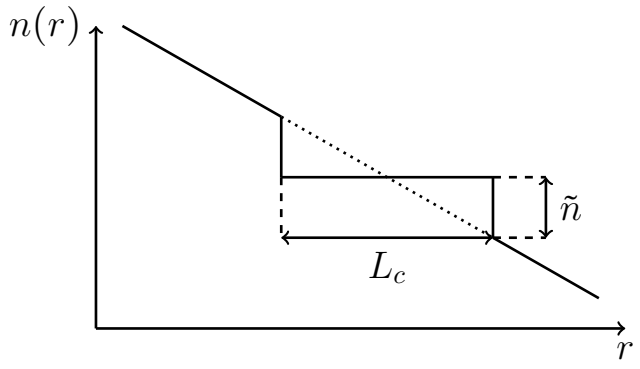

Figure 2.3: Schematic of the mixing-length model: a turbulent structure with correlation length L_c flattens the gradient. The turbulence amplitude is the size of the fluctuation $\tilde{n}$ (adapted from [14]).

regime ($\nu_* < 1$) is called banana regime, the high collisionality regime ($\nu_* > \epsilon^{3/2}$) is the Pfirsch-Schlüter regime while the intermediate regime is named plateau regime. The trapping of particles and the plasma curvature leads to larger excursion of the guiding centre orbit of the particle from the flux surfaces and thus to a larger step size due to the collisions. This enhances the diffusion process and leads to large transport as compared to the classical transport. Nevertheless the experimentally observed radial transport occurring in a tokamak is found to be significantly larger than the neoclassical predictions [12, 13]. The amount of transport which can not be explained by collisional transport is called turbulent transport.

Small fluctuations in the plasma parameters, e.g. density and temperature, can be thought as small irregular structures which enhance the radial transport due to microscopic potential structures . These structures have a finite correlation length L_c and time t_c which determine the transport coefficient, $D_t \approx L_c^2/t_c$. In the mixing-length model [15], a turbulent structure flattens a gradient region equal to its correlation length. The turbulent amplitude $\tilde{n}$ is the size of the perturbation (figure 2.3):

$$\frac{\mathrm{d}n}{\mathrm{d}r} = \frac{\tilde{n}}{L_c}. \tag{2.10}$$

The turbulence transport is then given by:

$$\Gamma = \tilde{n}\tilde{v}_r \tag{2.11}$$

where $\tilde{v}_r = L_c/t_c$ is the characteristic turbulence velocity. Equation (2.11) can be

of a closed magnetic field line and thus a measure of its helicity.

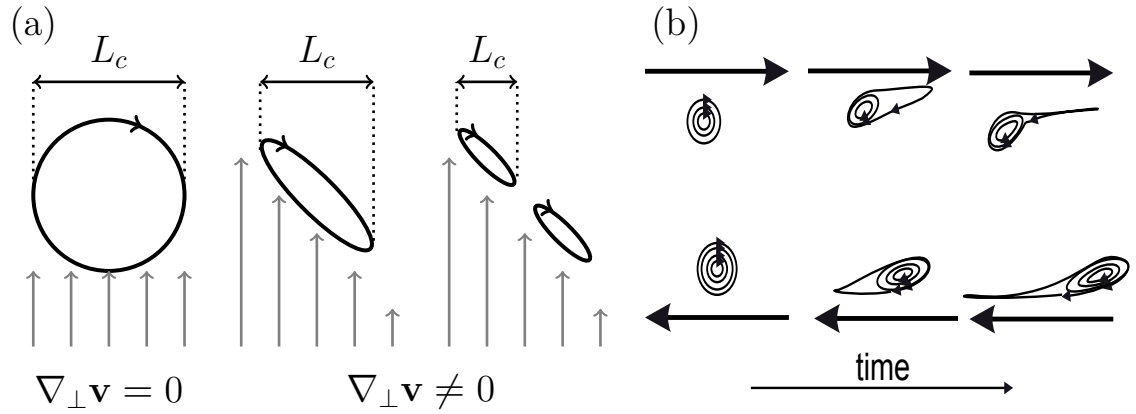

Figure 2.4: Schematic of the possible mechanism for the turbulence suppression due to shear flow: (a), breaking of the eddies by stretching and distortion [7]; (b), energy transfer from turbulence to flow through vortex tinning [16]. (figure (b) adapted from [16])

re-written as the first Fick's law [14]:

$$\Gamma = L_c \tilde{v}_r \frac{\mathrm{d}n}{\mathrm{d}r} = \frac{L_c^2}{t_c} \frac{\mathrm{d}n}{\mathrm{d}r} = D_t \frac{\mathrm{d}n}{\mathrm{d}r}. \tag{2.12}$$

The relation (2.12) emphasizes the role of the gradient in turbulent transport. This highlights the conceptual complications of the L–H transition where a steepening of the gradients is observed while the turbulence amplitude is reduced. In the next section, details on the effects of shear flows on the turbulence will presented.

2.2 Turbulence suppression by shear flows

Turbulent transport can be largely suppressed by shear flows. In 1990, Biglari, Diamond and Terry [7], first recognized this mechanism for the turbulence suppression in fusion plasma. When a turbulent eddy is placed in a constant flow $\mathbf{v}$ without any gradient perpendicular to its direction ($\nabla_\perp v = 0$), the eddy is simply transported (figure 2.4(a), first frame). Instead, if the background flow presents such a gradient ($\nabla_\perp v \neq 0$) the eddy is stretched and finally breaks up as different parts of the eddy are teared apart with different velocity (figure 2.4(a), second and third frame). This process leads to a reduction of the eddy correlation length and therefore of the turbulence diffusion coefficient (see equation (2.12)). However, it does not extract energy from the turbulence but it just redistribute it to smaller scales [17]. Another possible mechanism

for turbulence suppression is shown in figure 2.4(b). In fluid turbulence it is observed that the turbulent eddies are not destroyed but elongated and convolute in a larger flow [18]. An energy transfer is therefore established from the turbulence to zonal flows which do not contribute to radial transport and are also amplified by the energy transfer (details on zonal flows are given in section 2.3.3) [16]. In a tokamak plasma the velocity field $\mathbf{v}$ is given by the $\mathbf{E}\times\mathbf{B}$ velocity and the criterion for the turbulence decorrelation is [17]:

$$|\nabla \mathbf{v}_{\mathrm{E}\times\mathrm{B}}| = \left|\frac{\nabla E_r}{B}\right| > \frac{\omega_t}{k_\theta L_c} \tag{2.13}$$

where ω_t is the lifetime of a turbulence eddy and k_θ^{-1} the poloidal elongation with k_θ being the poloidal wavenumber of the turbulence. As discussed previously, it is not clear how an electric field, and therefore $\mathbf{v}_{\mathrm{E}\times\mathrm{B}}$, can be established in a plasma. This requires the solution of a self-consistent plasma model which is described in the next section.

2.3 Kinetic and fluid description of a plasma

2.3.1 The radial force balance

In a plasma, every particle is subject to the equation of motion (2.1). The distribution function $f_\alpha(\mathbf{r}, \mathbf{v}, t)$ gives the particle density of a certain species α in the six-dimensional phase space $(\mathbf{r}, \mathbf{v}, t)$. f_α obeys the conservation equation, which combined with (2.1) gives the Vlasov equation [19, 20]:

$$\frac{\partial f_\alpha}{\partial t} + \mathbf{v}\cdot\nabla f_\alpha + \frac{q_\alpha}{m_\alpha}(\mathbf{E} + \mathbf{v}\times\mathbf{B})\cdot\frac{\partial f_\alpha}{\partial \mathbf{v}} = 0. \tag{2.14}$$

The Vlasov equation neglects Coulomb collisions which can be implemented by the Fokker-Plank collision operator

$$C_\alpha(f) = \left.\frac{\partial f_\alpha}{\partial t}\right|_{\text{collisions}} \tag{2.15}$$

which describes the change per unit of time of the distribution function f_α due to collisions. The collision operator is added on the right-hand side of the Vlasov equation obtaining the so-called Fokker-Plank equation:

$$\frac{\partial f_\alpha}{\partial t} + \mathbf{v}\cdot\nabla f_\alpha + \frac{q_\alpha}{m_\alpha}(\mathbf{E} + \mathbf{v}\times\mathbf{B})\cdot\frac{\partial f_\alpha}{\partial \mathbf{v}} = C_\alpha(f). \tag{2.16}$$

The most interesting information of f_α is contained in its moments. By taking the first order velocity moment of equation (2.16), the fluid momentum or force balance equation is obtained [20]:

$$m_\alpha n_\alpha \left.\frac{\mathrm{d}\mathbf{v}_\alpha}{\mathrm{d}t}\right|_\alpha = -\nabla p_\alpha + q_\alpha n_\alpha (\mathbf{E} + \mathbf{v}_\alpha \times \mathbf{B}) + \mathbf{R}_\alpha - \nabla \cdot \mathbf{\Pi}_\alpha + \mathbf{F}_\alpha \tag{2.17}$$

where $\mathrm{d}/\mathrm{d}t|_\alpha$ is the convective derivative, $\mathbf{\Pi}_\alpha$ is the viscous stress tensor, $\mathbf{R}_\alpha$ the collisional friction and $\mathbf{F}_\alpha$ is the external force. The equation (2.17) is similar to the Navier-Stokes equation with the addition of the Lorentz force.

In general, the inertial term (left-hand side of equation (2.17)) is negligible compared to the friction and the pressure gradient. This, in turn, is much larger than the collisional friction and therefore equation (2.17) can be in first order in the normalized Larmor radius $\rho^* = r_L / L_c$ reduced to [19, 21, 22]:

$$0 = \nabla p_\alpha - q_\alpha n_\alpha (\mathbf{E} + \mathbf{v}_\alpha \times \mathbf{B}). \tag{2.18}$$

This equation can be re-written by taking its cross-product with the magnetic field:

$$\mathbf{v}_{\perp,\alpha} = -\frac{\nabla p \times \mathbf{B}}{n_\alpha q_\alpha B^2} + \frac{\mathbf{E} \times \mathbf{B}}{B^2} = \mathbf{v}_{dia,\alpha} + \mathbf{v}_{\mathrm{E}\times\mathrm{B}} \tag{2.19}$$

Thus, the perpendicular velocity is the sum of the diamagnetic and the $\mathbf{E}\times\mathbf{B}$ velocity. Another convenient form of equation (2.18) is the radial force balance equation. By taking an axis-symmetric configuration and assuming p_α to be a flux function, equation (2.18) can be re-written as [20]:

$$\begin{aligned} E_r &= \frac{1}{n_\alpha q_\alpha}\frac{\partial p_\alpha}{\partial r} + v_{\perp,\alpha} B \\ &= \frac{1}{e Z_\alpha n_\alpha}\frac{\partial p_\alpha}{\partial r} - v_{\theta,\alpha} B_\phi + v_{\phi,\alpha} B_\theta. \end{aligned} \tag{2.20}$$

Here, $v_{\theta,\alpha}$ and $v_{\phi,\alpha}$ are the poloidal and toroidal velocities and $\partial p_\alpha / \partial r / (e Z_\alpha n_\alpha)$ is the diamagnetic or pressure gradient term. This relation is used in this work to measure the radial electric field (see chapter 4) and it is valid as long as the ordering is satisfied (which is nearly always).

In toroidally symmetric configuration, the radial electric field is undetermined because the toroidal flow is a free parameter [23]. Various mechanisms could set the condition to determine the radial electric field or contribute to it, such as neutral friction with the ambipolarity condition [14], the neoclassical approximation of E_r [21], the turbulent stress driven flows [24], fast-ion orbit width effects [25] and ion orbit losses [26]. Given

the connection between a sheared $\mathbf{E}\times\mathbf{B}$ velocity and the turbulence suppression, all these phenomena can be potentially used to build a theory on the L–H transition. A brief overview on the L–H transition theories is given in section 2.5. Here, the main focus is on two mechanisms which have attracted interest in the last decade has being the most important players in the L–H transition physics: the neoclassical E_r and the generation of flows through turbulence stresses. Experiments which quantitatively address these mechanisms are necessary to unravel the fundamental players in the L–H transition physics. This is the ultimate purpose of this work.

2.3.2 Neoclassical approximation of the radial electric field

In 1991, Kim, Diamond and Groebner derived the explicit expression for the neoclassical poloidal and toroidal velocity [27] for main ions and impurities. Starting from the parallel momentum and heat flow balance equations [28] they derived expressions for the main ion and impurity poloidal velocities, respectively $v_{\theta,i}$ and $v_{\theta,\alpha}$:

$$\begin{aligned} v_{\theta,i}^{\text{neo}} &= \frac{1}{2} v_{th,i} r_{L,i} \left(K_1 \frac{1}{L_{T_i}} \right) \frac{B B_\phi}{\langle B^2 \rangle} \\ v_{\theta,\alpha}^{\text{neo}} &= \frac{1}{2} v_{th,i} r_{L,i} \left[\left(K_1 + \frac{3K_2}{2} \right) \frac{1}{L_{T_i}} - \frac{1}{L_{p_i}} + \frac{Z_i}{Z_\alpha} \frac{T_\alpha}{T_i} \frac{1}{L_{p_\alpha}} \right] \frac{B B_\phi}{\langle B^2 \rangle} \end{aligned} \tag{2.21}$$

where $v_{th,i}$ is the thermal velocity of the main ions, $r_{L,i}$ the main ion Larmor radius, K_1 and K_2 are the viscosity coefficients (see [27] for the definition), L_{T_i} and L_{p_i} are the ion temperature and pressure gradient scale lengths. The poloidal velocity of the main ions does not depend on the ion pressure gradient but only on L_{T_i} whereas $v_{\theta,\alpha}^{\text{neo}}$ is a function of L_{p_i} and L_{p_α}. Note that at the plasma edge, the impurities rotate poloidally faster compared to the main ions since the low diamagnetic velocity cannot compensate the $\mathbf{E}\times\mathbf{B}$ drift as in the case of the main ions. In other words, the radial force balance (2.20) has to be satisfied by every species, therefore, $v_{\theta,\alpha}$ is larger due to the smaller diamagnetic term [29]. The main ion poloidal velocity can be close to zero and in case the main ion toroidal velocity is also close to zero, the radial electric is roughly equal to the main ion diamagnetic term [21]:

$$E_r \approx \frac{\nabla p_i}{e n_i}. \tag{2.22}$$

Other assumptions can lead to the same approximation of E_r, such as the neutral friction combined with the ambipolarity condition [14]. In case of large $v_{\theta,i}^{\text{neo}}$ and/or large $v_{\phi,i}$, the neoclassical approximation of E_r can be calculated from full neoclassical models such as NEOART [30]. This was experimentally investigated in H-mode at

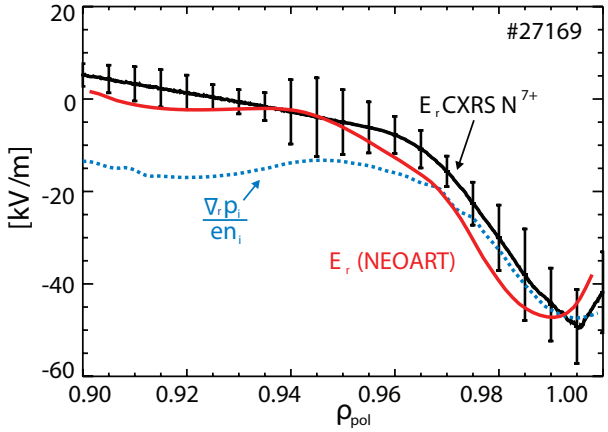

Figure 2.5: Comparison between: (black) measurement of E_r, (red) his neoclassical approximation and (blue) the diamagnetic term of the main ions. A good agreement is found between neoclassical predictions and measurements of E_r. In particular, at the very edge of the plasma, E_r is consistent with the diamagnetic term of the main ions. (adapted from [31])

ASDEX Upgrade where, at the plasma edge, the measurements of E_r are consistent with the simple neoclassical approximation (2.22) [31]. In Figure 2.5, the measured E_r (black) is compared with the diamagnetic component of the main ions (blue) and with the calculated neoclassical approximation (red). In this work, the electron diamagnetic direction is defined in the positive direction, i.e. poloidally upwards. Note that at the very edge of the plasma E_r is well described by $\mathbf{v}^{\mathrm{i}}_{\mathrm{dia}}$ whereas further inside the plasma full neoclassical modelling is required due to the finite toroidal flows. Many experiments have assessed whether the background gradients evolve together with E_r during the L–H transition. Experimental evidences for other contributions to E_r have been found ([32] and references therein). The one which has been recently investigated intensely in the framework of the L–H transition theories are the zonal flows.

2.3.3 Zonal Flows

Zonal flows (ZFs) are azimuthally symmetric, bandlike, shear flows generated by turbulence stresses [24]. They are universally observed in nature and laboratory. Examples are observed in planetary atmospheres, such as the Jovian belts, the Jupiter zonal streams or the Earth jet streams [33]. In a tokamak plasma, ZFs are toroidally ($n = 0$) and poloidally ($m = 0$) symmetric electrostatic potential fluctuations and are driven exclusively by nonlinear interactions, which transfer energy from the small scale drift waves to the $n = 0$ flow. Here, drift-waves describe all type of micro-instabilities. ZFs contribute to the poloidal plasma flow through the $\mathbf{E}\times\mathbf{B}$ velocity besides the always present diamagnetic velocity. The zonal flows are described in a general dynamic way

by the equation:

$$\frac{\partial v_{\theta,\mathrm{ZF}}}{\partial t} = \frac{\partial}{\partial r}\langle \tilde{v}_\theta \tilde{v}_r \rangle - \gamma_{\mathrm{damp}} v_{\theta,\mathrm{ZF}} \tag{2.23}$$

where $v_{\theta,\mathrm{ZF}}$ denotes the zonal flow velocity, $\langle \tilde{v}_\theta \tilde{v}_r \rangle$ the flux surface average of the product between the fluctuating poloidal $\tilde{v}_\theta$ and radial $\tilde{v}_r$ velocities, and γ_{damp} the flow damping. The first term on the right-hand side is the turbulent Reynold stress $\Pi_r = \langle \tilde{v}_\theta \tilde{v}_r \rangle$. Its radial derivative is the drive of the zonal flows [34]. The growth and the amplitude of the zonal flows is limited by several damping mechanisms described by γ_{damp} in equation (2.23). The most important contribution are from the ion-ion collisions and in toroidal plasmas the parallel viscosity [35]. The interest on zonal flows has increased substantially in the tokamak community in the last decade due to their capability to regulate drift-wave transport [36] and to develop a predator-prey relation with the turbulence [37, 38]. The latter is often used as a paradigm for the L–H transition and is discussed in section 2.5. The most clear experimental evidence for zonal flows has been found in low temperature plasmas where the ions are cold and therefore there is no contribution from the diamagnetic velocity. In this condition, the energy transfer between turbulence and flows can be directly measured [16]. In high temperature plasmas the existence of zonal flows is often discussed through the relation between flows and turbulence (a review of experiments can be found in [32] and in [39]) while a direct comparison between the neoclassical approximation and the measurements of E_r is often limited by the demanding diagnostic requirements. Quantifying the total contribution of ZFs to the total $\mathbf{E}\times\mathbf{B}$ shear and clarifying their interaction with $\mathbf{v}^{\mathrm{i}}_{\mathrm{dia}}$ is one of the compelling task of future experiments. This work contributes to unravel the interplay between turbulence, neoclassical and zonal flows during the L–H transition at ASDEX Upgrade.

2.4 The high confinement mode

The confinement time τ_E in a tokamak is defined as the ratio between the energy stored inside the plasma W and the net input power P_{net}, i.e. the injected power P_{inj} minus $\partial W/\partial t$:

$$\tau_E = \frac{W}{P_{\mathrm{net}}} = \frac{W}{P_{\mathrm{inj}} - \partial W/\partial t}. \tag{2.24}$$

The plasma stored energy can be rewritten as:

$$W = \int_V \frac{3}{2}(n_e T_e + n_i T_i)\, dV \tag{2.25}$$

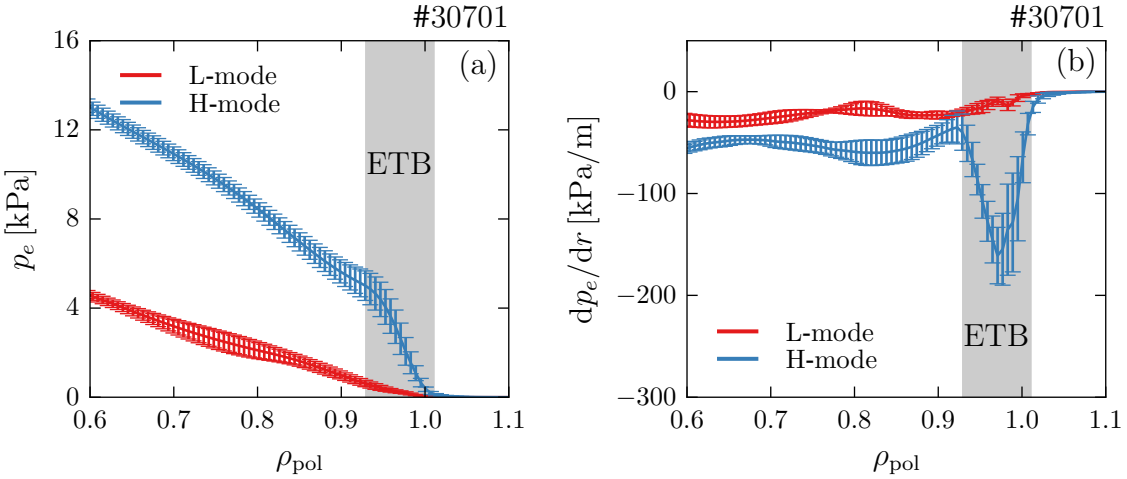

Figure 2.6: Electron pressure profile p_e (a) and its gradient $\mathrm{d}p_e/\mathrm{d}r$ (b) in L-mode (red) and in H-mode (blue). The electron pressure profile gradient in L- and H-mode clearly differ only in a small area close to the separatrix where the ETB is established. This sets an offset for the core p_e profile.

where V is the plasma volume, n_e and n_i the electron and ion densities, T_e and T_i the electron and ion temperatures. It is clear that an increase of electron and ion pressure at similar input power leads to a better confinement. This is exactly what happens at the H-mode onset, if the input power is raised above the power threshold a build up of electron and ion pressure is observed. In Figure 2.6 the electron pressure profile (a) and its gradient (b) are compared in L-mode (red) and in H-mode (blue). The electron pressure gradient in L- and H-mode clearly differ only in a small area at the very edge of the plasma – highlighted in gray – where the edge transport barrier is established. The ETB defines the boundary conditions for the profiles in the plasma core where no significant improvement in the pressure gradient is observed. Therefore the enhanced confinement, or in other words the increase of the plasma stored energy, is set by the edge transport barrier.

The stiffness of the profile in the plasma core, i.e. the small changes of the normalized gradients $\nabla T/T$ or $\nabla n/n$, is observed in different devices [40, 41]. The profile resilience sets on at a certain normalized gradient exhibiting a rapid increase of the transport [42, 43]. Turbulence instabilities are believed to drive this mechanisms and are often classified by their driving force, such as the ion temperature gradient mode, the trapped electron mode and the electron temperature gradient mode. The profile resilience is the macroscopic effect of the anomalous transport and the reason of designing large and hence expensive machines to obtain enough fusion power. However, this does not apply to the edge of an H-mode discharge where the turbulence is strongly reduced.

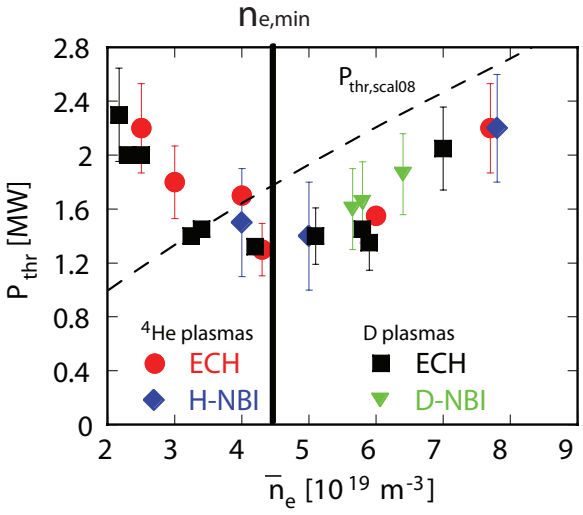

Figure 2.7: Dependence of the L–H power threshold P_{thr} on the line averaged density $\bar{n}_e$. The data shows two different trends: for $\bar{n}_e$ below $n_{e,min}$, P_{thr} decreases whereas it increases for $\bar{n}_e > n_{e,min}$ (reprinted from [44]).

2.4.1 The L–H transition power threshold

The input power requirement for accessing the H-mode is one of the key constraints for the design of any future fusion device. Given the lack of physics based model for the L–H transition, experiments of present-day devices are used to extrapolate to future experiments. A multi machine database of the L–H transition power threshold has been built collecting data from fourteen different machines [45]. The resulting scaling for deuterium (D) plasmas in discharges with low power the threshold is [46]:

$$P_{\mathrm{thr,scal08}} = 0.049\, \bar{n}_e^{0.72}\, B_\phi^{0.80}\, S^{0.94} \tag{2.26}$$

where $\bar{n}_e$ is the line-averaged density in $10^{20}\,\mathrm{m}^{-3}$, B_ϕ is the toroidal magnetic field in T and S the plasma surface in m^2. Note that the B_ϕ-dependence is well reproduced across the whole database while the $\bar{n}_e$-dependence shows deviations at low densities in several devices [44, 47–50]. In particular an increase of P_{thr} is observed below a certain density, here labelled $n_{e,\mathrm{min}}$, as shown in Figure 2.7 for the power threshold in ASDEX Upgrade [44]. The scaling $P_{\mathrm{thr,scal08}}$ is obtained from a subset of data where only the high density branch ($\bar{n}_e > n_{e,\mathrm{min}}$) is considered.

The L–H transition power threshold shows other dependencies not considered in the scaling (2.26). In particular, P_{thr} scales with the inverse of the ion mass M_i of hydrogen isotopes [51] and depends on the ion ∇B drift direction [52]. The configuration with the ion-drift direction pointing from the plasma center towards the magnetic X-point

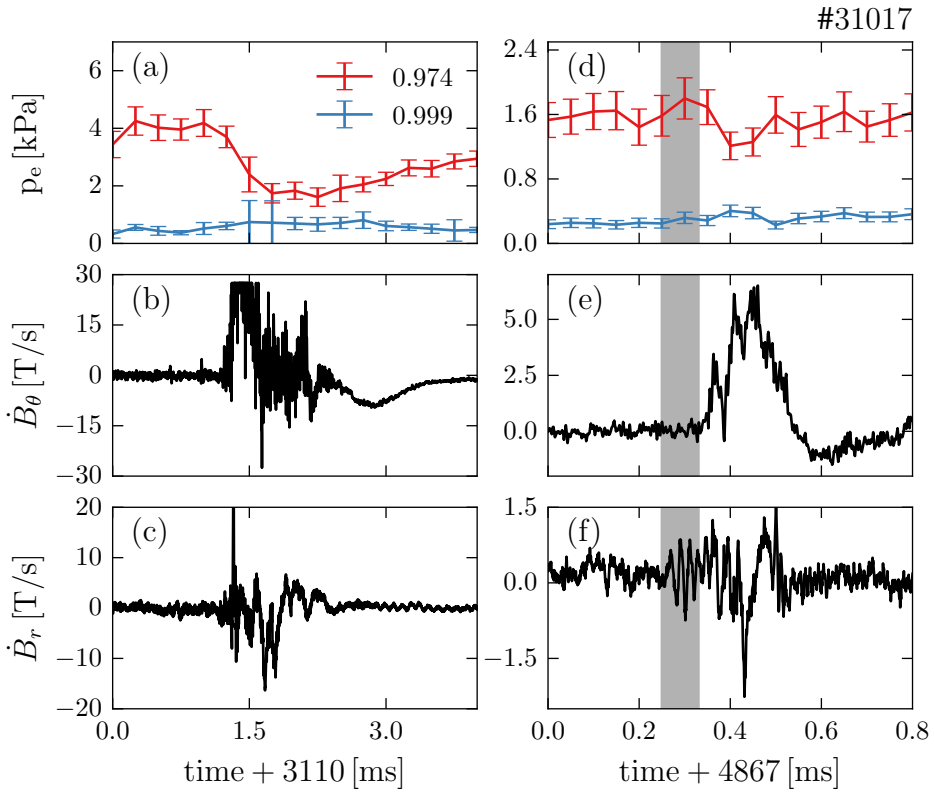

Figure 2.8: Magnetic signature of type-I (a)-(c) and type-III ELMs (d)-(f): (a) and (d) electron pressure measured at two radial position, (b) and (e) poloidal magnetic field fluctuation $\dot{B}_\theta$, (c) and (f) radial magnetic field fluctuation $\dot{B}_r$. The magnetic precursor is indicated in the shaded region.

is called "favourable" configuration otherwise "unfavourable". In the "unfavourable" configuration the power threshold is roughly two times higher than in the "favourable" configuration. Moreover, the position of the X-point [53] and the toroidal velocity [54] are reported to affect P_{thr}. In this work, it is investigated: (i) the plasma isotopes dependence by performing experiments in deuterium (D) and hydrogen (H) plasmas, (ii) the B_ϕ-dependence, (iii) the n_e-dependence.

2.4.2 The edge localized modes (ELMs)

While the H-mode is the most favourable regime for a future reactor, it also carries one of the most serious physics and engineering problem of the present fusion research: the edge localized modes or ELMs. The ELMs lead to periodic relaxation of the edge profile gradients [55]. Each ELM lasts for a few 100 µs and produces energy and particle losses and their loads on the divertor target could lead to a rapid damage of the first wall [56].

The mitigation or even full suppression of ELMs are mandatory for future devices.

Different types of ELMs have been identified [55], this work is focussed on the type-I and the type-III ELMs. Type-I ELMs are sharp isolated events which limit the pressure gradient at the plasma edge. Their frequency is typically in the range of 10 to 150 Hz at AUG and increases with the heating power. The type-I ELMs are peeling-ballooning instabilities which are triggered by a critical pressure gradient and a critical edge current density [57]. Type-III ELMs have instead higher frequencies (0.5–10 kHz) which decrease with increasing heating power. They are mostly observed at an input power close to the L–H power threshold and seem to be connected with the L–H transition itself. A widely accepted theory about the underlying physics of the type-III has not been shown yet [55]. The type-III ELMs are often labelled as magnetohydrodynamic events because they show a coherent magnetic precursor in the radial magnetic field fluctuations $\dot{B}_r$. The precursor is not observed before type-I ELMs. In figure 2.8, a comparison of the magnetic signature of type-I (a)–(c) and type-III (d)–(f) is shown. The relative collapse of the edge pressure is typically large in case of type-I ELMs (a) as compared to that during type-III ELMs (d). The duration is also different, the magnetic perturbation on the $\dot{B}_\theta$ is roughly six times longer and larger in case of the type-I ELM (b) than during a type-III ELM (e). The type-III ELM shows a precursor in the $\dot{B}_r$ signal ((f), shaded area) while no sign of a precursor is visible during a type-I ELM (c).

2.5 Overview on the L–H transition theories

A review of the L–H transition theories can be found in [58]. Here, the focus is on the "two-step" theories where step one is the formation of E_r and step two is the suppression of the edge turbulence via $\mathbf{E}\times\mathbf{B}$ velocity shear. In this framework, any contribution to E_r can be potentially used for developing an L–H transition theory. The radial electric field is generated by non-ambipolar radial flows, i.e. radial currents, which can be caused by diffusion mechanisms. Radial flows and currents are caused by drifts due to the poloidal forces or by direct losses of particles. Many theories have focussed on external direct contribution to the $\mathbf{E}\times\mathbf{B}$ velocity. Given the radial force balance for the main ions, any change in E_r not induced by pressure gradients results in a non-zero poloidal velocity if the toroidal velocity is small. For this reason, this branch of theories has been historically referred to "poloidal spin-up" theories. For consistency, the same nomenclature is used in this work despite it can be misleading. The theories where the diamagnetic term is discussed as the main contribution to the total E_r are classified as "pressure gradient" theories.

2.5.1 Poloidal spin-up theories

Several effects could drive poloidal flows in a plasma, e.g. by non-ambipolar mechanisms or turbulence stresses. Ion orbit losses can trigger a transition [59] as well as non-ambipolar electron losses [60]. The theory developed by Shaing et al. predicts the generation of a positive (in the electron diamagnetic direction) flow as a consequence of ion orbit losses. However, this was not observed in the experiments where the main ion poloidal velocity is negative [31, 61]. Itoh et al. instead suggested non-ambipolar electron and ion losses to cause dual solutions of the ambipolar condition and the L–H transition as a change from negative (L-mode) to positive (H-mode) of the radial electric field which does not agree with the experiments. However, these effects could still contribute to the total E_r.

As discussed in section 2.3.3, also turbulence induced flows or zonal flows are predicted to have the potential to induce an L–H transition through a "predator–prey" relation with turbulence [37, 38]. This theory had the merit to predict an intermediate phase, originally called dithering H-mode, between L- and H-mode states which has been observed nowadays in almost every machine [62–71]. In this work, this "intermediate phase" is labelled "I-phase" as proposed in [66]. The I-phase is characterized by fluctuations in the turbulence level and in the $\mathbf{E}\times\mathbf{B}$ velocity at the plasma edge. In Figure 2.9 the time-traces of $\mathbf{v}_{\mathrm{E}\times\mathrm{B}}$ (a) and density fluctuations $\tilde{n}/n$ (b) at the plasma edge are shown. Here the measurements of $\mathbf{v}_{\mathrm{E}\times\mathrm{B}}$ and $\tilde{n}/n$ are obtained from Doppler reflectometry. The spikes in the density fluctuations correlate with $\mathbf{v}_{\mathrm{E}\times\mathrm{B}}$ and with the D_α radiation in the divertor region (c). The latter is often used as an L–H monitor signal and it is proportional to the electron and neutral density in the divertor region. The model proposed by Diamond et al. interprets this phase as a competition between turbulence – the prey – and turbulence induced flows or zonal flows – the predator. Recently, this model has been modified to include neoclassical flows, i.e. the flows generated by the neoclassical E_r (see section 2.3.2), as a second "predator" [72, 73]. The neoclassical flows are predicted to be responsible for locking the transition to H-mode: during the I-phase they slowly (compared to the ZFs) evolve with the steepening of the ion pressure (see equation (2.22)) due to the partial turbulence reduction until they can actively shear the turbulence eddies themselves. At this point the H-mode takes place and the turbulence is completely damped and thus, ZFs cannot be induced anymore. The fluctuations during the I-phase are often called Limit Cycle Oscillations (LCOs) [68] whereas the phase itself was also referred to as "IM-mode" [63] or "M-Mode" [69]. The existence of zonal flows is often deduced from the phase relation between turbulence amplitude and flows, where a phase difference of $\pi/4$ is characteristic for predator-prey oscillations [37, 38]. Direct measurements of the energy transfer from turbulence to the ZF through Reynolds stress were made in low temperature plasmas [16], however,

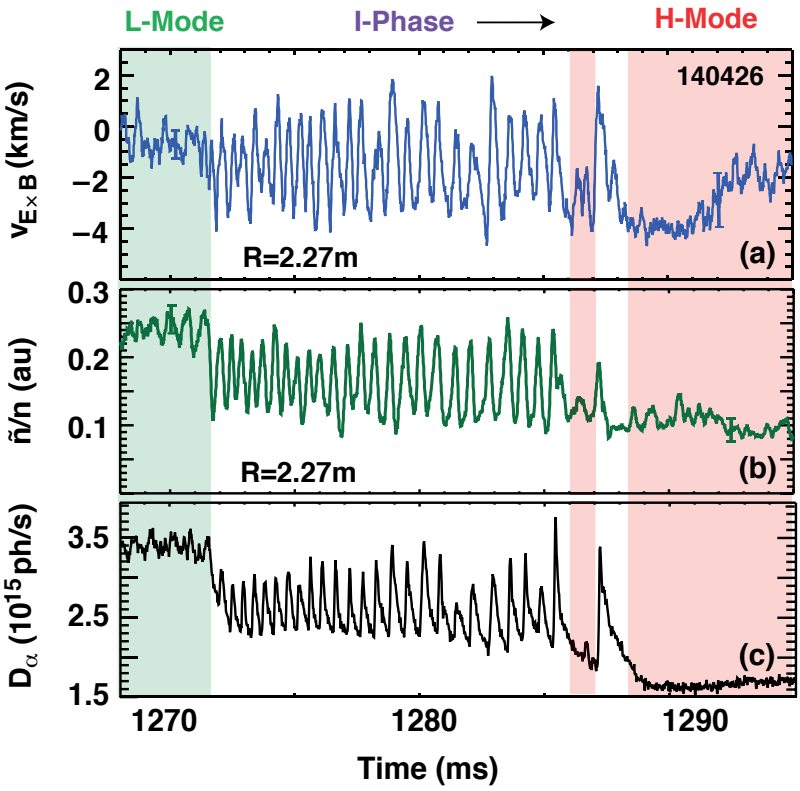

Figure 2.9: Time evolution of a L–H transition at the DII-D tokamak: (a) $\mathbf{v}_{\mathrm{E}\times\mathrm{B}}$, (b) density fluctuations $\tilde{n}/n$, (c) D_α radiation in the divertor region. In the evolution from L-mode (green-shaded area) to H-mode (red-shaded area), an intermediate phase (I-phase) is observed where the edge turbulence and $\mathbf{v}_{\mathrm{E}\times\mathrm{B}}$ fluctuate. (adapted from [68])

in fusion plasmas a direct measurement is not possible. Note that a significant level of the Reynolds stress Π_r cannot be taken as first principle demonstration of zonal flow activity, since any change in $\mathbf{v}_{\mathrm{E}\times\mathrm{B}}$, containing also the neoclassical flow, may also tilt the turbulence eddy orientation and therefore, affect Π_r [74]. It might be clear that the zonal flow production intrinsically takes place whenever turbulence eddies are suppressed (see section 2.3.3), but whether this is the dominant contribution to E_r at the L–H transition is still an open issue for the modelling [72–74] and for the experiments [66–68, 70, 71]. In particular, the LCOs are often reported to smoothly transient to type-III ELMs which are macroscopically similar to the LCOs but present a precursor [70, 75, 76]. However, recent studies suggest that the absence of the precursor might be connected to a detection limit and a precursor in the reflectometry data has been observed, which was not visible in $\dot{B}_r$ [77]. Therefore, the difference between type-III ELMs and LCOs and the underlying physics is as of yet not clear.

2.5.2 Pressure gradient theories

The edge pressure gradient contributes to the total E_r through the diamagnetic velocity and hence to the shearing of turbulence (see section 2.3.1). However, it is also the source of the turbulence. The pressure gradient theories study the competition between turbulence shearing and turbulent transport while the input power is increased, i.e. while ∇p steepens up. This idea was first proposed by Hinton [78] and can be expressed in terms of the transport coefficient χ as follows:

$$\chi = \frac{\chi_0}{1 + c_0 v'^{\alpha}} \tag{2.27}$$

where χ_0 is the transport coefficient in absence of the shear, $v' = \partial v / \partial x$ is the velocity shear, c_0 and α are constants. These types of models assume that v' is dominated by E_r induced by the pressure gradient. Here, the key parameter is α which defines how effective the shear in competition with the increased transport is. The most recent models do not agree in the prediction of α which is found to be equal to 2 [79] or to 0.7 [80]. In the first case, the proposed model is able to produce a transition whereas the second model does not. However, it is clear that the background flows are the fundamental player for locking in any transition model to H-mode after the initial turbulence suppression [72, 73] and, in certain circumstances, they can alone trigger an ETB [81]. Moreover, there is experimental evidence for the importance of main ions in setting the background conditions for the L–H transition physics [82, 83] and of the edge profile gradients during the LCO [70, 71]. In particular, independent studies [47, 83–85] show that a critical E_r minimum (a good proxy of the E_r gradient [29]) is required to access the H-mode independent of the electron density. In particular, at low density, where the decoupling between electrons and ions is stronger ($T_e/T_i > 1$) and where P_{thr} increases, E_r is found to be constant indicating that the heating which goes to the ions is a key player of the L–H transition. Moreover, a correlation between the ion edge heat flux and the H-mode onset have been found through power balance analysis confirming again the fundamental role of the main ions in the L–H transition physics [82].

3 Plasma edge diagnostics at ASDEX Upgrade

As discussed in chapter 1, to unravel the physics of the L–H transition it is necessary to measure the following edge parameters with at a few hundreds of µs time resolution

i. the density n and temperature T

ii. the $\mathbf{E}\times\mathbf{B}$ flow

iii. the turbulence amplitude.

In this work, the Integrated Data Analysis (IDA) diagnostic [86] has been used to determine the edge electron temperature T_e and density n_e from the Lithium Beam Emission (Li-BES) diagnostic, the DCN lasers interferometry, the electron cyclotron emission diagnostic (ECE) and from the Thomson scattering system (TS). The edge charge exchange recombination spectroscopy (CXRS) [8] was employed for the measurements of the ion temperature T_i and the radial electric field E_r and the Doppler reflectometry was used for the evaluation of E_r and the turbulence amplitude. Moreover, measurements of the magnetic fluctuations ($\dot{B}_r$ and $\dot{B}_\theta$) are used for the characterization of the different phases in the evolution from L- to H-mode. In this chapter, the set of edge diagnostics in AUG is described except for the CXRS diagnostic, which was upgraded and installed during this thesis and is characterized in chapter 4.

3.1 The integrated data analysis of the electron density and temperature profiles

The integrated data analysis algorithm [86] reconstructs the electron temperature and density profile combining different diagnostics in the framework of the Bayesian theory. The lithium beam emission spectroscopy (Li-BES) [87] and the laser interferometry are used for the reconstruction of n_e whereas the electron cyclotron emission diagnostic (ECE) [88, 89] is used for T_e. The Thomson scattering (TS) [90] can be optionally included in the reconstruction of T_e and n_e. There are several advantages of this

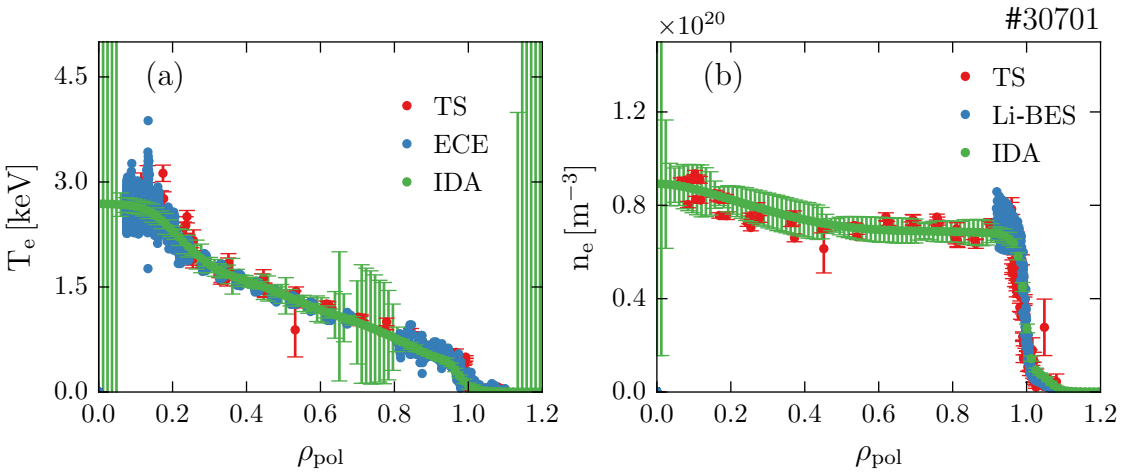

Figure 3.1: Reconstruction of the T_e (a) and n_e (b) profiles by the integrated data analysis algorithm. (a): in red the Thomson scattering measurements, in blue the electron cyclotron emission and in green the reconstructed profile from IDA. (b): in red the Thomson scattering measurements, in blue the Li-BES measurements and in green the reconstructed profile from IDA. The DCN interferometry measurements are not shown since they are line integrated measurements of n_e.

approach, such as: consistency in error bar calculation, reduced uncertainties by combining multiple information from different diagnostics, direct implementation of inter-diagnostic dependencies, easy identification of outliers and/or systematic errors. In Figure 3.1 an example of the IDA reconstructed profile of T_e (a) and n_e (b) is shown. The IDA T_e profile (green) is compared with the measured T_e profiles from ECE (blue) and from TS (red) whereas the electron density is compared with Li-BES (blue) and TS (red). Here, the DCN interferometer is not shown since it provides only line integrated measurements of the electron density. The n_e and T_e profiles are parameterized with the exponential of a cubic B-spline which by definition are C^2 functions and therefore intrinsically provide an estimation of the radial gradient [91]. Thus, no manual fitting of the data is required to calculate the gradients. The link to the measurements is given by a physical model which reconstruct the measured raw data from a given set of parameters. However, given the computational cost of the fitting routine, pre-processing of data is performed, e.g. calibration and background subtraction. In the following the basic principle of the IDA algorithm is described.

3.1.1 Lithium beam emission spectroscopy (Li-BES)

The Li-BES diagnostic exploits the interaction between the plasma and injected neutral lithium (Li) atoms injected at an energy of around 45 keV. Collisions excite the lithium

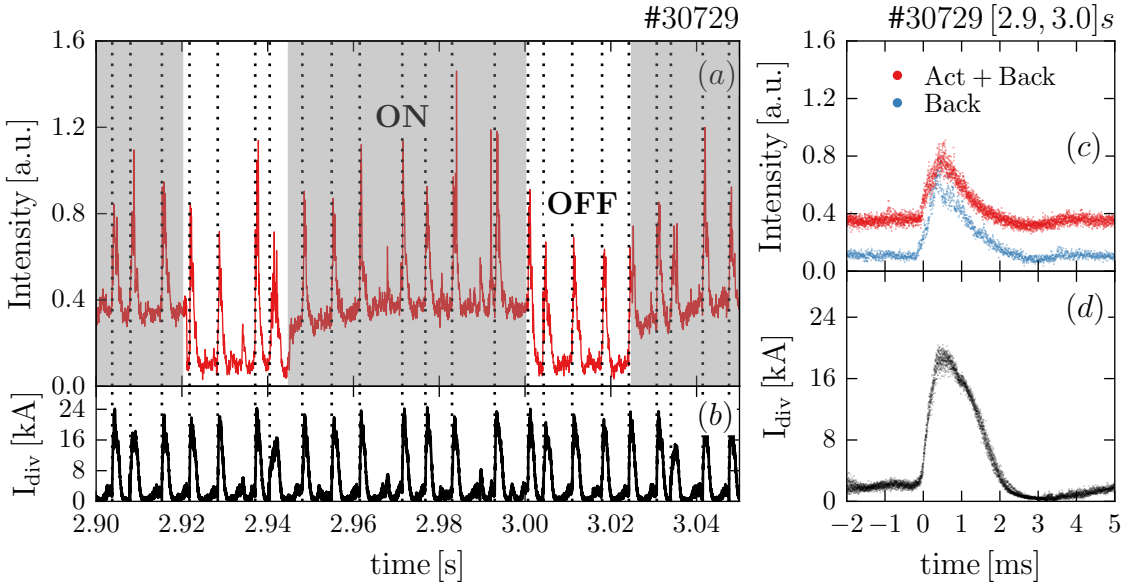

Figure 3.2: New method for the evaluation of intra-ELM n_e profiles based on Li-BES diagnostic: (a) evolution of the intensity of one LOS, (b) divertor shunt current I_{div}, (c) synchronized time traces of on LOS signal with focussed (red) and deflected beam (blue), (d) synchronized time trace of I_{div}. The highlighted areas in figure (a) indicate the time windows when the Li-beam is focussed onto the lines of sights.

atoms mainly to the $\mathrm{Li}_{2\mathrm{p}}$ state and its resonance line at 670.8 nm ($\mathrm{Li}_{2\mathrm{p}\to 2\mathrm{s}}$) can be measured [92]. From the spatial distribution of the line intensity, one can calculate the electron density profile [93]. A collisional-radiative model including electron-impact excitation, ionization and charge exchange processes is employed to reconstruct the emission profile. The sensitivity of the diagnostic decreases with the attenuation of the Li-beam, therefore at AUG the reconstructed profiles extend up to roughly $\rho_{\mathrm{pol}} = 0.95$.

The AUG experimental set-up of the Li-BES diagnostic was upgraded in 2013 with the installation of a new optical head [87]. Fifty new lines of sight resolve the complete radial penetration of the lithium beam with a radial resolution of about 6 mm. Every channel is equipped with an interference filter at the red-shifted $\mathrm{Li}_{2\mathrm{p}\to 2\mathrm{s}}$ line and with a photo-multiplier to ensure good signal to noise ratio. Moreover, a new acquisition system has been installed which allows a sampling rate of 200 kHz. The background radiation is subtracted from the active signal by chopping the Li-beam periodically. In Figure 3.2a the intensity of one Li-BES channel is plotted as a function of time (red). The signal is modulated by the intermittent chopping of the Li-beam. Moreover, the comparison between the divertor shunt current I_{div} (b) and the Li-BES intensity (a) shows that the edge localized modes (ELMs) have a strong effect on active and background signal (see dashed vertical lines). The divertor tile shunt current is an

indicator of heat and particle fluxes reaching the divertor plates and in metal divertor tokamaks it is often used as a monitor signal for ELMs and the L–H transition. The strong effect of ELMs on the background signal needs to be treated accurately. In the framework of this work, a new algorithm for the background subtraction was developed which allows to evaluate intra-ELM n_e profiles. The background radiation is synchronized relatively to the ELM onset using I_{div} as a reference signal. This is then subtracted from the signal when the Li-beam is not deflected in order to obtain only the active part. In Figure 3.2c the conditional synchronized background signal (green) and the sum of active and passive signal (blue) are shown. The intensity is synchronized based on the divertor shunt current shown in figure 3.2b. The synchronized divertor shunt current is shown in figure 3.2d.

3.1.2 The laser interferometry diagnostic

Interferometric methods generally exploit the dependence of the refractive index N on the density of a transparent medium. The interaction between electrons and electromagnetic waves in a plasma can be described by the connection between N and the electron density n_e:

$$N = \sqrt{1 - \frac{\omega_p^2}{\omega_0^2}} = \sqrt{1 - n_e \frac{e^2}{\epsilon_0 m_e \omega_0^2}} \tag{3.1}$$

where ω_p is the plasma frequency, e the elementary charge, ϵ_0 the dielectric constant, m_e the electron mass and ω_0 the frequency of the electromagnetic wave. By superimposing two waves, one propagating through vacuum and one propagating through the plasma, it is possible to measure the phase difference ϕ created by the different optical paths. By taking the first order Taylor approximation of 3.1 assuming $\omega_p^2/\omega_0^2 \ll 1$, ϕ can be written as:

$$\phi = \frac{2\pi}{\lambda} \int (N_{\mathrm{vac}} - N(x)) dx = \frac{\lambda e^2}{4\pi c^2 \epsilon_0 m_e} \int n_e(x) dx \tag{3.2}$$

where x is the coordinate along the wave propagation, $N_{\mathrm{vac}} \approx 1$ is the refractive index in vacuum and λ is the wavelength of the propagating wave in vacuum. The equation (3.2) shows already the strongest limitation of the interferometry systems: they measure line-integrated density and not localized ones.

The DCN laser interferometry system at AUG consists of five laser beams (H-1 to H-5) intersecting the plasma at different positions. The system is equipped with deuterium cyanide (DCN) lasers operated at a wavelength of 195 µm [94] and provides a time resolution of 300 µs. The DCN interferometry data are reconstructed by the IDA algorithm through the spatial integral of the density along the laser lines of sight.

3.1.3 Electron cyclotron emission

The electrons in the plasma gyrate around the magnetic field lines emitting radiation at the angular electron cyclotron frequency $\omega_{c,e} = eB/m_e$ and its harmonics $\omega_k = k\omega_{c,e}$. Assuming that the plasma is optically thick at the second harmonic of the cyclotron frequency, i.e. the radiation temperature T_{rad} is equal to the electron temperature, and that the underlying electron energy distribution is close to thermal equilibration, the Planck's law of black body radiation holds and therefore the spectral radiance I_ω is given by:

$$I_\omega(\omega) = \frac{\omega^2}{2\pi^2 c^2} k_B T_e \tag{3.3}$$

The optically thick layer, for a certain frequency $\omega_{c,e}$, is relative small (few mm) and therefore it provides a good radial resolution. By measuring the spectral radiance at a certain frequency, T_e can be determined using expression (3.3). However, the plasma is not always optically thick. In particular, at low densities, the shine-through effect increases the radiation resulting in unreal electron temperatures. Here, a forward model for the electron cyclotron radiation transport is applied to extract T_e up to the separatrix [95]. The electron cyclotron emission (ECE) system at ASDEX Upgrade measures simultaneously sixty different frequencies with a sampling rate of 1 MHz. Each frequency corresponds to a radial position R which is given by the magnetic field $B(R)$.

3.1.4 Thomson scattering

The Thomson scattering (TS) diagnostic is widely used in plasma physics for localized and simultaneous measurements of the electron density (n_e) and temperature (T_e). The scattering of electromagnetic waves by charged particles was first explained by J.J. Thomson [96]. The electric and magnetic components of an incident wave accelerate charged particles (in case of a plasma the electrons since $m_e \ll m_i$) which in turn emit radiation in all directions, thus scattering the wave. The scattered radiation is frequency shifted as a double Doppler effect takes place, one or the incoming photon and one for the outgoing photon emitted by the electron. The Doppler width of the measured scattered radiation provides the information of T_e whereas the intensity is proportional to n_e.

ASDEX Upgrade is equipped with a vertical Thomson scattering system which provides electron density and temperature profiles from the plasma core to the edge [90]. The scattering volume is around 25 mm^3 in the plasma core and 3 mm^3 at the plasma edge. Two systems of respectively four and six lasers are used for edge and core measurements. The scattered waves are collected by twenty-six polychromators providing spatially resolved profiles. The temporal resolution is 3 ms at the plasma edge and 8 ms

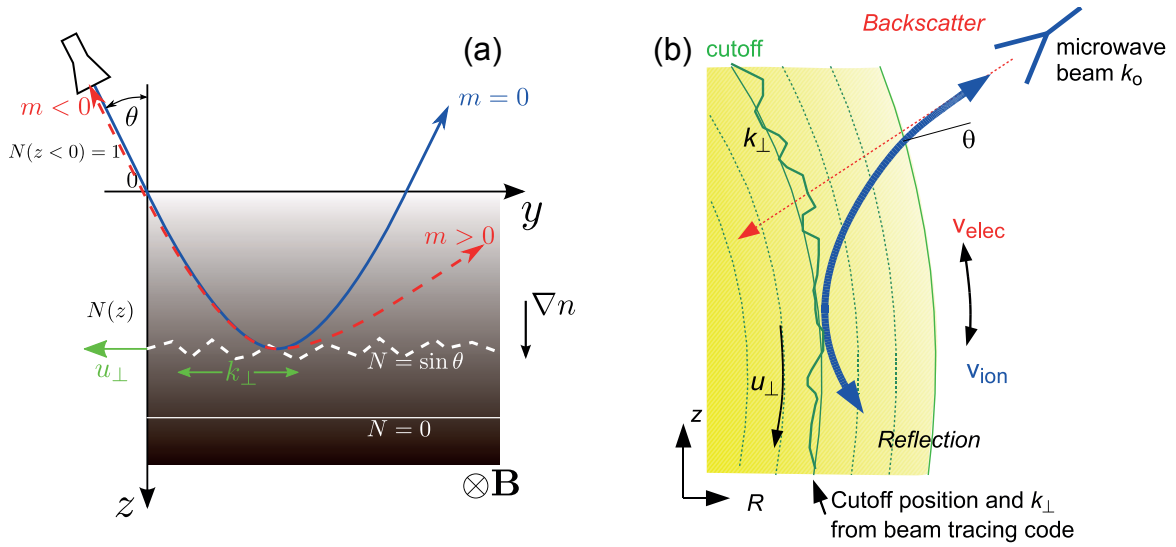

Figure 3.3: Concept of the Doppler reflectometry diagnostic in a slab geometry (a) and in a real geometry (b): a moving sinusoidally corrugated layer with velocity $\mathbf{v}_\perp$ backscatters incoming electromagnetic waves. The Doppler shift of the -1 order reflection is proportional to $\mathbf{v}_\perp$ while the intensity of the signal to the ruggedness of the scattering surface, i.e. the turbulence level (adapted from [5, 97]).

in the core. This is not fast enough to resolve the typical L–H transition timescales (≈100 µs) and therefore the TS was excluded from the IDA reconstruction although it is included in the original algorithm. Thus, in this work, the edge n_e evaluation just relies on the Li-BES diagnostic.

3.2 The Doppler reflectometry system

The concept of Doppler reflectometry (DR) is illustrated in figure 3.3. A microwave beam is launched into the plasma with a tilt angle θ where it is eventually reflected at a plasma cutoff surface. In the presence of a corrugated surface, the beam is also Bragg scattered (figure 3.3). The corrugation of the cutoff layer, which is determined by the cutoff plasma density, is caused by density fluctuations. To understand the basic principle of DR, one can model the cutoff layer as a reflection grating with a small sinusoidal corrugation with a wavenumber $k_\perp$ [98]. For a setup where the scattered microwave is measured with the launching antenna, the returned pattern of order -1 satisfies the Bragg condition if

$$k_\perp = 2k_0 \sin\theta \tag{3.4}$$

where k_0 is the wavevector of the microwave. By changing θ the $k_\perp$-spectrum of the density perturbation can be scanned. If the corrugation pattern, i.e. the turbulent fluctuations, of the cutoff layer propagates with a velocity $\mathbf{u}$, the backscattered microwave is Doppler shifted by $\omega_D = \mathbf{u} \cdot \mathbf{k}$ and gives information on the velocity of the plasma fluctuations. Ray tracing calculations enable the determination of $\mathbf{k}$ and the cutoff layer position and therefore the measurement of $\mathbf{u}$ profiles. In particular, since the turbulence structure are very elongated in the parallel direction, by probing the plasma with a microwave beam the backscattered Doppler shift is only a result of the movement perpendicular of them $\omega_D = k_\perp u_\perp$ thus allowing to directly measure $u_\perp$.

The perpendicular velocity $u_\perp$ is equal to the sum of the $\mathbf{E}\times\mathbf{B}$ drift velocity and the turbulent phase velocity of the density fluctuations v_{ph}. v_{ph} is assumed to be small, which has been confirmed by experiments in different machines [98–100]. Thus, the perpendicular velocity is a good approximation of the plasma $\mathbf{E}\times\mathbf{B}$ velocity.

Combined with measurements of $\mathbf{v}_{\mathrm{E}\times\mathrm{B}}$, the Doppler reflectometry provides information on the turbulence intensity A_D. The influence of the turbulence amplitude on the backscattered signal can be represented as a screening effect of the measured layer by turbulence. Screening scatters a part of the signal power of the receiving antenna preventing absolute measurements of the turbulence amplitude. However, for most of the cases, the power scattered into the diffraction order -1 can still be used as a qualitative monitor of the temporal evolution of the fluctuation amplitude at the preselected wavenumber. An example is shown in picture 1.3b.

3.3 Magnetic fluctuation measurements

Following Faraday's law, a temporal change in the magnetic field going through a conductor loop induces a current in this loop leading to a voltage. The measured voltage corresponds to the rate of change of the magnetic field. Therefore, a magnetic coil installed within the vessel of a magnetically confined plasma allows to measure magnetic fluctuations $\partial B / \partial t$ caused for example by instabilities.

The most common coils used for magnetic fluctuations in fusion plasmas are the Mirnov coils which depending on the wiring, can measure fluctuations alternatively in the poloidal B_θ or radial B_r field direction [101]. ASDEX Upgrade is equipped with several Mirnov coils as shown is figure 3.4. Two arrays in the poloidal plane named "C09–X" and "C07–X" (figure 3.4a, green) are distributed along the poloidal cross-section (figure 3.4b, green) and assigned to measurements of $\dot{B}_\theta$. Moreover, the "B31–X" coils (red) measure the magnetic fluctuations in the radial direction $\dot{B}_r$. Every coil is equipped with an Analog Digital Converter with a maximum sampling rate of 500 kHz. The overall system is used for different purposes, for instance to study MHD

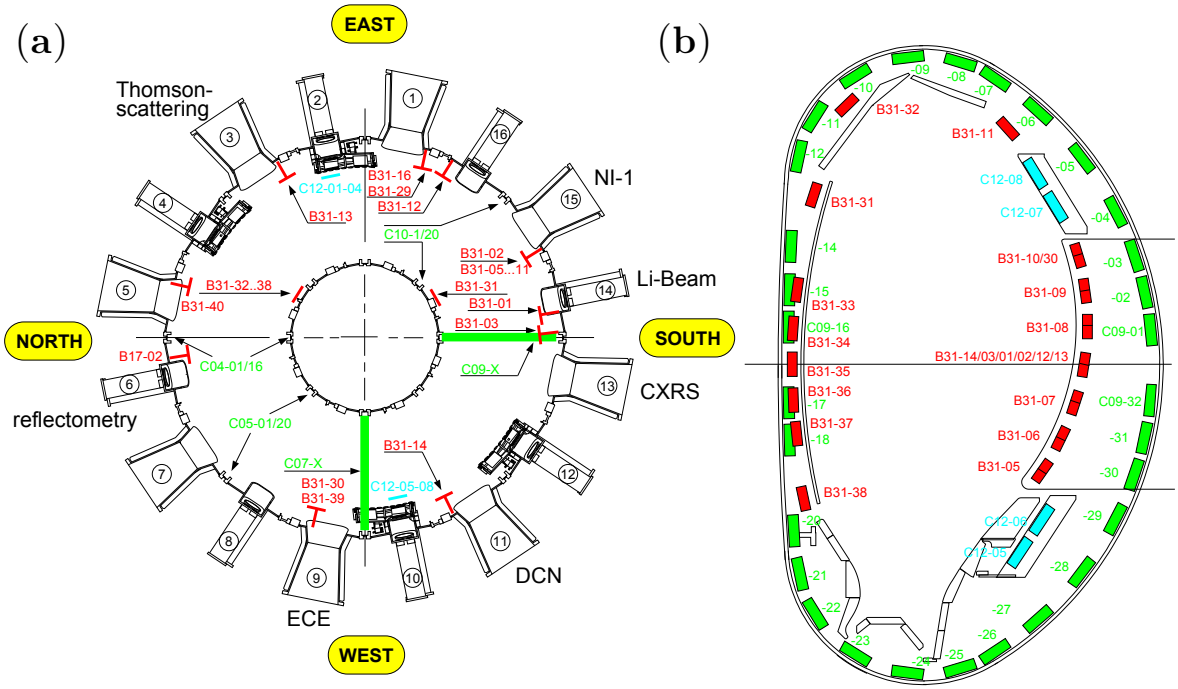

Figure 3.4: Overview of the magnetic fluctuation measurement system at ASDEX Upgrade. The diagnostic consists of Mirnov coils assigned to measure radial (red) and poloidal (green) magnetic field fluctuations, $\dot{B}_r$ and $\dot{B}_\theta$ respectively. The toroidal overview of the coil position is shown in figure (a), while the poloidal arrangement is shown in figure (b).

instabilities [102], disruption mitigation [103] or edge localized modes (see chapter 2, section 2.4.2). In this work, the magnetic signal is recorder during the L–H transition.

4 The edge CXRS diagnostics at ASDEX Upgrade

The diagnostic capabilities of charge exchange recombination spectroscopic (CXRS) was recognised from the earliest days in the fusion community [104]. Now many key plasma parameters are accessed through CXRS, such as ion temperature and flows, impurity influx and electric fields [105]. In this chapter, the upgraded edge charge exchange system at AUG is described. During this work, the spatial coverage and temporal resolution of the low field side edge CXRS diagnostic [8] have been improved and new data analysis techniques were developed.

4.1 Basic principle of CXRS

The basic principle of charge exchange recombination spectroscopy exploits spectral lines produced by charge transfer from neutral atoms (D) into highly excited states of impurity ions A^{Z+} [106, 107]:

$$A^{Z+} + D^0 \quad \rightarrow \quad A^{(Z-1)+^*} + D^+ \quad \rightarrow \quad A^{(Z-1)+} + h\nu + D^+. \tag{4.1}$$

The subsequent decay of the excited state of the impurity ions leads to the emission of a photon $h\nu$ at a specific wavelength. The resulting spectra contains information of the emitting ion species α. The ion temperature (T_α) and the flow velocity (v_α) is obtained from the Doppler width and Doppler shift and the impurity density (n_α) from the radiance of the emission line.

Typically, CXRS diagnostics measure charge exchange between low-Z impurities and injected neutrals from either diagnostic or heating beams (neutral beam injection, NBI). Low-Z impurities, such as boron or nitrogen, are mostly fully ionized throughout the whole plasma and therefore, allow to measure a specific line emission from the edge to the core. This is not the case for high-Z impurities whose emission from a given transition is localized where the specific charge state of the ion exists. Moreover, their concentration is typically too low for CXRS measurements. The use of NBI is required to obtain measurements up to the plasma core where the intrinsic neutral density is

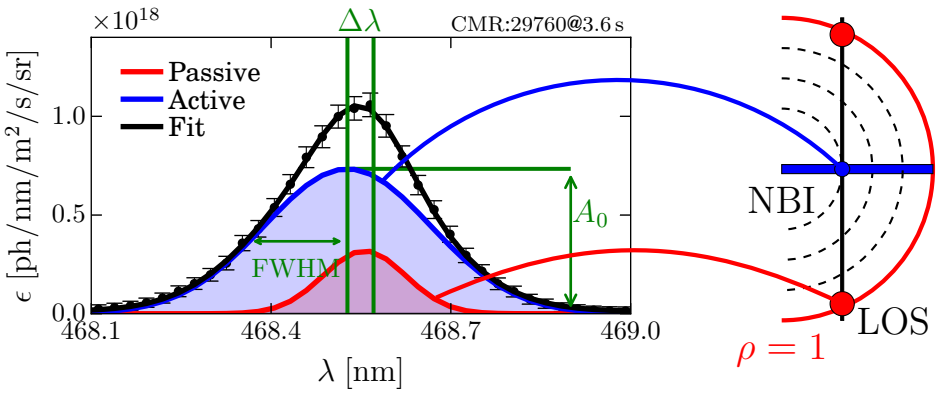

Figure 4.1: Example of CX spectra at the plasma edge: active (blue) and passive (red) form the measured spectra. The fit (black) needs to account for both components. On the right-hand side a sketch of a CX LOS viewing the plasma is shown: the active radiation originates from an localized region where the LOS intersects the neutral beam whereas the passive is from a less defined volume close to the separatrix.

too low. Additionally, by looking across the beam path the CX signal is localized and hence radial profiles of T_α, v_α and n_α can be obtained. This is usually possible up to the separatrix because in the scrape-off layer (SOL) the fully ionized low-Z impurity concentration strongly decays.

An example of CXRS spectra measuring the $He^{2+}(4 \rightarrow 3)$ line emission is shown in figure 4.1. Two components form the measured spectra: (i) the active signal (blue) given by the CX reaction with the injected neutrals, (ii) the passive signal (red) given by electron or ion impact excitation of the $A^{(Z-1)+}$ or CX with the thermal neutrals. The active signal originates from a localized area where the LOS intersect the neutral beam, while the passive radiation is emitted in an less well-defined region close to the separatrix. To extract localized information, either both components need to be fitted together or the passive signal needs to be determined via beam modulation and then subtracted (for further details see section 4.6). Assuming that the impurity ions have a Maxwellian velocity distribution, i.e. that they are thermalized, their line emission has a Gaussian line shape:

$$I_{\mathrm{CX}}(\lambda) = I_0 \sqrt{\frac{m_\alpha c^2}{2\pi k_B T_\alpha \lambda_0^2}} \cdot \exp\left(-\frac{m_\alpha c^2}{2k_B T_\alpha} \frac{(\lambda-\lambda_0)^2}{\lambda_0^2}\right) \tag{4.2}$$

where I_{CX} is the line shape function of the CX line normalized to a radiance of 1, I_0 the observed maximum of the spectral radiance, m_α and T_α the mass and temperature of the species α, λ_0 the theoretical wavelength of the measured spectral line, c the speed

of light and k_B the Boltzmann constant.

The temperature of the species α is therefore determined from the full width at half maximum (FWHM) of the fit of the active spectral component (Figure 4.1):

$$T_\alpha = \frac{m_\alpha c^2}{8\ln(2)\lambda_0^2 e^2}\mathrm{FWHM}^2. \tag{4.3}$$

However, due to the presence of the magnetic field, the measured temperature has to be corrected for the Zeeman splitting effect [8]. When all Zeeman components are added up, the width of the Gaussian overestimates the true ion temperature. A correction factor is routinely used to correct the apparent T_α measurements. The resulting temperature evaluation for the α species are assumed to be equal to the main ion temperature ($T_\alpha \approx T_i$) since the energy equilibration between impurities and main ions ($\tau_{\alpha,i}$) is typically one to two order of magnitude shorter ($\sim 10\,\mu s$) than the acquisition time ($\sim 1\,ms$). The limits of this assumption in case of fast measurements are examined in section 4.1.

From the Doppler shift of the active component of the line radiation ($\Delta\lambda$, Figure 4.1) the flow velocity of the ion species α ($\mathbf{v}_\alpha$) projected onto the LOS can be derived:

$$\frac{\Delta\lambda}{\lambda_0} = \frac{\mathbf{v}_\alpha \cdot \mathbf{u}_{\mathrm{LOS}}}{c} \tag{4.4}$$

where $\mathbf{u}_{\mathrm{LOS}}$ is the unit vector along the LOS. Apparent wavelength drifts due to charge-exchange cross-section effects or due to the gyro-motion effects [108] are found to be small, approximately 1.5 km/s in total, and hence not included in the standard analysis [8].

The spectral radiance of the active CX signal observed by a LOS of a CXRS diagnostic is given by:

$$L_{CX}(\lambda) = \frac{h\nu}{4\pi}\sum_{k=1}^{n_b}\langle\sigma_n v\rangle_{k,\lambda}\int_{\mathrm{LOS}} n_{\alpha,Z}\, n_k\, dl \tag{4.5}$$

where $n_{\alpha,Z}$ is the density of the impurity α in the ionization stage Z, n_k the beam neutral density, n_b the beam components and $\langle\sigma_n v\rangle_{k,\lambda}$ the CX rate coefficient of the specific transition including the velocity of the k-th beam component and the neutral density of each beam component n_k. The neutral density of the beam is modelled taking into account the beam geometry and the beam energy components [109]. The rate coefficient are obtained by the Atomic Data and Analysis Structure (ADAS) which is an interconnected set of computer codes and data collections for modelling the radiating properties of ions and atoms in plasmas [110]. Assuming a constant impurity density

along the intersection between the LOS and the beam, n_α can be derived from (4.5):

$$n_\alpha = \frac{4\pi}{h\nu} \frac{L_{CX}(\lambda)}{\sum_k \langle \sigma_n v \rangle_{k,\lambda} \int_{\mathrm{LOS}} n_{N,k} dl}. \tag{4.6}$$

Toroidal and poloidal aligned views of the plasma enable to measure the poloidal and toroidal projection of the plasma ion flow. In this way, through the radial force balance (equation (2.20)), the radial electric field can be calculated.

Thermal equilibration time

The time $\tau_{\alpha,\beta}$ required for two different plasma species α and β to reach a thermal equilibrium, i.e. a Maxwellian distribution, is given in seconds [111]:

$$\tau_{\alpha,\beta} = \frac{1}{1.8 \times 10^{-19}} \frac{(m_\alpha T_\alpha + m_\beta T_\beta)^{3/2}}{\sqrt{m_\alpha m_\beta} (Z_\alpha Z_\beta)^2 n_\beta \ln \Lambda} \quad [\mathrm{s}] \tag{4.7}$$

where m_α, m_β are the masses in AMU, T_α, T_β the temperatures in eV and Z_α, Z_β the charge states of the species α and β, n_β is the density of the species β in cm^{-3} and $\ln \Lambda$ the ion-ion Coulomb logarithm. If the integration time of the CX measurements of the impurity α is longer than $\tau_{\alpha,i}$, where i indicates the main ions, then the main ion temperature is roughly equal to the impurity ion temperature ($T_i \approx T_\alpha$). For typical edge conditions, $T_\alpha = T_\beta = 150\,\mathrm{eV}$ and $n_\beta = 2 \times 10^{19}\,\mathrm{m}^{-3}$, the thermal equilibrium between helium ($Z_{\mathrm{He}} = 2$, $m_{\mathrm{He}} = 4$) and deuterium ($Z_{\mathrm{D}} = 1$, $m_{\mathrm{D}} = 2$) is 50 µs, below the resolution of both fast and standard CX measurements. The equilibration time is even smaller for impurities with higher Z due to the square in the denominator in equation (4.7). Therefore the impurity ion temperature measured by CXRS is assumed to be the same as the main ion temperature.

4.2 Geometry of the upgraded edge CXRS systems

The ASDEX Upgrade tokamak is equipped with several charge exchange systems which cover the entire plasma volume, from low field side (LFS) to the high field side (HFS) [8, 112, 113]. An overview of some of the available systems is shown in figure 4.2. During this thesis, the edge poloidal and toroidal charge exchange systems also called CPR (Figure 4.2, blue) and CMR, respectively (Figure 4.2, red), have been upgraded. The total number of lines of sight has been increased from 16 to 50 compared to the old systems [8]. Moreover, the radial coverage has been reduced to roughly 6 cm in order to obtain detailed profiles without any radial plasma sweep.

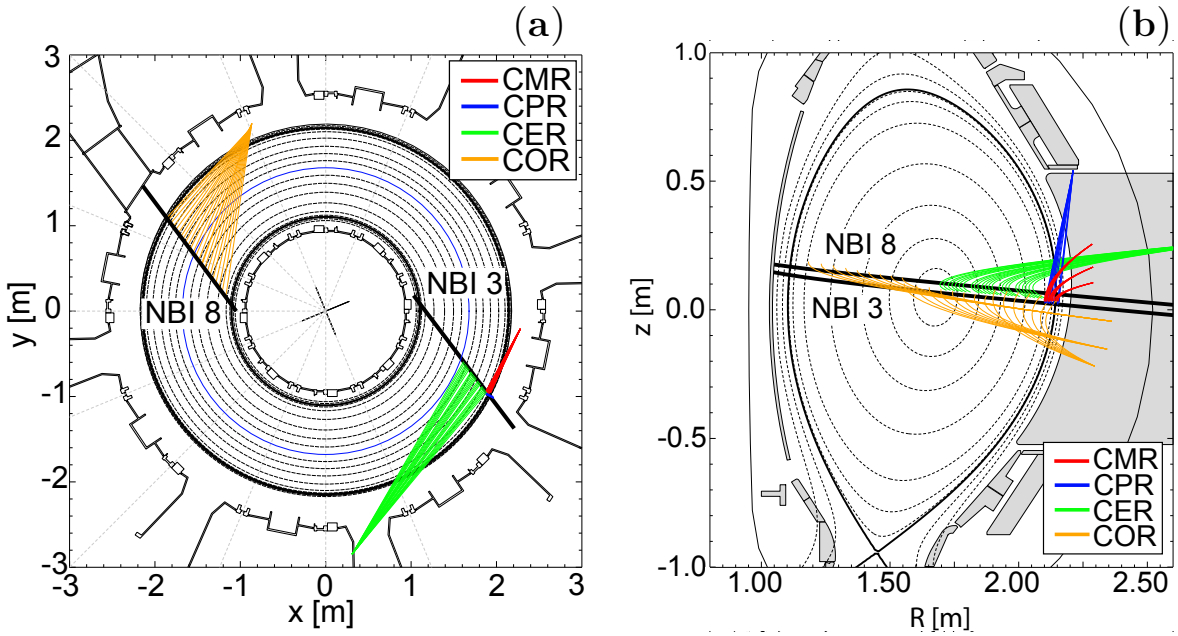

Figure 4.2: Overview of some of the CXRS systems at ASDEX upgrade: (a) top-view (b) poloidal-view. The edge charge exchange consists in CMR (red) and CPR (blue).

4.2.1 Edge toroidal charge exchange system

The toroidal edge charge exchange system (CMR) has been completely renovated during this thesis. The old system was characterized by parallel lines of sight focussed on beam #3 and realized with an individual mirror to optimize the resolution down to 3 mm [114]. The channels were separated by about 1 cm and each LOS was equipped with three fibers. This was the main limitation for this study: the radial distance between the lines of sight does not allow to measure detailed profiles without any plasma sweep and therefore single events, like the L–H transition, could not be investigated.

The old mirror-based system has been replaced in 2013 by three lens-based optical heads which provide 30 lines of sight separated by roughly 0.3 mm and focussed in a radial range of 6 cm at the low field side plasma edge. The radial resolution Δr is roughly 3 mm at the very edge and it increases towards the plasma center where the lines of sight are not anymore tangential to the flux surfaces where the LOS intersects the beam center. The optical heads are equipped with $f/2.7$ plano-convex lenses with a focal length of 85 mm. Collimators with magnetic shutters have been installed to protect the lenses from stray light and from eventual dirt emerging during glow discharges.

The collected light is transmitted by glass fibers with a diameter of 400 µm to a

high through-put $f/4$ Czerny-Turner spectrometer (see Figure 4.3). The spectrometer is equipped with a variable slit typically set to 50 µm, two objective lenses (Leica APO-ELMARIT-R) with each a focal length of 180 mm (entrance lens) and 280 mm (focussing lens), respectively [115], and a movable grating with 2400 grooves/mm. Twenty-five fibers with a diameter of 400 µm are imaged onto a Princeton Instruments ProEM charge coupled device (CCD) camera with on-chip multiplication gain featuring a 512×512 16 µm pixel chip [116]. The time resolution is set by the reading-out time ($f_{\mathrm{RO}} = 10 \times 10^6$ pixel/s), by the shifting-time of the pixel to the reading out area ($v_s = 0.45$ µs/row) and by an offset required by the camera to clean the serial register and to apply the Pixel Bias Correction (PBC). The latter can be switched off for certain acquisition modes. The camera chip, including the frame transfer area (528 pixels) and the dark pixels ($12 + 12$ per side), features $(512 + 12 + 12) \times (512 + 528)$ pixels (see Figure 4.5). By binning the pixels onto which one channel is imaged, the number of rows which are read out reduces to the number of channels itself (n_{ch}) and hence the maximum repetition time is $\Delta t = 2.27$ ms for twenty-five channels.

The movable grating permits to select the central wavelength imaged onto the camera enabling the investigation of different CX impurity lines. Usually, the spectrometer measures the $B^{5+}(n = 7 \rightarrow 6)$ emission at 494.467 nm or the $N^{7+}(n = 9 \rightarrow 8)$ line at 566.937 nm. Alternately, He^{2+} or C^{6+} or Ne^{10+} are used for the measurements. Two channels are reserved for a neon lamp which provides a calibration spectrum on a shot-to-shot basis. This reduces systematic error on the wavelength calibration (more details about the wavelength calibration are given in section 4.4.1).

4.2.2 Edge poloidal charge exchange system

The edge poloidal charge exchange system (CPR) was first installed in 2010 and consists of a single lens-based optical head poloidally aligned on beam #3 [8]. The system is equipped with a $f/2.5$ plano-convex lens with a focal length of 40 mm. The resulting radial resolution is reduced by 2 mm compared to the toroidal system, i.e. $\Delta r_{\mathrm{CPR}} = 5$ mm, because the poloidal curvature of the plasma is not stronger than the toroidal one. The optical heads originally had 16 (2 binned together) lines of sight separated by 1.25 cm on the focal plane limiting, as for the toroidal system, the possibility to obtain detailed profiles in one single acquisition. The system has been upgraded during this work and now it provides twenty-two lines of sight radially separated by 5 mm. This required the installation of a new fiber holder into the optical heads whereas the remaining parts have been preserved.

The optical head is connected to a high throughput $f/4$ Czerny-Turner spectrometer, similar to the one used for CMR. The only difference compared to the toroidal spectrometer is the focal length of the objective lenses of 280 mm for both. Thus, only 16

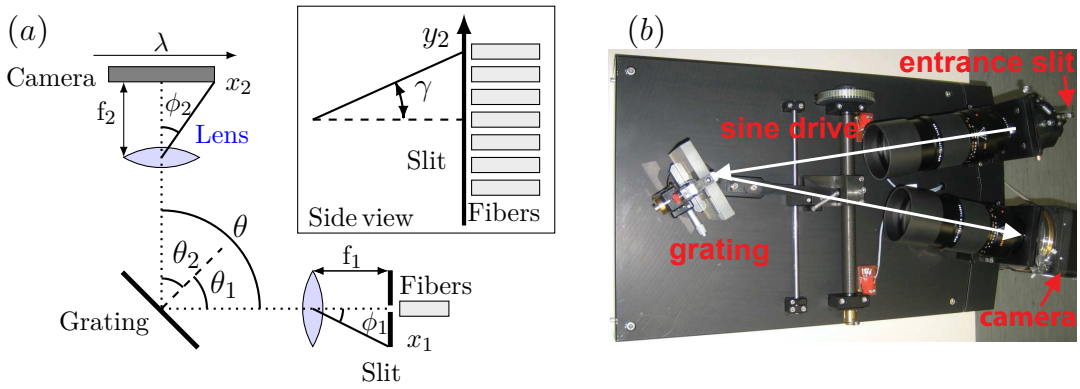

Figure 4.3: Schematic (a) and picture (b) of the high throughout $f/4$ Czerny-Turner spectrometer used for the toroidal edge charge exchange. The light coming from the entrance slit is collimated through an objective lens with $f_1 = 280\,\text{mm}$ onto a movable grating and re-focussed on a Princeton Instruments ProEM camera by a second lens with $f_2 = 180\,\text{mm}$. The opening angle θ of the spectrometer is 20° (adapted from [8]).

fibers with a diameter of 400 µm can be imaged on the camera chip. The dispersion, i.e. the variation in wavelength per pixel $\Delta\lambda/\Delta\text{pixel}$, of the spectrometer is also reduced allowing more detailed characterization of the spectral line. Thus, the small poloidal velocity can be better resolved. The maximum repetition time using the EM-mode could be reduced to 1.9 ms given the smaller number of rows to be read out, however, the time resolution is usually set to 2.3 ms to have simultaneous measurements of both edge CXRS systems.

4.3 A new approach for fast CXRS measurements

To increase the maximum repetition rate of a CCD camera the number of pixel (n_{pixels}) to acquire and/or the number of lines to shift have to be reduced. In figure 4.4, two examples of edge CX spectra acquired with the CMR spectrometer of the (a) He^{2+} and the (b) N^{7+} spectral lines are shown. The portion of the camera chip where the CX emission line is imaged (see highlighted regions in figure 4.4) is roughly 10 % of the active chip area for the CMR spectrometer. Hence, the number of pixels to be read can be strongly reduced. However, this cannot be done at the software level because the time consumed by the camera to discard a pixel in the horizontal direction is equivalent to read it out.

During this thesis, a re-design of the conventional Czerny-Turner spectrometer described in section 4.2 has been carried out in order to improve the temporal resolution of the system (see figure 4.4c). In the following, this spectrometer is called CNR. A

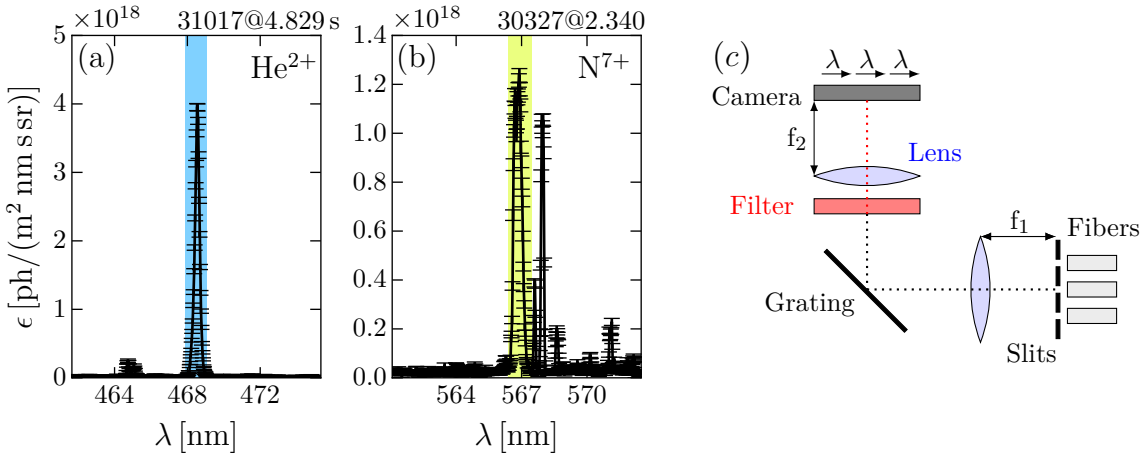

Figure 4.4: Example spectra centered around two different CX emission lines: (a) He^{2+} and (b) N^{7+}. The highlighted regions indicate the active line of the spectra and the color corresponds approximately to the wavelength of the emitted photon. (c) Schematic of the spectrometer which allows fast CX measurements. At the spectrometer entrance parallel slits are installed to image several channels on a chip row while an interference filter avoids overlapping between the spectra from different channels.

narrow interference filter, shown in red in figure 4.4c , has been installed between the grating and the second focussing lens in order to select only the interesting 10 % of the total diffracted light. In this way several channels can be arranged along the wavelength axis (λ) without overlapping between neighbouring lines. To do this, nine 50 µm fixed slits have been installed at the spectrometer entrance which allow to acquire several channels simultaneously on a single chip row. In case of the He^{2+} CX line, nine channels can be imaged together while for the N^{7+} only five are possible. Only N^{7+} and He^{2+} CX emissions are considered here as possible application for fast CX measurements because their concentration in the plasma can be manipulated by external gas puffing ("seeding"). This is a fundamental requirement to increase the signal to noise ratio when a high repetition time is used. Finally, the opening angle θ has been increased to 30° in order to allow the installation of brighter objective lenses of $f/2$ and $f/2.8$, keeping constant the focal lengths, of 180 mm and 280 mm respectively.

The vertical image of a fiber covers roughly an area of 20 pixels. The maximum repetition time for the CNR using the standard frame transfer acquisition mode can be reduced to 0.71 ms. A further increase of the temporal resolution is obtained by reducing the vertical chip size by the custom chip mode. Skipping the serial register cleaning and not applying the PBC, the maximum repetition time is 0.22 ms for 38 vertical rows. The custom chip mode can be applied only following precise rules in order to not interfere with the GigE Data Transfer requirements (see [116]). The acquisition

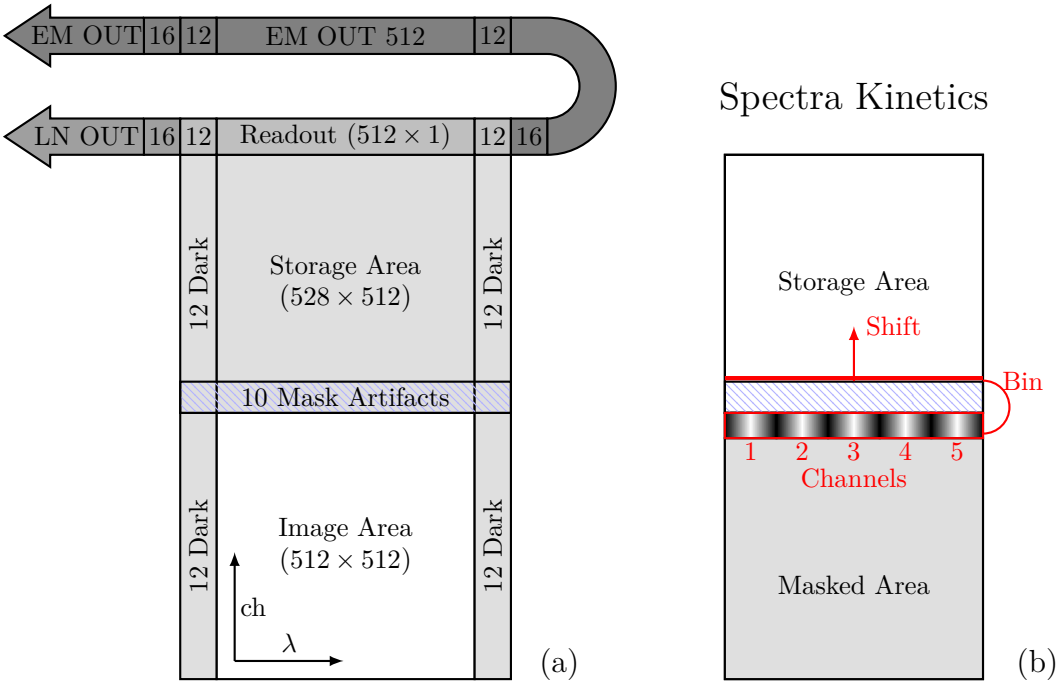

Figure 4.5: Schematic of: (a) the camera chip dimension, (b) the operation of the spectra kinetics acquisition mode.

mode which provides the best performance is the spectra kinetics mode (see Figure 4.5b). This mode exploits the capability of the camera to shift the chip rows on a micro-second time scale. Here, a certain number of rows n_r, after being exposed, are binned together at the entrance of the storage area and transferred into its first row. As shown in figure 4.5b, if the rows where the light is shaded are just below the storage area then the repetition time is equal to $\Delta t = (n_r + 10)v_s$. The resulting acquisition time for $n_r = 20$ pixels, i.e. the vertical dimension of the fiber image, is $\Delta t \approx 15\,\mu s$. This can be further reduced down to $\approx 5\,\mu s$ by imaging just a part of the fiber onto the camera chip. The process of binning and shifting can be repeated only until the storage area is filled, i.e. 528 times. Afterwards, the entire chip has to be read out such that a new burst of exposures can start. The reading out lasts $(512 + 12 + 28) \cdot f_{RO} \approx 30\,ms$.

The capability of performing CX measurements on a 10 to 20 µs timescale is limited by the low signal to noise ratio. Therefore, external impurity seeding is required to increase the intrinsic impurity content. In this work, by means of N or He puffing, good signal to noise ratio measurements have been obtained with a time resolution between 60 and 100 µs. This opens up the possibility to study the behaviour of the ions during fast phenomena like the L–H transition (see chapter 5) and the connected fluctuations (see chapter 6), as well as the dynamics during the edge localized modes (see chapter 7).

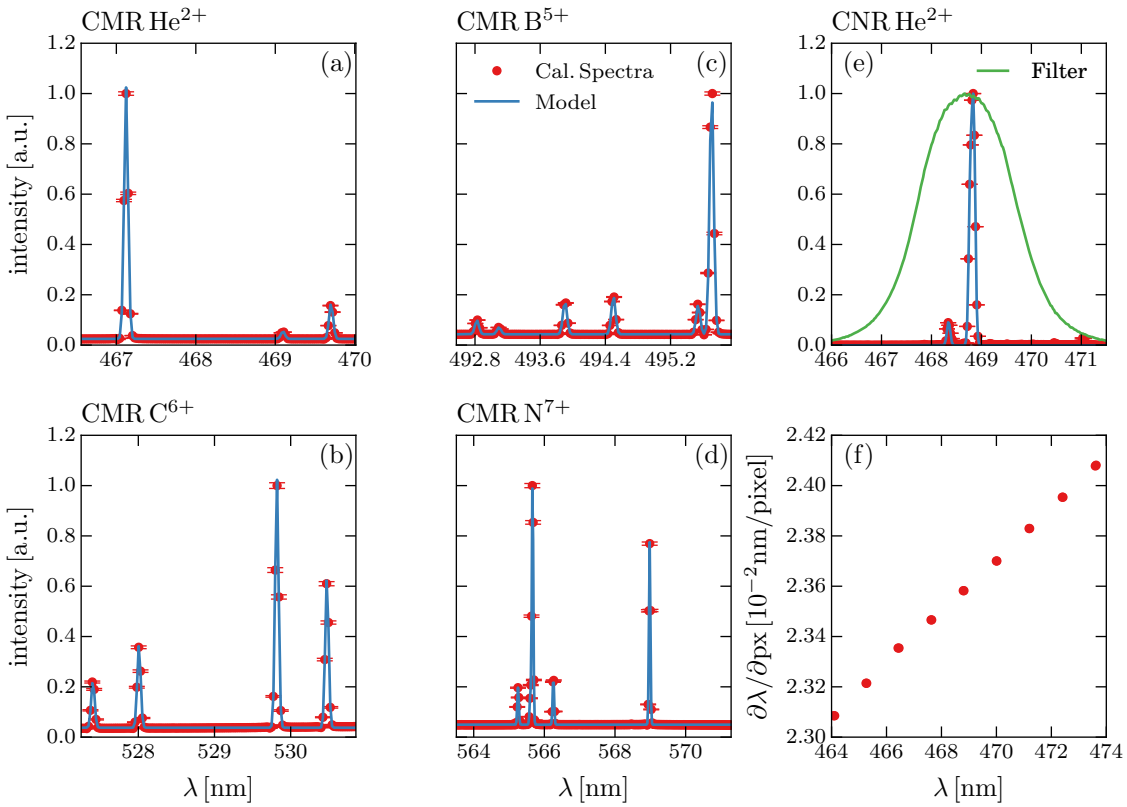

Figure 4.6: Forward modelling of calibration spectra for the spectrometer CMR (a-d) and CNR (e) in the range of the main CX emission lines. In red the acquired spectra of the Xe lamp (a), Ne lamp (b-d) and Zr lamp (e) are shown. The reconstructed spectra from the forward model is indicated in blue. (f) First oder dispersion of the channels in front of different slits of the CNR spectrometer as a function of the central imaged wavelength.

4.4 Calibration and characterization

The interpretation of the CX measurements needs accurate calibration. Wavelength calibrations are required for velocity measurements and intensity calibration of the entire system (in-torus optical heads, connecting fibers, spectrometer and camera) is necessary for determining the impurity density. Moreover, the instrument function of the system has to be characterized to deconvolve the Doppler broadening from the imperfections of the system optics and hence to measure the impurity ion temperature.

4.4.1 Wavelength calibration

The wavelength axis of a Czerny-Turner spectrometer is determined by the grating equation [117]:

$$ng\lambda = \cos\gamma(\sin(\theta_1 + \phi_1) + \sin(\theta_2 + \phi_2)) \tag{4.8}$$

where n is the diffraction order, g the number of grooves/mm of the grating, λ the wavelength, γ the vertical angle, of an off-axis ray, θ_1 and θ_2 the incident and the diffraction angle, respectively, ϕ_1 and ϕ_2 the horizontal angle, of the entrance slit and of the image plane, respectively (see figure 4.3). The horizontal distance from the optical axis on the image plane x_1 and on the slit plane x_2 are defined as: $\tan\phi_1 = x_1/f_1$ and $\tan\phi_2 = x_2/f_2$. On the optical axis ($\gamma = \phi_1 = \phi_2 = 0$), the chosen grating and geometry determine the central wavelength λ_0:

$$\lambda_0 = \frac{\sin\theta_1 + \sin\theta_2}{ng}. \tag{4.9}$$

For a fixed central wavelength λ_0, by differentiating equation (4.8) with respect to x_2 one obtains the linear dispersion[1]:

$$\frac{\partial\lambda}{\partial x_2} = \left(\frac{\lambda_0}{f_2}\right)\frac{\cos\gamma\cos(\theta_2 + \phi_2)\cos^2\phi_2}{\sin\theta_1 + \sin\theta_2} \tag{4.10}$$

The dependence of λ on γ produces a curved image of the slit for an emission line on the image plane. Assuming small angles $\gamma \ll 1$ and $x_2 \ll f_2$, equation (4.8) can be approximated as:

$$\Delta x_2 = \left(\frac{\lambda}{\lambda_0}\right)\frac{\sin\theta_1 + \sin\theta_2}{2f_2\cos(\theta_2 + \phi_2)}y_2^2 \tag{4.11}$$

and hence, the image of a vertical slit has a parabolic shape ($\Delta x_2 \sim y_2^2$). Additionally, a small displacement of the input fibers can produce deviations from the theoretical wavelength calculation.

In summary, the wavelength calibration is needed to determine the free parameters for the determination of the wavelength axis: the central wavelength λ_0, the focal length f_2, the vertical offset of the optical axis due to eventual misalignment Δh and the offset of every fiber from the central position Δx_{px}. In the framework of this work, a forward modelling has been developed to consistently fit together the calibration spectra of neon (Ne) and xenon (Xe) lamps in the wavelength ranges centered on CX emissions of He^{2+}, B^{5+}, N^{7+} and C^{6+} using the previous quantities as free parameters. The reference wavelength for the Ne and Xe lamps have been taken from the NIST Database [118].

[1] $\cos^2(\arctan x) = 1/(1 + x^2)$

In the forward modelling, parameters for the instrument function of every channel and for the intensity of every calibration line have been included to better reconstruct the calibration spectra. An example of the calibration spectra and their fits for one channel of the CMR spectrometer is shown in Figure 4.6a-d. Only the central part of the chip has been considered for the calibration in order to reach the best accuracy for the interesting part of the wavelength range where the emission line is measured. The same approach has been used for the CNR spectrometer where every slit can be considered as an independent spectrometer with a different opening angle. Therefore, for a fixed sine drive position, the imaged central wavelength and the dispersion changes for every vertical slit (see Figure 4.6f). Here, the effect of the interference filter on the line shape is taken into account by deconvolving the calibration spectra with the shape of the filter (see Figure 4.6e). The accuracy of the calibration procedure is about 2 pm, i.e. roughly 1 km/s.

To reduce systematic errors, an additional calibration is performed on a shot to shot basis. This accounts for possible air temperature or pressure changes which can affect the wavelength calibration or for mechanical uncertainties of the sine drive. A neon lamp is automatically switched on after every discharge on two dedicated channels, one imaged at the top of the chip and one at the bottom. Single gauss-fits of the emission lines allow to identify possible shifts in the wavelength axis. These are then applied as rigid shifts of the wavelength axis, i.e. the dispersion is kept constant. A cross-check of this assumption is obtained by comparing the channels at the opposite sides of the chip: if the wavelength shift obtained from the two channels is constant then the dispersion and the vertical offset of the optical axis have not changed. The calibration of the CNR spectrometer requires more care due to the presence of the interference filter. The filter is subject to variations in trasmittence and shape in case of changes of the ambient temperature. Therefore complete dedicated calibrations, as described previously, are performed before and after the discharges of interest.

4.4.2 Intensity calibration

An intensity calibration of the entire system is necessary to evaluate the impurity density. In practice, the sensitivity of every channel has to be determined to convert the measured counts into photons at every wavelength. A standard calibration source (Labsphere, Model Unisource 1200) with a known spectral radiance has been used to calibrate the whole system. The spectral radiance as a function of the wavelength is shown in Figure 4.7a. First, the sphere has been placed in front of the in-torus optical heads and the transmitted light has been measured at different wavelengths for all the various fibers (see Figure 4.7b). Second, a radiance calibration of every spectrometer channel has been performed in order to obtain a transmission factor for each line of

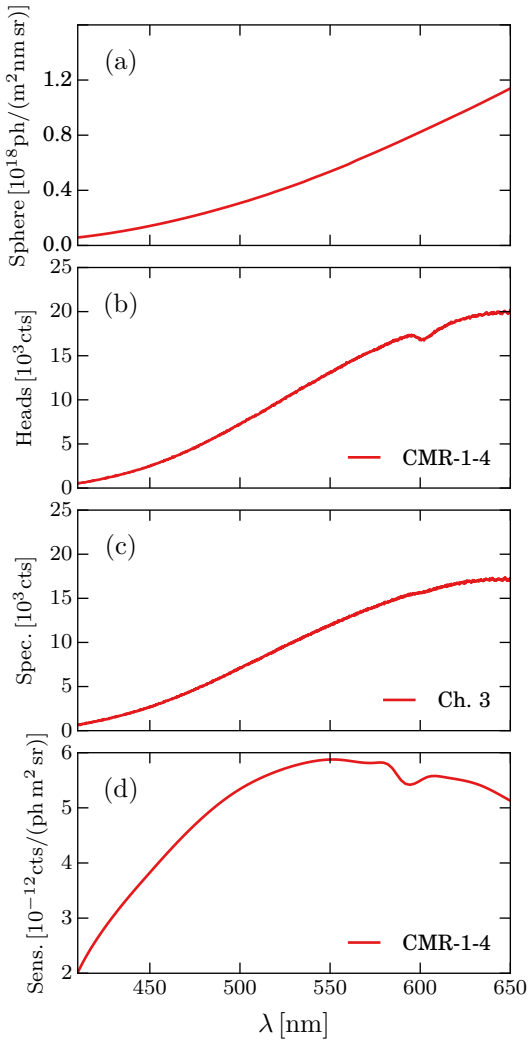

Figure 4.7: Intensity calibration procedure: (a) Radiance of a standard calibration source, (b) Calibration of the in-torus optical heads, (c) Calibration of the spectrometer channel used for (b), (d) Resulting sensitivity.

sight (see Figure 4.7c). The resulting sensitivity is shown in Figure 4.7d. The dip in the light transmission at roughly 600 nm is due to the glass fibers absorption and it is stronger for the optical head calibration since the fibers are longer.

The radiance calibration is performed as a function of the wavelength. While the spectrometer grating is turned, the acquired spectra scan the entire visible wavelength range. The sensitivity S is a function of λ, of the pixels in the x direction (wavelength axis) and each channel, as the pixels in the y-direction are binned according to the various channel (see section 4.3). This allows to calculate the number of photons emitted

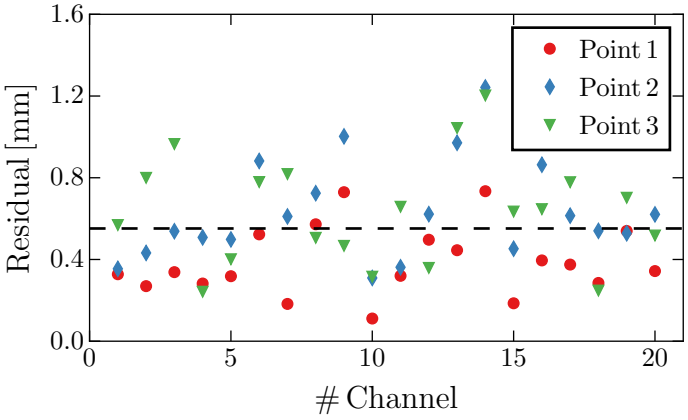

Figure 4.8: Residual of the fit of the CPR lines of sight geometry for every measured point (colors) for the different channels. The fit imposes that all the lines of sight pass through the measured lens position.

by a certain CX reaction and therefore, together with a model of the neutral beam, to reconstruct the impurity density.

Aging of fibers, deterioration of the in-vessel optical heads, dirt in the fiber connection and other effects may modify the sensitivity of each line of sight and spectrometer channel. In particular, the lines of sight are often switched between the fast and the standard spectrometers increasing the uncertainties in the radiance calibration often up to 20–30 %. However, assuming that the emissivity profile has to be smooth the sensitivity of every channel can be readjusted by a fudge factor not larger 20–30 %. During a constant plasma phase, the plasma position can be radially swept through the view of the LOS. In this way, by mapping the measurements on a radial profile, different channels overlap and therefore the recalibration is more accurate.

4.4.3 Spatial calibration

Precise alignment of the lines of sight is fundamental for the calculation of a radial profile and for maximizing the resolution where the LOS cross the beam. In case of the poloidally aligned LOS (CPR), it is even more critical. The poloidal velocity at the edge of the plasma is often smaller or of the same order of the toroidal velocity. Therefore, a misalignment of the radial position of the LOS can corrupt the poloidal velocity measurements and hence, the E_r calculation, since an unprecise poloidal alignment can lead to an unwanted contribution of the toroidal velocity being mixed to the poloidal rotation data. To avoid or to eventually correct this issue, the diagnostic was adjusted by back-lighting the optical fibers and by measuring points along every LOS using the 3D measurements technology provided by FARO [119]. The FARO technology

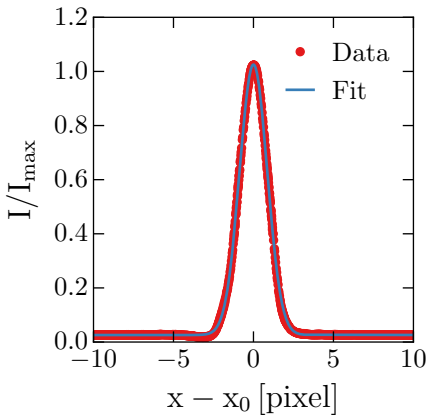

Figure 4.9: Characterisation of the instrument function of the spectrometer CMR for a slit width of 50 µm: (red) measured data points, (blue) one gauss-fit. For a slit width ≈ 50 µm the instrument function is well approximated by a single Gaussian function.

guarantees an accuracy of about 1 mm. Moreover, the position of the lenses of the optical heads were documented. A fit of the LOS geometry through the measured points assuming that all the lines of sight pass through the lens, provides an accuracy down to 1 mm for the geometry of the LOS. Figure 4.8 shows the residual of the fit of the CPR LOS for every measurement point as a function of the channel number. The average deviation is ≈ 0.55 mm.

4.4.4 Instrument function

The measured spectral line shape is the convolution of the Doppler broadening and the instrument function of the system. Assuming that the instrument function can be approximated by a sum of Gaussian shaped lines, the deconvolution can be performed analytically during the fitting procedure. The width of the measured line is determined by the root mean square of the instrument function and the Doppler broadening.

Calibration lamps (Ne or Hg) have been used to characterize the instrument function at different wavelengths. To obtain a sub-pixel resolution, the grating was slowly rotated such that the line is imaged at many different positions onto the chip. Since the change of the dispersion due to the small step size of the rotating grating is negligible, the wavelength axis is rigidly shifted during this scan. Therefore, the centre of the line at a certain grating position can be realigned and superimposed together with all the other samples. The result for a 50 µm slit width for the CMR spectrometer is shown in figure 4.9. In red the measured data points are shown, while in blue the single Gaussian fit is presented. The instrument function for a slit width of about 50 µm can be well approximated with a single Gaussian shaped line. The line width of the instrument

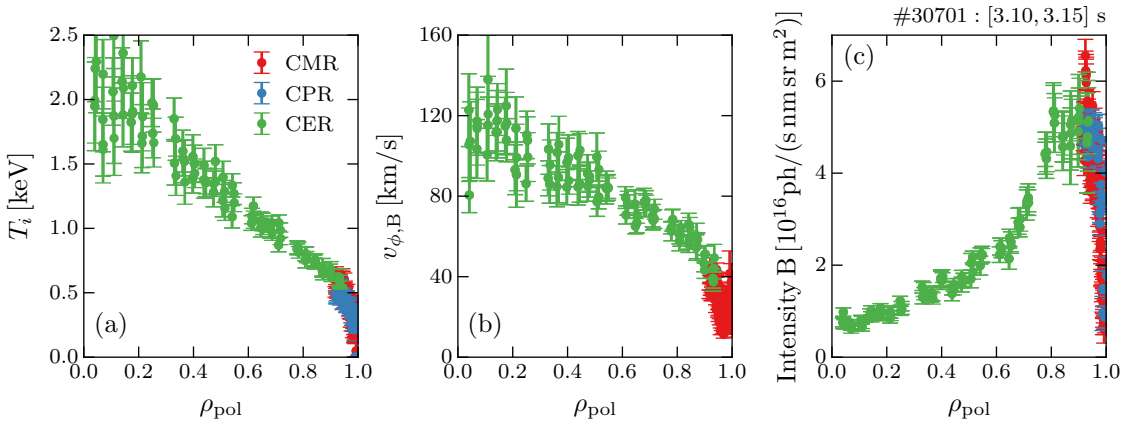

Figure 4.10: Radial profile of: (a) impurity ion temperature T_α, (b) toroidal velocity v_ϕ, (c) intensity of the B^{5+} CX line. By combining the edge (CMR: red, CPR: blue) and the core CXRS (CER: green) the entire T_α and v_ϕ can be plotted and hence the measurements cross validated.

function corresponds to the apparent temperature of about 26 eV for He^{2+}, 20 eV for B^{5+} and 16 eV for N^{7+}.

4.5 Validation of the edge CXRS measurements

By combining the edge and the core CXRS systems, the entire radial profile of the ion temperature and the toroidal velocity can be measured enabling a cross validation of the different systems. Figure 4.10 shows an example of radial profiles of $T_{B^{5+}}$ (a), $v_{\phi,B^{5+}}$ (b) and the intensity of the boron CX line (c) from the plasma edge to the core. Good agreement is found between the different CXRS systems [8]. A rigid re-alignment of the profiles of about 5 to 10 mm due to uncertainties in the magnetic equilibrium reconstruction is often required to reach a better agreement between the profiles.

4.6 Conditional synchronization of passive and active radiation

To obtain localized CX measurements, the passive and the active radiation needs to be distinguished. This is usually performed by fitting the measured spectral line with two Gaussian curves as shown in Figure 4.1. Certain constraints are often set to the fit to reach a better convergence stability such as fixed Doppler shift and/or width of the passive radiation. However, if the temperature gradients at the plasma edge

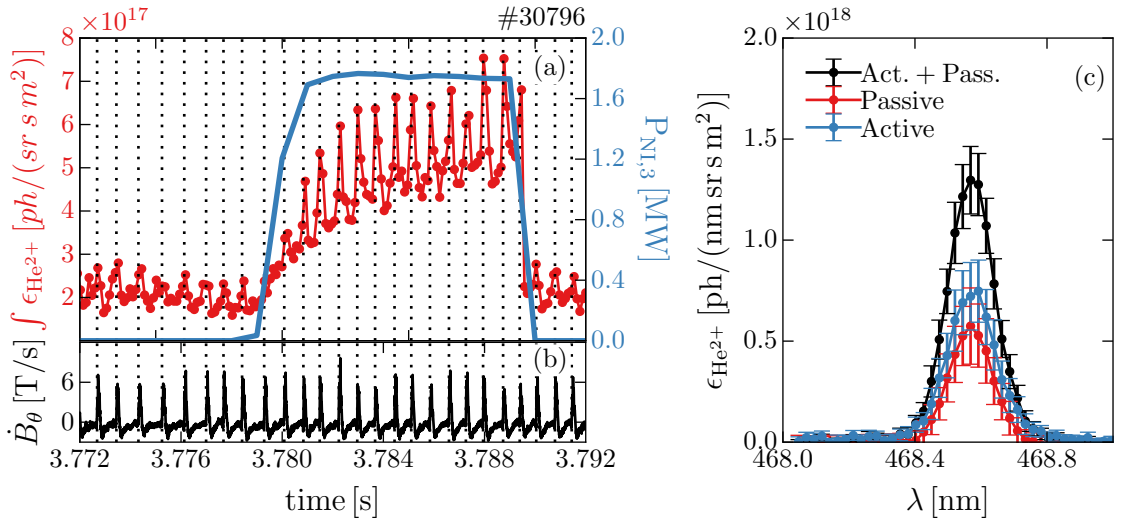

Figure 4.11: Passive radiation subtraction via beam modulation and Conditional synchronization: (a) Time-traces of the integral of the He^{2+} line emission (red) and the neutral beam NBI#3 (blue), (b) $\dot{B}_\theta$ from the coil C09-23 (see Figure 3.4), (c) Comparison between the active (blue) and the passive (red) spectra components and the sum of two (black) in the time window $t \in [-200 + t_0, -100 + t_0]$µs synchronized to the onset t_0 of the I-phase bursts (see dashed lines in a and b).

are not steep, as for example in L-mode or close to the L-H transition, the emission layer of the $(Z-1)^+$ impurity ions extends further into the plasma. Thus, the passive emission is less localized and therefore has a non Gaussian shape and can be similar to the active radiation at the plasma edge. This effect is particularly extreme for the He^{2+} CX emission because the passive radiation is mostly dominated by electron impact excitation and hence, proportional to the He^{1+} concentration.

An alternative to the combined fit of active and passive radiation is to switch on and off the neutral beam repetitively to properly monitor and then subtract the passive contribution. However, as for the Li-BES diagnostic (section 3.1.1), single events like ELMs affecting both passive and active component on a faster timescale than the beam modulation need special treatment. Figure 4.11 shows an example of beam modulation during an I-phase. Every I-phase burst (figure 4.11b) affects both passive and active contributions of the CX spectra such as the integral of the CX emission (figure 4.11a, red). The intensity of the emission is modulated with the I-phase frequency in both beam-on and beam-off phases (figure 4.11a, blue). To properly account for the fast changes of the passive spectra and to reliably extract only the active component without using constraints for the fit, the acquired spectra in beam-on and beam-off phases have been separately conditionally synchronized to the onset of the I-phase bursts

t_0 through the $\dot{B}_\theta$ signal from the C09-23 Mirnov coil (Figure 4.11b, dashed line). Hence, the passive radiation can be properly subtracted from the total CX spectra accounting for its evolution in time. Figure 4.11(c) shows the synchronized passive (red) and total (black) spectra in the time window $t \in [-200 + t_0, -100 + t_0]$µs, and the resulting active component (blue). This analysis procedure is similar to the one presented in section 3.1.1 for the Li-BES diagnostic. The approach of synchronizing and averaging data at the spectra level does not only provide the advantage of a more reliable treatment of the passive radiation but it also reduces the uncertainties of the synchronized radial profiles. The binning of the raw data improves the signal to ratio leading to a more reliable fit of the data.

5 Connecting macro to micro: the power threshold and the radial electric field

It is widely accepted that $\mathbf{E}\times\mathbf{B}$ velocity shear, caused by the radial electric field E_r, is responsible for the suppression of turbulence and therefore for the establishment of (ETB) which is the characteristics feature of the H-mode [7]. The formation of the ETB coincides with the transition from the low (L-) to the high confinement mode (H-mode) and is triggered when the heating power exceeds a certain threshold P_{thr}, which has the following inter-machine scaling [46]:

$$P_{\mathrm{thr,scal08}} = 0.049\,\bar{n}_e^{0.72}\,B_\phi^{0.80}\,S^{0.94}. \tag{5.1}$$

The scaling gives the required power in MW for a given density in $10^{19}\,\mathrm{m}^{-3}$, magnetic field in T and the plasma surfaces in m^2. A physics-based model of the L–H transition power threshold is needed to confidently extrapolate the auxiliary heating requirements for future devices. Correlations between the E_r profile just before the confinement change and the power threshold are investigated here in order to experimentally relate the macroscopic effects of P_{thr} to the microscopic $\mathbf{E}\times\mathbf{B}$ velocity shearing of turbulence. In particular, the minimum of the E_r well as shown in figure 2.5, used as proxy of ∇E_r [120], is examined for discharges with different L–H power thresholds obtained via a variation of electron density, magnetic field and isotope mass (deuterium and hydrogen).

5.1 Dynamics of the L–H transition

In order to address the $\mathbf{E}\times\mathbf{B}$ velocity shear condition for the H-mode onset, it is necessary to understand the dynamics of the L–H transition process and to define a time point where the plasma changes its confinement state thus enabling a comparison of different discharges. A series of discharges has been performed where several L–H and H–L transitions have been induced by slowly ramping the input power up and

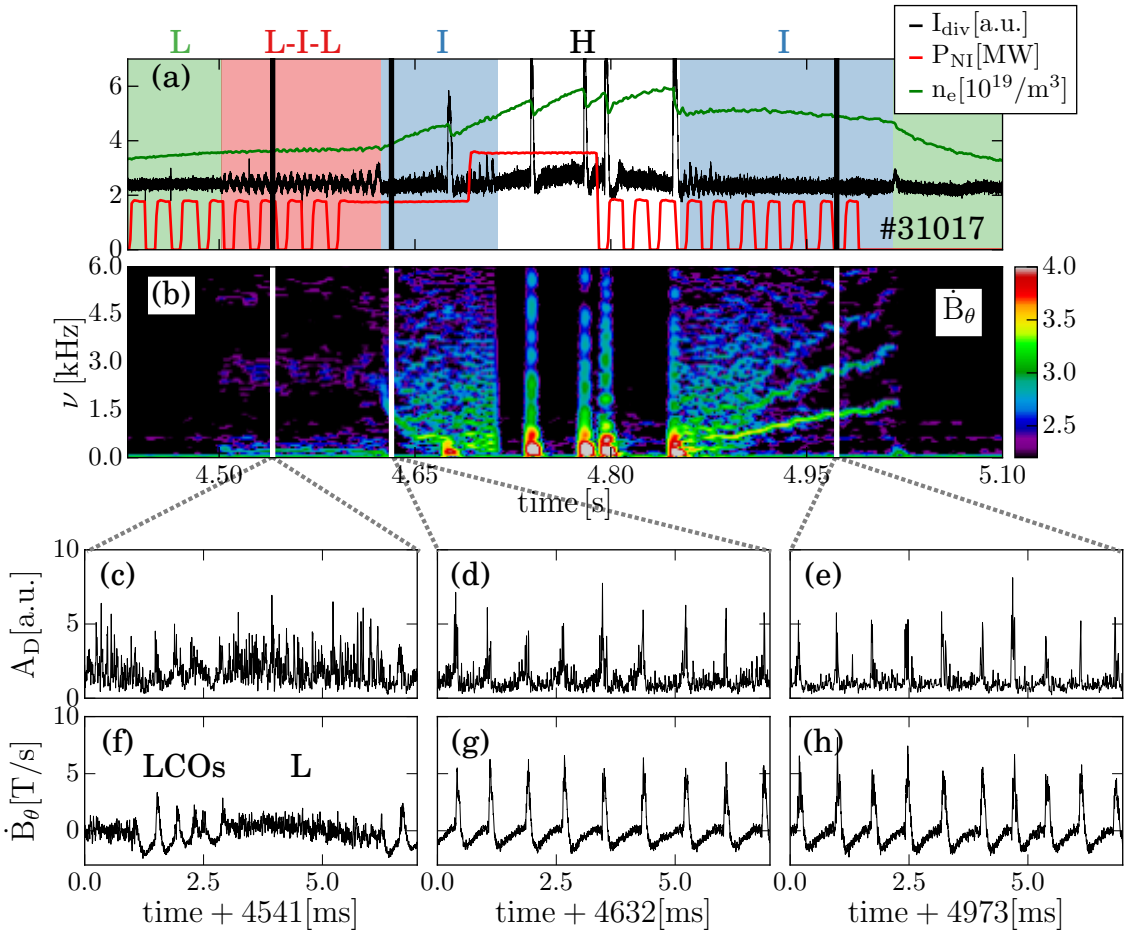

Figure 5.1: Example of an ASDEX Upgrade discharge with NBI induced L–H and H–L transition. (a): NBI input power P_{NI} (red), line integrated edge electron density n_e (green), divertor shunt current I_{div} (black). (b) spectrogram of $\dot{B}_\theta$ measured at the high field side. (c,d,e)/(f,g,h) turbulence amplitude at the edge measured by Doppler reflectometry $A_D/\dot{B}_\theta$ measured during the L–I–L oscillations (c,f) and during the LCO close to the L–H (d,g) and H–L transition (e,h).

down. Figure 5.1 shows the time evolution of a discharge where neutral beam injection (NI) is used to induce L–H–L transition sequences and to allow active charge exchange measurements. In figure 5.1a, the time traces of the input power P_{NI} (red), the line integrated edge electron density $n_{e,edge}$ (green) and the divertor current I_{div} (black) are presented. The input power is ramped up and down by changing the duty cycle of the beam on and off phases. In this way the passive and active CX spectra components are monitored as described in section 4.6. The divertor tile shunt current I_{div} is an indicator of heat and particle fluxes reaching the divertor plates and is often used in metal

divertor tokamaks as an L–H transition monitor signal. When a transport barrier forms, the power flow out of the plasma is reduced leading to a drop in I_{div}. Figure 5.1b shows the spectrogram of the poloidal magnetic field fluctuation ($\dot{B}_\theta$) measured by the C09-09 Mirnov-coil located above the upper divertor of AUG (see figure 3.4). Two distinct fluctuating phases in the evolution from L-mode (highlighted in green) to H-mode (white) and back to L-mode are identified: (i) repetitive L–I–L transitions (highlighted in red) with a frequency of around 200 Hz, (ii) an extended I-phase characterized by limit cycle oscillations at the L–H and the H–L transitions (highlighted in blue), visible in the spectrogram as harmonics. The presence of the I-phase at the L–H and H–L transition has previously also been reported in other machines [62, 70, 121]. The L–I–L dithers are characterized by transitions from a highly turbulent state (L-mode) to the typical turbulent bursts of the limit cycle oscillations (LCOs, figure 5.1c). The turbulence level at the plasma edge A_{D}, measured by Doppler reflectometry, correlates with the $\dot{\mathrm{B}}_\theta$ signal (figure 5.1f): the spikes of the LCOs are followed by quiet phases while in L-mode a continuously high fluctuation level is found. The same correlation is found during the I-phase close to the L–H (figures 5.1d,g) and H–L (figures 5.1e,h) transitions.

In the following two sections, the macroscopic characteristics of the I-phase and the L–I–L dithers are analysed. The details about the profiles and the E_r evolution in these phases are reported in chapter 6.

5.1.1 Structure of the limit cycle oscillations during the I-phase

The magnetic structure of the I-phase at ASDEX Upgrade is described in detail in [77]. In this section, the main characteristics of the single limit cycles within the I-phase are reported and the confinement properties of the I-phase are investigated.

The I-phase is characterized by regular pulsations, often called limit cycle oscillations (LCOs), in the low kilohertz range which occur at the plasma edge. Figure 5.2 shows the onset of the LCOs observed by different diagnostics: (a) divertor shunt current, (b) turbulence amplitude at the edge measured by Doppler reflectometry, (c) $\dot{B}_\theta$ and (d) a bolometer channel viewing at the magnetic X-point. Here, a low-pass Chebyshev filter ($f_{\mathrm{pass}} = 60\,\mathrm{kHz}$, $f_{\mathrm{stop}} = 100\,\mathrm{kHz}$) is applied to remove high frequency components from the signals [122]. The fluctuations of the particle and heat fluxes coming to the divertor (figure 5.2a) and of the emitted radiation at the X-point (figure 5.2b) indicate that every pulsation is an instantaneous increase of the transport close to the separatrix and in the scrape off layer [62, 63, 66]. The effects of the I-phase on the magnetic X-point where firstly observed in [123]. The spikes in $\dot{B}_\theta$ result in harmonics once the Fourier transformation is applied (see also figure 5.1). The I-phase pulsation is often

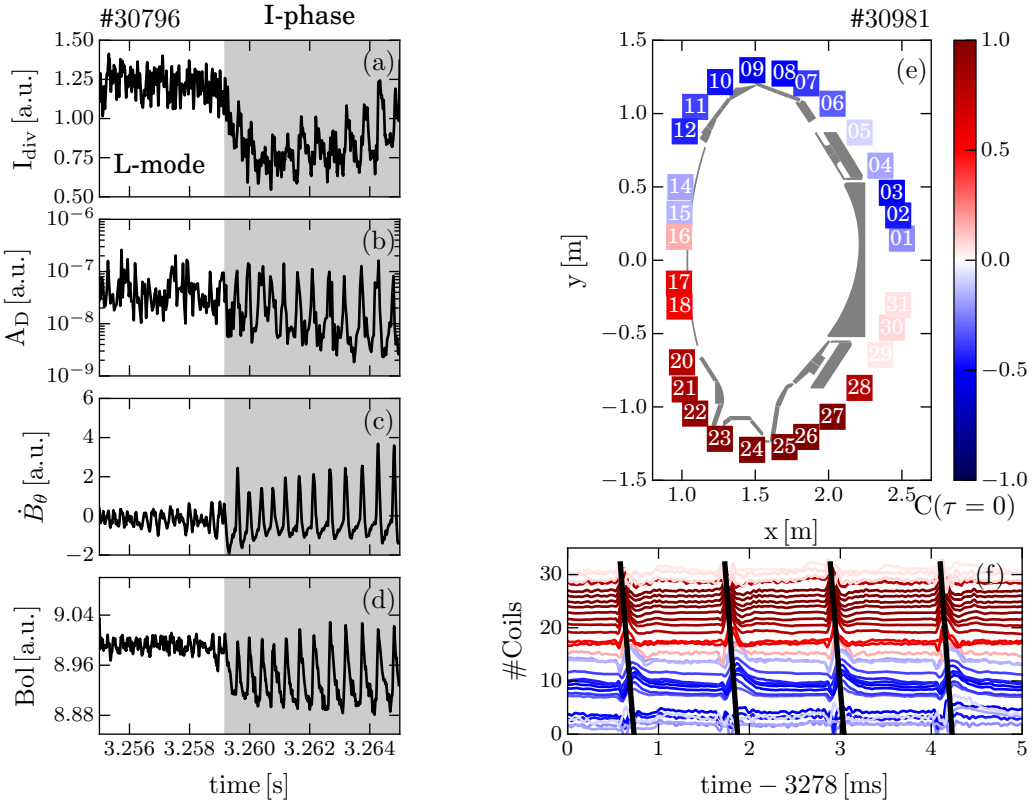

Figure 5.2: Onset of the I-phase measured by different diagnostics: (a) divertor shunt current, (b) turbulence amplitude at the plasma edge measured by Doppler reflectometry, (c) poloidal magnetic fluctuation measured by the C09-23 Mirnov Coil (see figure 3.4) and (d) radiation close to the X-point measured by a bolometer channel. Magnetic structure of the I-phase pulsations: (e) cross correlation of the poloidal array of Mirnov coils C09-xx (see figure 3.4) at $\tau = 0$ using as reference signal the C09-25 coil, (f) normalized signal of the Mirnov coil poloidal array C09-xx ordered by the coil position. The colors of the signals correspond to the colors in subfigure (e).

proceeded by a similar fluctuation but with a smaller amplitude, firstly identified at the EAST tokamak and named small-amplitude oscillations [67, 124]. The small-amplitude oscillations are usually less regular with respect to the normal LCO, but exhibit similar features of turbulence-flow interactions at the plasma edge. These are, however, not always present before the I-phase onset.

The I-phase pulsations have a clear magnetic structure (figure 5.2e,f). The effect of the LCO on the magnetic measurements has been reported in several machines [62, 67, 69, 70]. The cross-correlation of the poloidal array of Mirnov coils C09-xx (see figure 3.4) with respect to the signal of coil C09-25 at $\tau = 0$ presents an up-down asymmetry as shown in figure 5.2e. Here the colors indicate the level of cross-correlation with red

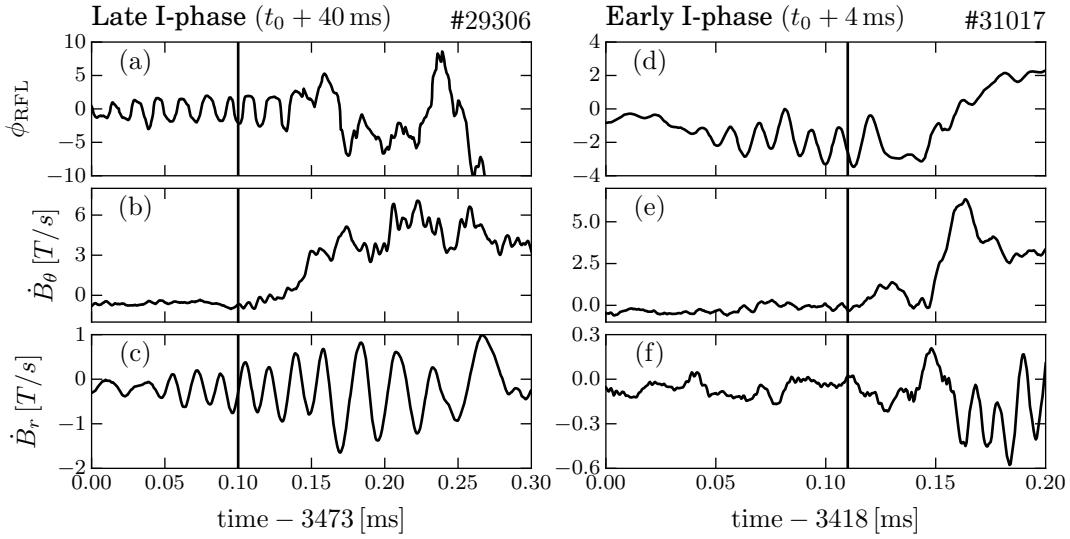

Figure 5.3: Example of precursor to the LCOs during the I-phase. Late I-phase, 60 ms after the L–I transition t_0 (a-c): a clear precursor is visible in $\dot{B}_r$ (c) and the unwrapped hopping reflectometry phase ϕ_{RFL} (a). Early I-phase, 4 ms after t_0 (d-f): no precursor is detected by the $\dot{B}_r$ (f) coil while it is still visible in the ϕ_{RFL} (d). A precursor is here defined as a fluctuation with a frequency of the order of 100 kHz visible before the onset of the pulsation, i.e. before the rise of $\dot{B}_\theta$ signal (b,e).

being a high level of cross-correlation and blue of anti-correlation. The asymmetry can be better interpreted by looking at the normalized raw signal shown in figure 5.2f where the different colors indicate the different coils shown in figure 5.2e. The magnetic perturbation propagates from the X-point to the top along the high field side in $\tau \approx 130\,\mu$s (see black line), consistent with the observations from EAST [124]. The propagation velocity of the LCO pulse can be determine as $v_{\mathrm{pulse}} = L_\parallel/\tau \approx 90\,\mathrm{km/s}$, where $L_\parallel$ is the parallel connection length $L_\parallel \approx qR_0 = 11\,\mathrm{m}$. The velocity agrees well with the sound speed $c_s = \sqrt{T_e/m_i}$ at the plasma edge [77]. The $\dot{B}_\theta$ signature of a single pulse remains unchanged during the whole I-phase, while the characteristics of the radial component, $\dot{B}_r$, evolves. In 5.2c a 100 kHz fluctuation is observed reminiscent of the ones called "precursor" seen just before type-III ELMs (cfr. section 2.4.2) [55, 125–128]. The precursor is usually not visible at the beginning of the I-phase and it gradually appears in the later pulsations. This is often used to discriminate between LCOs and type-III ELMs. Figure 5.3 shows a comparison between the $\dot{B}_\theta$ and $\dot{B}_r$ signals 40 ms (a-c) and 4 ms (d-f), respectively, after the L–I transition (t_0). A clear precursor is visible in the $\dot{B}_r$ signal in the late I-phase (c), while in the early I-phase it is not present (f). A precursor is defined as a fluctuation with a frequency of the order of 100 kHz, which is visible before the onset of the pulsation, i.e. before the rise of the

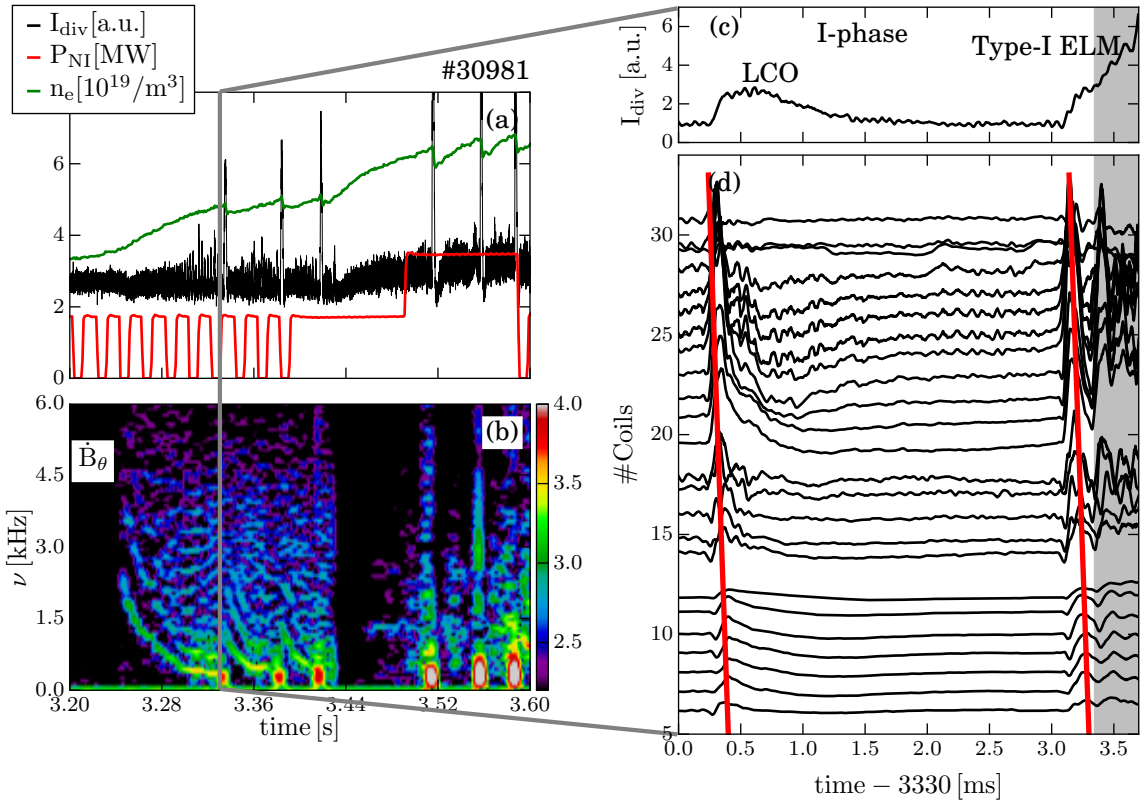

Figure 5.4: Late I-phase interrupted by type-I ELMs: (a): main time traces: edge line integrated electron density (green), divertor shunt current (black), NBI input power (red). (b): spectrogram of the Mirnov coil C09-09. (d) $\dot{B}_\theta$ magnetic signature of last I-phase pulsation and the first type-I ELM.

$\dot{B}_\theta$ signal (b,e). A similar precursor with the same frequency is visible in the unwrapped phase of the hopping reflectometry signal ϕ_{RFL} (figure 5.3a), where ϕ_{RFL} corresponds, in first approximation, to the history of the movement of the cut-off layer [129, 130]. This is also present in the early I-phase indicating that the radial Mirnov coils might not detect it because the pulsations are substantially smaller compared to the later phase. This suggests that the early I-phase pulses have similar characteristics to the later ones. The presence of a magnetic signature of the I-phase pulsations also helps to distinguish them from other X-point fluctuations which often take place under similar plasma conditions [84, 131, 132].

The late I-phase is often interrupted by type-I ELMs as seen in figure 5.1 ($t = 4.675\,\mathrm{s}$) and in figure 5.4. Approaching the first type-I ELM, the I-phase pulsations can keep a well defined frequency and do not transient in a more intermittent phase which is often associated to type-III ELMs (see spectrogram in figure 5.4b). The $\dot{B}_\theta$ magnetic

signature of the last I-phase pulsation and of the first type-I ELM is shown in figure 5.4d. The type-I ELM seems to be triggered in a similar awy as the last LCO with equivalent features as presented in [133]. The frequency of LCO fluctuations increases after the type-I ELM which, according to the scaling in [77], is an effect of the reduction of the pedestal pressure due to the type-I ELM itself. The existence of type-I ELMs during the I-phase clearly indicates an increase of particle and heat confinement at the edge to a level close to that of the H-mode rather than the L-mode. This is also confirmed by the signature of the H–L transition where the plasma transits back into L-mode only when the LCOs disappear ($t = 5.017\,\mathrm{s}$, figure 5.1). Therefore, for the analysis carried out in this chapter, the strongest confinement change is assumed to take place at the onset of the I-phase (labelled "early I-phase").

5.1.2 Characterization of the L–I–L oscillations

The L–I–L oscillations are repetitive transitions from L-mode to I-phase and back to L-mode and only exhibits in specific plasma conditions ($n_e \geq 4.5 \times 10^{19}\,\mathrm{m}^-3$) and are suited to study the L–I transition. An example of a few oscillations is shown in figure 5.5 where the I-phase time windows are highlighted in grey. These are clearly distinguishable from the L-mode phase using the $\dot{B}_\theta$ signal (see figure 5.5e). If the input power is kept constant, this type of oscillatory phase can be run steadily. Such regular L–I–L transitions with a frequency around 180 Hz are only a feature of the L–H transition in the high density branch of P_{thr} ($n_e \geq 4.5 \times 10^{19}\,\mathrm{m}^-3$) and have so far been reported only in JET and ASDEX Upgrade [84, 134, 135]. Other single L–I–L transitions also have been documented previously but never with such as oscillatory characteristics [66, 70, 124]. Note that the L–I–L transitions presented here are not triggered by sawteeth which under these conditions are found to be relatively small and have a lower frequency compared to the L–I–L transitions.

As discussed in the previous section, every L–I transition exhibits an increase of the confinement reflected in a modulation of the edge line integrated electron density (figure 5.5b). This also leads to a drop of the divertor shunt current which indicates a reduction of transport in the scrape-off layer (figure 5.5a, black). The same effect is seen on the electron temperature $T_{\mathrm{e,div}}$ measured by the Langmuir probes in the divertor (5.5d). The L–I–L oscillations might be confused with the divertor oscillations where the divertor plasma oscillates between the detached and non-detached states (see figure 5.5f-j and [136, 137]). These take place also close to the L–H transition power threshold at medium to high densities and show similar effects on I_{div} (figure 5.5f), $n_{\mathrm{e,edge}}$ (g) and on $T_{\mathrm{e,div}}$ (i). However, the X-point fluctuations, present in the detached phase, do not have any $\dot{B}_\theta$ magnetic signature (figure 5.5j) and are therefore easy to distinguish from the I-phase pulsations. Moreover, the L–I–L oscillations usually take

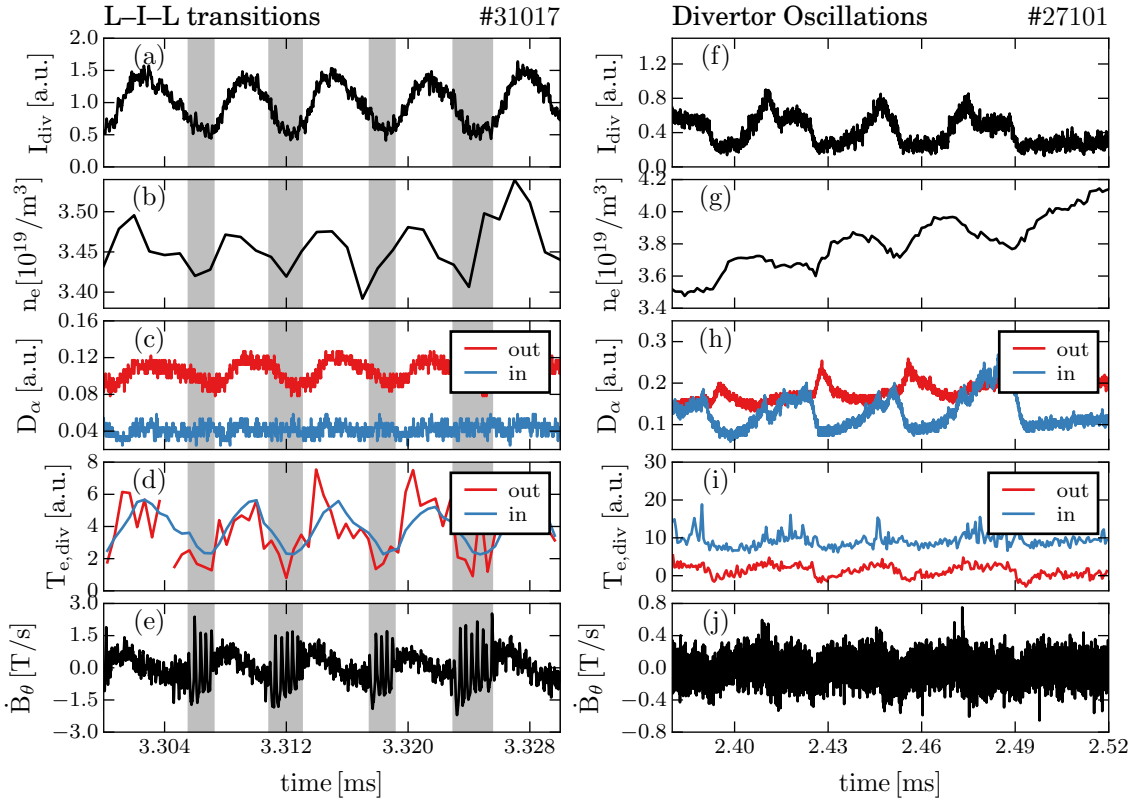

Figure 5.5: Characterization of the L–I–L transitions (a-e) and comparison with the divertor oscillations (f-j): (a,f) divertor shunt current, (b,g) edge electron density, (c,h) D_α emission at the inner (blue) and outer (red) divertor, (d,i) electron temperature at the inner (blue) and outer(red) divertor measured by Langmuir probes and (e,j) poloidal magnetic fluctuations (note the different time windows).

place with a higher frequency.

The L–I–L oscillations are observed only in the high density branch of the L–H transition power threshold ($n_e \gtrsim 4.5 \times 10^{19}\,\mathrm{m}^{-3}$) see figure 2.7). This suggests two possible mechanisms for the onset of these oscillations, one linked with the power threshold and the other with the divertor detachment suggested in [84]. Every L–I transition induces an increase of the electron density (figure 5.5b) and, in turn, of the input power required for the H-mode onset (see scaling (2.26)). By keeping the net input power constant after the L–I transition, the plasma might not have enough power to sustain the I-phase and therefore it transits back to L-mode. The other mechanism involves the effect of the detachment on E_r in the scrape-off layer. The radial electric field in the scrape-off layer in case of a continuous limiter is defined by the parallel can

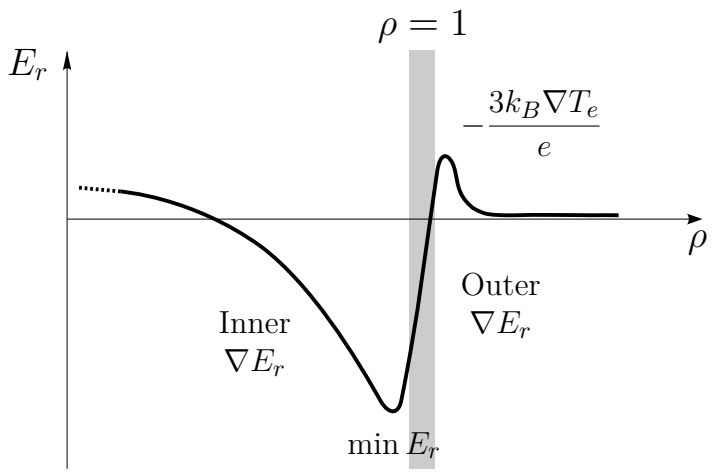

Figure 5.6: Schematic view of the edge E_r profile across the separatrix.

be approximated by [138]:

$$E_r = -\frac{3k_B\nabla T_e}{e}. \tag{5.2}$$

Figure 5.6 shows a schematic view of the edge E_r profile across the separatrix.

In the SOL the reduction of particle and heat fluxes connected to the L–H transition leads to a decrease of the electron temperature (figure 5.5d). This often coincides with the onset of the detachment state of the inner divertor [139, 140]. The reduction of T_e due to the L–I transition leads to a reduction of ∇T_e and therefore, of E_r in the SOL. In this way, the outer ∇E_r and hence the resulting $\mathbf{v}_{\mathrm{E\times B}}$ shear is reduced if the minimum of E_r stays constant. This effect could potentially explain the L–I–L oscillations, however, the E_r profile inside the separatrix evolves as well at the L–I transition. The increase of the confinement connected with the I-phase onset goes along with a steepening of the edge gradients and therefore, of E_r (more details in chapter 6). However, it has to be noticed that the L–H transition and the detachment onset have different dependencies on the main plasma parameters [46, 141] and therefore, the two phenomenas can be disentangled. Moreover, it is not clear whether the inner or the outer gradient of $\mathbf{v}_{\mathrm{E\times B}}$ or both of them are mostly responsible for the turbulence suppression at the L–H transition. In this chapter, the time window just before the final L–I transition is considered for the comparison between different discharges.

5.2 L–H transition power threshold

In this section, the minimum of the radial electric field profile ($E_{r,\mathrm{min}}$) is compared just before the strongest confinement change in discharges with different power threshold.

Here, the E_r minimum is used as proxy of the inner E_r gradient as shown in [120]. However, if the E_r in the scrape-off layer remains constant $E_{r,\min}$ is also a proxy of the outer E_r gradient assuming that the position of the minimum of E_r does not strongly change. In the discharges presented in this section, only one magnetic configuration has been used with a fixed X-point position and constant impurity seeding was apply, therefore the conditions of the E_r in the SOL are expected to stay constant. Hence, $E_{r,\min}$ might be a good approximation of both inner and outer shear layer. In this way, the microscopic $\nabla v_{E\times B}$ turbulence shear can be related directly to the macroscopic L–H transition power threshold.

This work aims at the same time to extend the study performed in [83] and support its results, combined to the results found in [132], by directly measuring the radial electric field without recurring to modelling.

5.2.1 Toroidal magnetic field dependence

The almost linear dependence of the L–H transition power threshold on the toroidal magnetic field B_ϕ (see equation (2.26)) is not very well understood as of yet. On the other side, the dependence of the power threshold on B_ϕ is amongst others the most robust dependence observed in every device independently of plasma conditions [142].

In figure 5.7, the power threshold dependence on B_ϕ is related to the radial electric field shear, here approximated by the minimum of E_r. Figure 5.7a shows the net input power at the L–H transition as a function of the toroidal magnetic field for deuterium (blue) and hydrogen plasmas (red). The dashed black line shows the predicted value of the threshold power from the scaling $P_{\text{thr,scal08}}$ for deuterium (see section 2.4.1). This is systematically higher than the measured power threshold due to the reduction of $P_{\text{net,LH}}$ observed with the tungsten wall [142]. However, a linear dependence of $P_{\text{net,LH}}$ on B_ϕ is observed as expected from the scaling introduced in equation (2.26). The power threshold in hydrogen (red) is roughly a factor of 1.8 higher compared to the one in deuterium (blue) at the same toroidal field. This behaviour was observed in several machines [51, 142–144]. Note that here the net input power is calculated without subtracting the radiation losses from the volume inside the separatrix and the L–H transition presented here takes place at similar electron densities, roughly $4.5 \times 10^{19}\,\text{m}^{-3}$.

In figure 5.7b the absolute value of the E_r minimum just before the final L–I transition is shown as a function of the magnetic field B at the measurement position for deuterium (blue) and for hydrogen (red) discharges. The minimum of E_r scales roughly linearly with B, consistent with the almost linear dependence of P_{thr} on B_ϕ [46]. In other words, a constant $v_{\mathbf{E}\times\mathbf{B}} = E_r/B$ is found at the L–H transition as shown in [47]. These findings may indicate that a critical $\mathbf{v}_{\text{E}\times\text{B}}$ shear is required to access the H-mode.

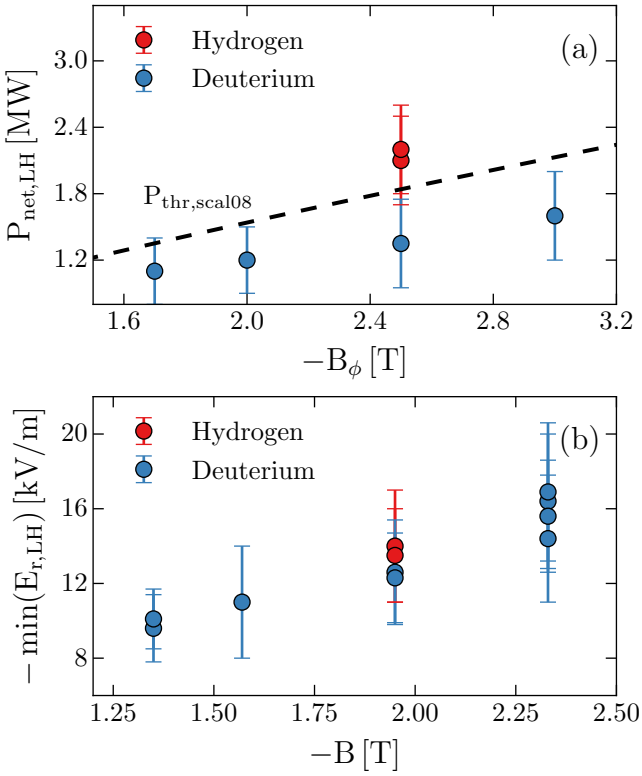

Figure 5.7: Toroidal magnetic field scan in deuterium (blue) and hydrogen (red): (a) net input power at the L–H transition as a function of the toroidal magnetic field. The $P_{\mathrm{thr,scal08}}$ scaling [46] is highlighted by the dashed black line. (b) Minimum of the radial electric field at the L–H transition as a function of the magnetic field at the measurement location.

However, the turbulence characteristics at the edge might also change with the magnetic field. Therefore, the right hand side of the criterion for the turbulence decorrelation (2.13) might also scale with B. Hence the B dependence has to be integrated differently. This is the case, for example, if the edge turbulence follows the gyro-Bohm scaling where the correlation length scales with the ion Larmor radius and therefore inversely with B_ϕ [145].

The same considerations are valid also for the comparison between hydrogen and deuterium plasmas. In hydrogen, the minimum of E_r is in agreement with the measurements in hydrogen within the error bars (figure 5.7b), while a higher input power is required to transit to H-mode in hydrogen plasmas (figure 5.7a). These findings again point to a possible critical $\mathbf{E}\times\mathbf{B}$ velocity shear for the H-mode onset independent of the plasma isotope. However, as for the B_ϕ-scan, the characteristics of the turbulence also need to be compared between hydrogen and deuterium plasmas. For example, in [146]

the turbulence correlation length L_c in L-mode is shown to be comparable in hydrogen and deuterium plasmas at the edge while in the plasma centre the predicted gyro-Bohm scaling is verified. On the other hand, in the DIII-D and TEXTOR tokamaks the edge L_c in hydrogen and deuterium are found to be different [147, 148]. Therefore, it is not clear whether the turbulence characteristics at the plasma edge change with the plasma isotope. Note that the energy confinement time is known to increase with the isotope mass [149].

These observations only tackle one side of the turbulence decorrelation criterion at the L–H transition. Here, for a constant magnetic configuration, a threshold in the $\mathbf{E}\times\mathbf{B}$ shear for the H-mode onset is found. More information about the edge turbulence behaviour at the L–H transition is required to generalize this as a criterion.

5.2.2 Electron density dependence

The dependence of the L–H power threshold on the electron density is not monotonic (see figure 2.7). In case of ASDEX Upgrade, P_{thr} has a minimum at an electron density of roughly $n_{e,\mathrm{min}} = 4 \times 10^{19}\,\mathrm{m}^{-3}$. Although it has been found in almost every tokamak [44, 47–50], this feature is not included in the power threshold scaling. A possible explanation of the increase of P_{thr} at low densities has been suggested in [83] and in [82]. In [83], a threshold for the H-mode onset in the neoclassical electric field has been found independent of the electron density at a fixed toroidal magnetic field. In particular, [83] explored the range of densities below $n_{e,\mathrm{min}}$ where P_{thr} is observed to rise with the decreasing density. In this regime, the electron and ion fluids decouple and the electron cyclotron heating used in these discharges is almost exclusively deposited in the electrons. Only a small fraction is then transferred to the ion by collisions. Hence, to reach the same neoclassical electric field at the L–H transition more heating is required. In other words, one of the key players of the L–H transition physics is the ion heat flux at the plasma edge. These findings have been confirmed by an independent study described in [82]. Here, the ion and electron heat flux at the edge have been determined by means of transport analysis. A correlation between the edge ion heat flux and the H-mode onset has been found in deuterium plasmas and more recently also for hydrogen plasmas [150]. The increase of the ion heat flux and consequently, of the edge pressure gradient, however, also enhances the turbulence level at the edge. Consequently, due to the higher diamagnetic velocity, the probability of triggering zonal flows increases with edge ion heat flux. This mechanism is shown theoretically to reproduce the low density branch of the L–H transition power threshold, while in the high density branch ion-ion collisions are damping the ZFs leading to an increase of P_{thr} with n_e [72, 73].

This section presents an extension of the findings published in [83]. In figure 5.8b,

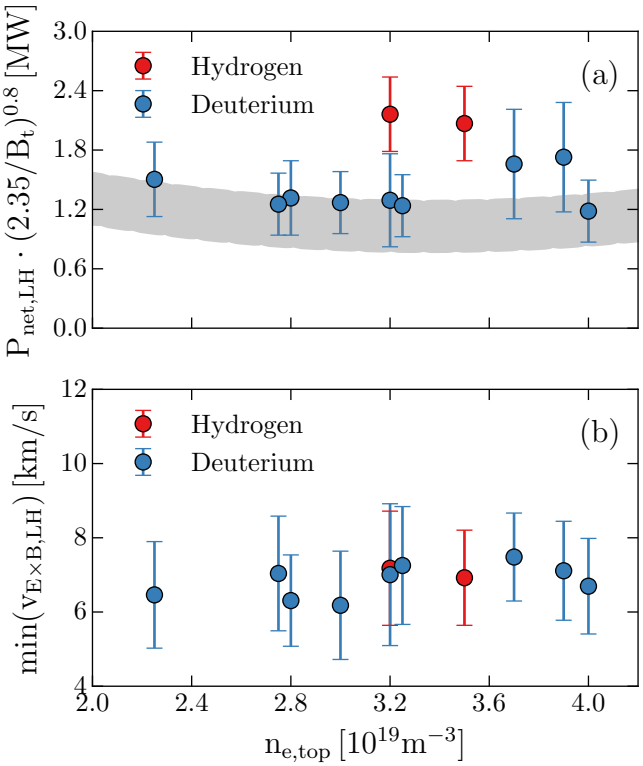

Figure 5.8: Electron density scan in deuterium (blue) and hydrogen (red): (a) net input power at the L–H transition as a function of the electron density, the grey band corresponds to the P_{thr} values taken from reference [142], (b) minimum of the **E**×**B** velocity at the L–H transition as a function of the pedestal top electron density.

the minimum of the **E**×**B** velocity at the L–H transition is shown as a function of the pedestal top electron density for the discharges presented in the previous section. The corresponding calculated power threshold normalized to $B_\phi = 2.35\,\mathrm{T}$ is shown in figure 5.8a in comparison with the estimation from [142] which is highlighted by the grey band. Here, the discharges performed in deuterium plasmas are indicated in blue while the ones in hydrogen are marked in red. The minimum of the **E**×**B** velocity at the L–H transition is found to be constant independent of the electron density, similar to the observations in [83].

5.2.3 Considerations on the L–H transition power threshold

The findings presented in this section correlate the **E**×**B** velocity and the net input power close to the L–H transition exploring the main dependencies of the L–H power threshold, on B_ϕ and n_e. A threshold in $\mathbf{v}_{E\times B}$ for the L–H transition is found consistent

with [83, 85]. Figure 5.9 presents a comparison between the measurements of the minimum of $\mathbf{v}_{\mathrm{E\times B}}$ discussed in the previous section and the evaluations published in [83, 85, 150]. Within the error bars a constant $\mathbf{E}\times\mathbf{B}$ velocity is found over a large range of the electron densities, for different B_ϕ and with carbon and tungsten wall [85] (figure 5.9a). At the L–H transition the $\mathbf{E}\times\mathbf{B}$ velocity is on average $v_{\mathrm{L-H}} = 6.8 \pm 1.0$ km/s. Here measurements from CXRS (this work) and Doppler reflectometry [150] are compared with the predictions from neoclassical theory [83, 85] showing good agreement within the error bars. This suggests that the background condition of the $\mathbf{E}\times\mathbf{B}$ velocity just before the L–H transition is dominated by the neoclassical $\mathbf{E}\times\mathbf{B}$ velocity. This however does not exclude a contribution (order of few km/s) from zonal flows to the total $\mathbf{v}_{\mathrm{E\times B}}$ and/or that ZFs can trigger the L–H transition itself. More details about the fast evolution of E_r are given in the next section. The same evaluations of $\mathbf{v}_{\mathrm{E\times B}}$ are shown in figure 5.9b as a function of the net input power at the L–H transition normalized to $B_\phi = 2.35\,\mathrm{T}$. A large variation of $P_{\mathrm{net,LH}}$ is observed across the whole database due to the scan of the L–H power threshold dependencies while the minimum of $\mathbf{v}_{\mathrm{E\times B}}$ remains roughly constant. In other words, for the same $\nabla v_{\mathrm{E\times B}}$ different ion heat fluxes $Q^{\mathrm{LH}}_{i,\mathrm{edge}}$ and hence $P_{\mathrm{net,LH}}$ are required. Several reasons could produce this effect, for instance a higher ion heat transport (this is the case in hydrogen plasmas [150]) or a change of the plasma boundary conditions or a change of the SOL.

The findings presented here combined with [82, 83, 150, 151] clearly point to a major role of the main ions in the L–H transition physics. Assuming that the edge turbulence characteristics are similar in the different configuration, one might extrapolate that a critical $\mathbf{E}\times\mathbf{B}$ shear is necessary for the H-mode onset.

Finally, a clarification to avoid misunderstanding: this study does not aim to unify all the different experimental observations characterizing the transition from L- to H-mode. Many of them require a deeper knowledge of the influence of the SOL or of the turbulence behaviour to the L–H transition, as for instance the $P_{\mathrm{thr,LH}}$ dependence on the X-point position [53, 84]. Here, only the main dependences of the L–H power threshold using a constant magnetic configuration are investigated.

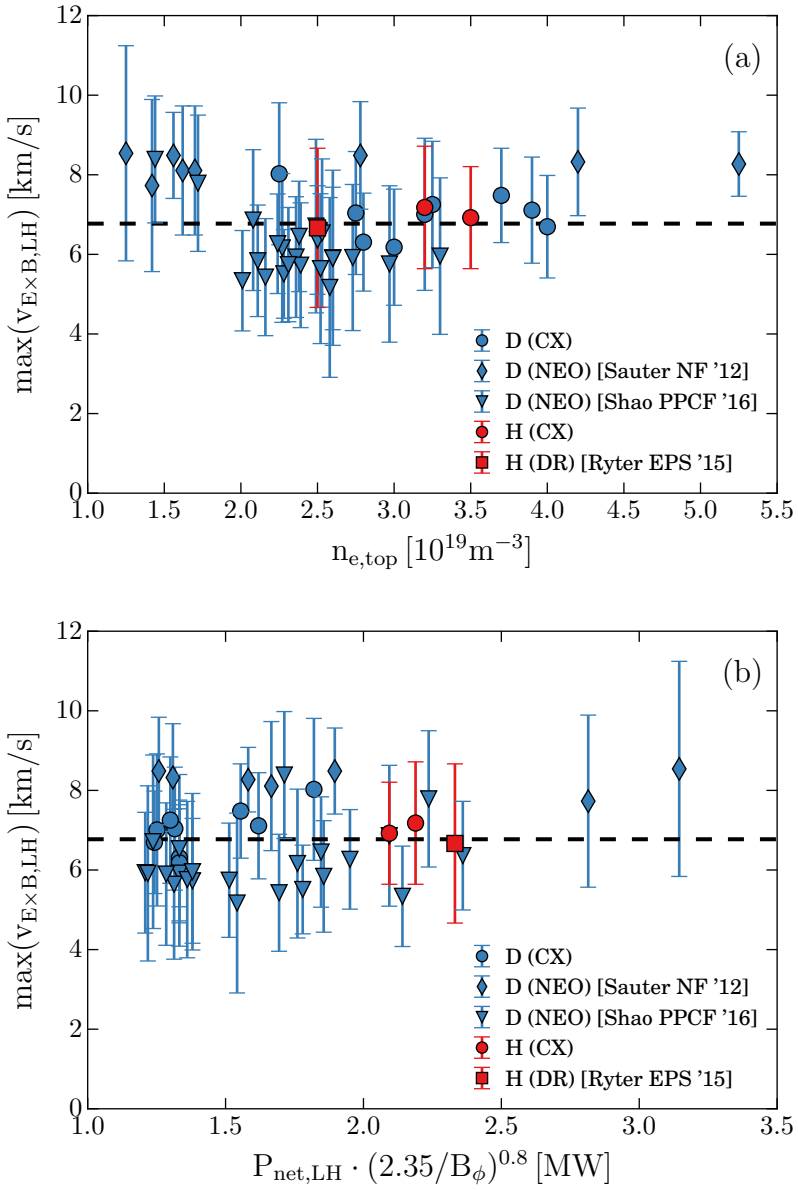

Figure 5.9: Comparison between the measurements of $\mathbf{v}_{\mathrm{E}\times\mathrm{B}}$ at the L–H transition in deuterium (blue) and hydrogen (red) presented in figures 5.7 and 5.8, including data from [83, 85, 150]. The minimum of the $\mathbf{E}\times\mathbf{B}$ velocity at the L–H transition is shown as a function of the pedestal top electron density (a) and the net input power normalized to $B_\phi = 2.35\,\mathrm{T}$ (b). The data points labelled with "CX" are evaluations obtained via the charge exchange recombination diagnostic, while "NEO" and "DR" indicates respectively predictions from neoclassical theory and measurements from Doppler reflectometry.

6 The interplay between turbulence, neoclassical and zonal flows at the L–H transition

The key players of the L–H transition, turbulence, the neoclassical radial electric field and the zonal flows, are investigated in this chapter. Their fast evolution close to the L–H transition is presented and their inter-correlations are studied in detail. The important theoretical concept were introduced in chapter 2 while the following section is dedicated to an experimental view on the most recent investigations.

6.1 Previous results from theory and experiments

In toroidally confined plasmas, the $\mathbf{E}\times\mathbf{B}$ velocity is a sum of at least two contributions: the always present neoclassical or background $\mathbf{E}\times\mathbf{B}$ flows (NFs) and the self induced turbulent flows, also called zonal flows (ZFs). The background flow is dominated by the main ion temperature (T_i) and density (n_i) gradients and is roughly equal to the diamagnetic velocity $\mathbf{v}^\mathrm{i}_\mathrm{dia} = \nabla(n_\mathrm{i}T_\mathrm{i})/(eZ_\mathrm{i}n_\mathrm{i})$ (section 2.3.2). Zonal flows are azimuthally symmetric, bandlike shear flows generated by turbulent stresses [24] (section 2.3.3).

Early DIII-D results [152–155] showed that at the L–H transition the value of E_r decreases and a negative well like structure in E_r, forms on and just within the separatrix. This takes place in conjunction with a drop of the edge density and magnetic fluctuations. The edge $\mathbf{E}\times\mathbf{B}$ velocity was observed to speed up on similar timescales as the edge fluctuations were reduced, while the edge $\mathbf{v}^\mathrm{i}_\mathrm{dia}$ was reported to evolve slowly, on a timescale of $\approx 10\,\mathrm{ms}$. The mismatch in the measurements of the evolution of $\mathbf{v}_{\mathrm{E}\times\mathrm{B}}$ and $\mathbf{v}^\mathrm{i}_\mathrm{dia}$ triggered the search of possible other contributions to the total $\mathbf{v}_{\mathrm{E}\times\mathrm{B}}$ at the L–H transition while, in a fully developed H-mode E_r was found to be close to neoclassical prediction [154].

In [37], it was first proposed that turbulence driven zonal flows are responsible for the turbulence suppression and that the neoclassical electric field develops on the slow transport timescale of the particles [38]. Nowadays, zonal flows are frequently invoked

as a possible mechanism for the transition from L-mode to H-mode often through an intermediate phase, here called I-phase (see also section 5.1.1). The I-phase has been observed in many different devices [9, 64, 66–68, 70, 71, 156] and was originally called dithering H-mode [9] and more recently IM-mode, M-mode or limit cycle oscillations (LCOs) [63, 66, 68, 69]. A heuristic model of the I-phase has been proposed in [37] which uses Lotka-Volterra type of equations [157] to describe the energetic interaction between shear flow and turbulence:

$$\begin{aligned} \partial_t \langle \tilde{n}^2 \rangle &= \gamma \langle \tilde{n}^2 \rangle - \alpha_1 \langle \tilde{n}^2 \rangle \langle \partial_r v_\theta \rangle^2 \\ \partial_t \langle \partial_r v_\theta \rangle^2 &= \alpha_2 \langle \tilde{n}^2 \rangle \langle \partial_r v_\theta \rangle^2 - \mu \langle \partial_r v_\theta \rangle^2 \end{aligned} \tag{6.1}$$

where $\langle \tilde{n}^2 \rangle$ is the turbulence energy, $\langle \partial_r v_\theta \rangle^2$ the shear flow intensity, and γ, α_1, α_2 and μ heuristic parameters. γ represents the turbulence growth rate and μ the flow damping. The shear flow is connected to zonal flows through equation (2.23). Due to the energy transfer from the turbulence to flow, the ZF becomes large thus dumping the turbulence itself. This results in a phase difference of $\pi/4$ between turbulence amplitude and zonal flows characteristic of a predator-prey relation. Within this theory, every limit cycle oscillation is regarded as a single L–H transition. This minimal predator-prey model has been successful in reproducing the experimental evolution of the limit cycle oscillations in the I-phase qualitatively. However, mean field equations also present limit cycle like oscillations as solutions [158], as well as the Stringer spin-up effect [159] or MHD equations [160]. In the traditional predator-prey model of the L–H transition, the neoclassical flow is necessary for providing the shear flow after the final transition into H-mode which is required to suppress the rise of turbulence in the H-mode state. Due to the temporary suppression of the edge turbulence at every LCO, the NF is believed to evolve slowly ($\mathcal{O}(10\,\mathrm{ms})$) during the I-phase and later to effectively shear the turbulence leading to the I–H transition. This might be the physics explanation of the early observation about the E_r evolution across the L–H transition. However, there are experimental results which cannot be explained in detail with this model, e.g. the idea of the dithering H-mode itself has been originally triggered by the observation of drop of the pedestal top electron temperature at every LCO [9, 62]. This suggests that, assuming $T_i \approx T_e$ at the pedestal top, the temperature gradient is changing with the frequency of the LCO and hence the neoclassical flow takes part in the dynamic evolution of the $\mathbf{v}_{\mathrm{E}\times\mathrm{B}}$ during the I-phase.

The basic mechanism of turbulence suppression by zonal flows [66–68] and the existence of the predator-prey dynamics [70, 156, 161] have been demonstrated experimentally, turbulence suppression by flow generation appears strong enough to trigger a transition into the H-mode. However, the existence of zonal flows is often deduced from the phase relation between turbulence amplitude and flows, where a phase difference of

$\pi/4$ is characteristic for predator-prey oscillations. A direct measurement of the energy transfer from turbulence to the ZF via Reynolds stress, which is not possible in fusion plasmas, has been made in low temperature plasmas [16]. Hence the physics of the ZF drive through turbulence stresses has been demonstrated. The question remain, however, how much this contributes to the L–H transition. Note that a significant level of the Reynolds stress Π_r cannot alone be taken as first principle demonstration of zonal flow activity, since any change in $\mathbf{v}_{\mathrm{E}\times\mathrm{B}}$, containing also the background flow, may tilt the turbulence eddy orientation and therefore affect Π_r [74]. In other words, any eddy tilting with a non-zero flux surface average results in a non-zero Reynolds stress, independent of the mechanism which triggered the process. Thus, the turbulence eddy tilting due to shear flows is itself automatically inducing some zonal flow. Therefore zonal flows are intrinsically produced at the L–H transition where the turbulence at the edge is strongly sheared. The important point is how much the ZF contribute to the total $\mathbf{E}\times\mathbf{B}$ flow in comparison to the diamagnetic flow. There is both experimental and theoretical evidence that the $\mathbf{E}\times\mathbf{B}$ velocity is dominated either by the turbulence induced flow [66–68, 70, 72, 73, 161, 162] or by the neoclassical flow [70, 71, 81, 163, 164].

There is still considerable discussion about whether the $\mathbf{E}\times\mathbf{B}$ shear really changes prior to spontaneous L to H transitions, i.e. not triggered by sawteeth, and if this is the case on which timescales this happens. A rather small increase of the E_r gradient was indeed before L–H transition observed evolving on typical transport timescales, i.e. $\mathcal{O}(10\,\mathrm{ms})$ [61]. More recent investigations show a relation between the edge ion heat flux Q_i^{edge} and E_r in L-mode [150]. The edge ion temperature gradient is found to weakly increase with Q_i^{edge} as well as E_r just prior to the L–H transition and the comparison with neoclassical theory shows a good agreement in the prediction of the minimum of E_r whereas its gradient shows larger discrepancies.

6.2 I-phase: comparison between neoclassical and measured $\mathbf{E}\times\mathbf{B}$ flows

This section is dedicated to a study of the evolution of the edge profiles in comparison with the measurements of the $\mathbf{E}\times\mathbf{B}$ velocity and of the turbulence level during an I-phase. In particular, $\mathbf{v}_{\mathrm{dia}}^{\mathrm{i}}$ and $\mathbf{v}_{\mathrm{E}\times\mathrm{B}}$ are compared during the I-phase at the L–H and H–L transitions.

A combination of 4 toroidal and 5 poloidal channels has been selected covering the radial range of 2.5 cm of the very edge of the confined area in order to diagnose both the $\mathbf{E}\times\mathbf{B}$ velocity and the ion temperature exactly where the edge transport barrier is

established during the L–H transition. Combining these measurements with the electron density n_e from lithium beam emission spectroscopy (Li-BES) [87, 93], it is possible to compare the evolution of $\mathbf{v}_{\mathrm{E\times B}}$ and $\mathbf{v}^{\mathrm{i}}_{\mathrm{dia}}$ which should be clearly different if ZFs make an important contribution. For this analysis, the dilution of the ions by impurities is assumed to be a flat profile, i.e. $\nabla n_{\mathrm{e}}/n_{\mathrm{e}} \approx \nabla n_{\mathrm{i}}/n_{\mathrm{i}}$, which is a good approximation given the typical profiles in L-mode and the purity of the plasmas.

The analysis presented here requires the application of conditional averaging methods on the CXRS spectra as described in section 4.6. In order to increase the signal to noise ratio, external helium seeding is indispensable. The He^{1+} passive emission gives a relatively strong contribution of up to 40 % of the total signal at the separatrix. Since the passive signal of He^{1+} evolves on similar timescales as the active signal, a direct subtraction of the passive component via beam modulation is necessary to extract localized information. Therefore, only stable I-phases with a constant frequency could be considered, which poses a limit to this study. The late I-phase pulsations are sometimes proceeded by magnetic precursors and often linked to a lower zonal flow activity [70, 121]. However, in section 5.1.1 it is shown that the precursor is not a good figure of merit for the zonal flow activity since it is also detected close to the L–I transition suggesting that the physics of the I-phase pulses seem to be similar, independent of the time to the L–I transition. The mechanism which regulates the LCO frequency is also independent of the temporal distance to the L–H transition [77]. However, this does not exclude a priori that the zonal flows are more influent close to or at the L–I transition. This possibility is analysed in detailed in section 6.3.

6.2.1 L–H transition

The investigation carried out in this section are based on the type of discharge presented in chapter 5. In particular, the evolution of $\mathbf{v}_{\mathrm{E\times B}}$, the profile gradients and the turbulence level at the edge of the plasma are compared during the I-phase at the L–H transition. In figure 6.1) the evolutions of (a) the input power, (b) the integrated electron density at the plasma edge, (c) divertor shunt current, (d) radiation measured by a bolometer channel pointing at the X-point and (e) poloidal magnetic fluctuations are compared. The time windows used for the conditional synchronization of the purely passive signal and of the sum of active and passive radiation are highlighted in blue and red respectively. In total 15 LCOs have been averaged. The synchronization of the CX spectra is based on the measurements of the poloidal magnetic fluctuations $\dot{B}$. The resulting profiles are shown in figure 6.2 together with the measurements of the electron density from the Li-BES diagnostic. Here, the evolution of the electron density (a), the He^{2+} density (b), the ion temperature (c), the toroidal (d) and the poloidal (e) velocities relatively to the onset of the magnetic pulsation (f) are compared at three

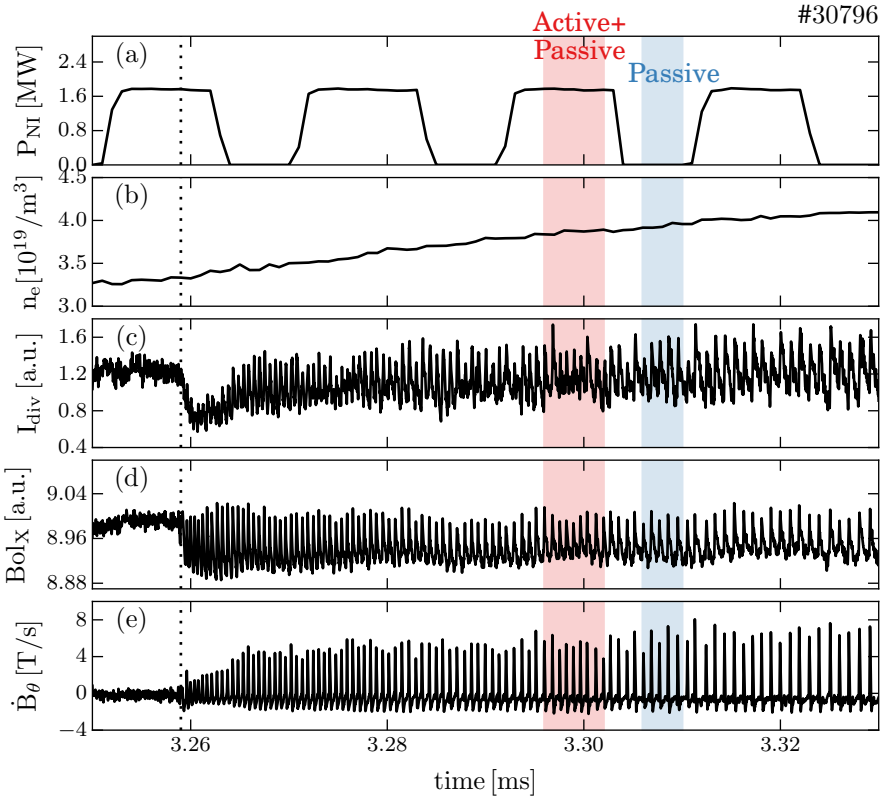

Figure 6.1: I-phase at the L–H transition: (a) NBI input power, (b) integrated electron density at the plasma edge, (c) divertor shunt current, (d) radiation measured by a bolometer pointing at the X-point, (e) poloidal magnetic fluctuations. The time windows used for the conditional synchronization of purely passive and active plus passive signal are highlighted in blue and red respectively.

different radial positions corresponding to the location of the poloidal lines of sights. The time-traces here are binned to the integration time of the fast CX measurements, i.e. 120 µs. Note that the toroidal measurements are fitted and the data interpolated on the measurements position of the poloidal lines of sights. The profile evolution is compared with the measurements of the turbulence level at the edge measured by Doppler reflectometry.

The I-phase pulsations affect all the edge profiles. The gradients of n_e, T_i and $n_{He^{2+}}$ show a small collapse, while the poloidal and toroidal velocity shears are reduced. At the same time, the edge turbulence level A_D increases together with the pulse in the magnetic fluctuation signal. The time resolution of the measurements do not allow to investigate the evolution of the profile during the pulses itself in detail. However, in the time window before the pulse onset (from approximately −0.4 to −0.10 µs), the

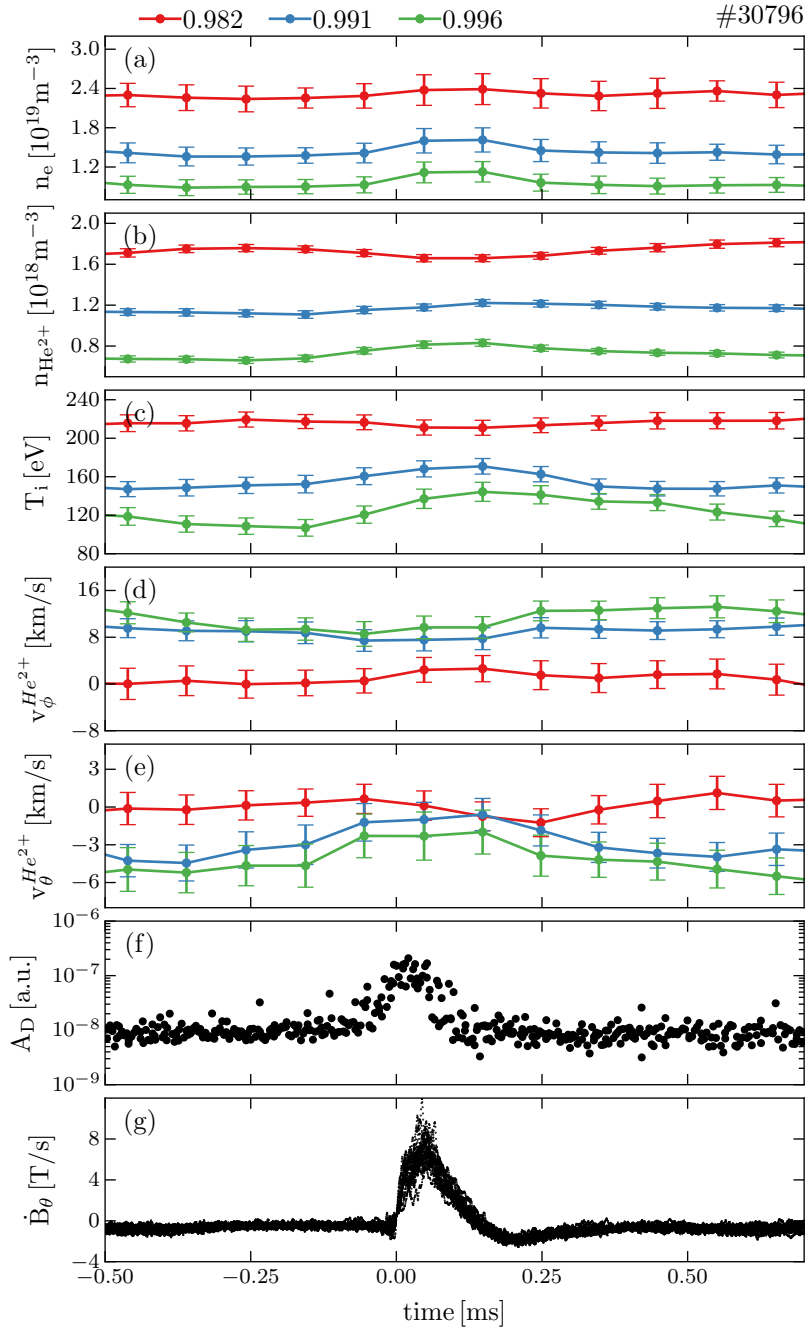

Figure 6.2: Edge profile evolution from conditional averaging during limit cycle oscillations: (a) electron density, (b) He^{2+} density, (c) ion temperature, (d) toroidal velocity, (e) poloidal velocity. The profile evolution is compared to the turbulence measurements at the plasma edge from Doppler reflectometry (f). The profiles are shown at four different radial positions (reported in ρ_p above) at the location of the poloidal lines of sight. The measurements are relatively synchronized to the magnetic pulsations observed in the C09-23 Mirnov coil (g) and binned to the original integration time of the CX measurements, i.e. 100 µs.

profiles are observed to stay constant, therefore the difference between the neoclassical and **E**×**B** flows are, in these time windows, can be investigated in detail. Note that this is the phase where the n_e, T_i, $n_{\mathrm{He}^{2+}}$ profiles appear to be steeper and v_θ to be, in absolute values, stronger. Hence, the strongest $\mathbf{v}_{\mathrm{E}\times\mathrm{B}}$ is measured in this phase, where also the strongest influence of ZFs would be expected.

Within the time resolution of these measurements, no time delay is observed between the evolution of the edge temperature and densities compared to the poloidal and toroidal flows. Such a discrepancy would be indicative of the activity of zonal flows. If there is an external contribution to $\mathbf{v}_{\mathrm{E}\times\mathrm{B}}$ not caused by the diamagnetic velocity, this needs to be compensated by the main ion poloidal or toroidal flow (see equation (2.20)). In other words, if the poloidal or toroidal flows of the impurity (as measured here) change due to a change of $\mathbf{v}_{\mathrm{E}\times\mathrm{B}}$, while n_e and T_i remain constant, this means that the zonal flows have actively contributed to the total $\mathbf{v}_{\mathrm{E}\times\mathrm{B}}$. Within the error bars, the measurements presented here, do not reveal this effect. It may be noted that zonal flows could play an important role on timescales clearly faster than the temporal resolution of the measurements, i.e. $< 100\,\mu\mathrm{s}$.

The effect of the I-phase pulsations is visible only in a narrow region, roughly 1–1.5 cm wide, close to the separatrix. Note that the reduction of the gradient is not only a result of the increase of the helium density and temperature close to separatrix (see green and blue time traces in figure 6.2b–c) but it is also due to a small reduction of the same parameters further inside (≈ 0.7 cm, see red time trace in figure 6.2a–c). This excludes that the observed changes on the profiles are a result of a shift of the whole plasma rather than a real change of them. This could have been a possibility since the CX diagnostics measures at a fixed position in real space (see chapter 4).

Figure 6.3 shows the direct comparison between the measured **E**×**B** velocity (a) and the diamagnetic velocity of the main ions (b). The time traces correspond to three different radial positions close to the separatrix indicated by the different colors. The evolution of the velocities is compared to the measurements of the turbulence level at the plasma edge ($\approx 0.99\,\rho_{\mathrm{pol}}$) obtained by Doppler reflectometry. A quantitative agreement within the error bars is found between $\mathbf{v}^{\mathrm{i}}_{\mathrm{dia}}$ and $\mathbf{v}_{\mathrm{E}\times\mathrm{B}}$ suggesting that, in this phase and for the time resolution of the presented analysis, the contribution from zonal flows to the total **E**×**B** velocity is rather small compared to $\mathbf{v}^{\mathrm{i}}_{\mathrm{dia}}$, in agreement with [71]. The turbulence burst itself seems to have a slightly bigger impact on the measured $\mathbf{v}_{\mathrm{E}\times\mathrm{B}}$ profile compared to $\mathbf{v}^{\mathrm{i}}_{\mathrm{dia}}$ but the difference is not significant. The diamagnetic and the **E**×**B** velocities are better compared in the Lissajous-diagram in figure 6.3d which shows the relation between $\mathbf{v}_{\mathrm{E}\times\mathrm{B}}$ and $\mathbf{v}^{\mathrm{i}}_{\mathrm{dia}}$ for the whole time window shown in figure 6.3a-c. The relation between $\mathbf{v}_{\mathrm{E}\times\mathrm{B}}$ and the turbulence level at the plasma edge suggests a limit-cycle like behavior (figure 6.3e), consistent with [68, 75, 123, 156]. This is however poorly diagnosed due to the large error bars of $v_{E\times B}$ and the limited

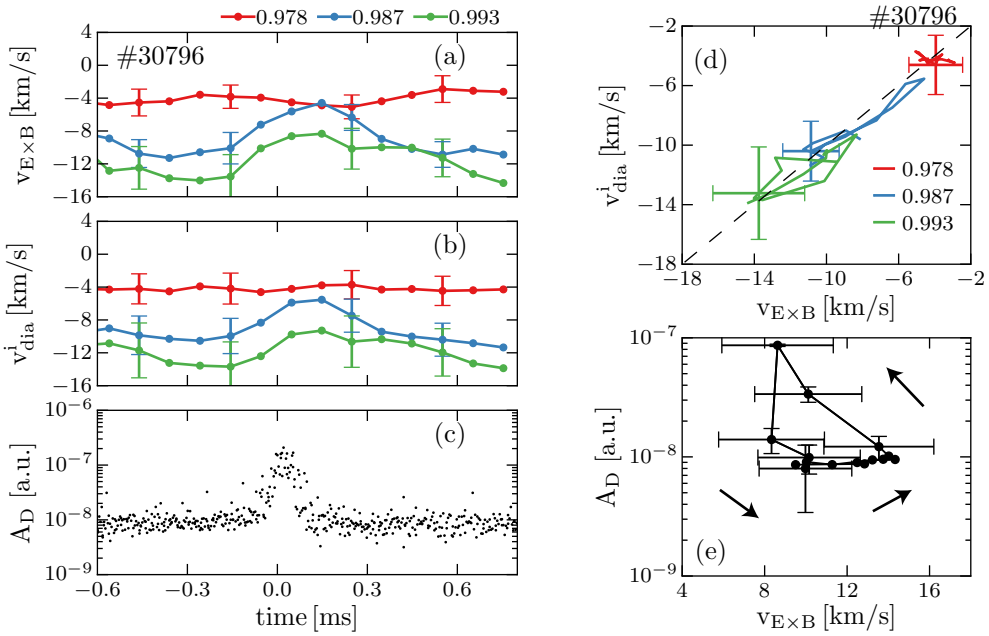

Figure 6.3: Time evolution during an I-phase pulsation at the L–H transition of: (a) **E**×**B** velocity profile, (b) main ion diamagnetic velocity profile and (c) turbulence at the plasma edge measured by Doppler reflectometry at roughly $\rho_{pol} = 0.99$. Lissajous-diagram of: (d) the main ion diamagnetic velocity plotted versus the **E**×**B** velocity, (e) the turbulence level at the plasma edge plotted as a function of the **E**×**B** shear. The time evolution in subfigure (e) is counter-clockwise and is indicated by the arrows. The velocities are shown at three different radial positions indicated by the different colors and correspond to the ρ_{pol} coordinate.

time resolution. Hence, the relation between A_D and $\mathbf{v}_{E\times B}$ cannot be studied in detail. However, the direction of the time evolution, indicated by the arrows in figure 6.3e, is clearly defined since the turbulence pulse (figure 6.3c) is much shorter in time compared to the recovery of the $\mathbf{v}_{E\times B}$. This results in a circle in the Lissajous diagram in figure 6.3d where the time evolution is consistent with the type-J LCO defined in [70]. More details are given later in this chapter. The findings presented here differ from the previous results at ASDEX Upgrade [66]. In particular, the basic trend between the turbulence level and the $\mathbf{v}_{E\times B}$ velocity could not be confirmed. In [66], the limit cycle oscillations are interpreted as a turbulence and zonal flows interaction where the **E**×**B** velocity shear is found to be maximum ("I high") when the turbulence level is also at its maximum, while E_r is found to be almost zero or slightly positive ("I low") when the edge turbulence level is reduced. The measurements presented here show the opposite trend: the **E**×**B** velocity shear is stronger when the turbulence is at its minimum (see figures 6.3a,c), while a reduction of the shear is observed when the turbulence level grows. While the final interpretation might be different, this basic trend is consist with

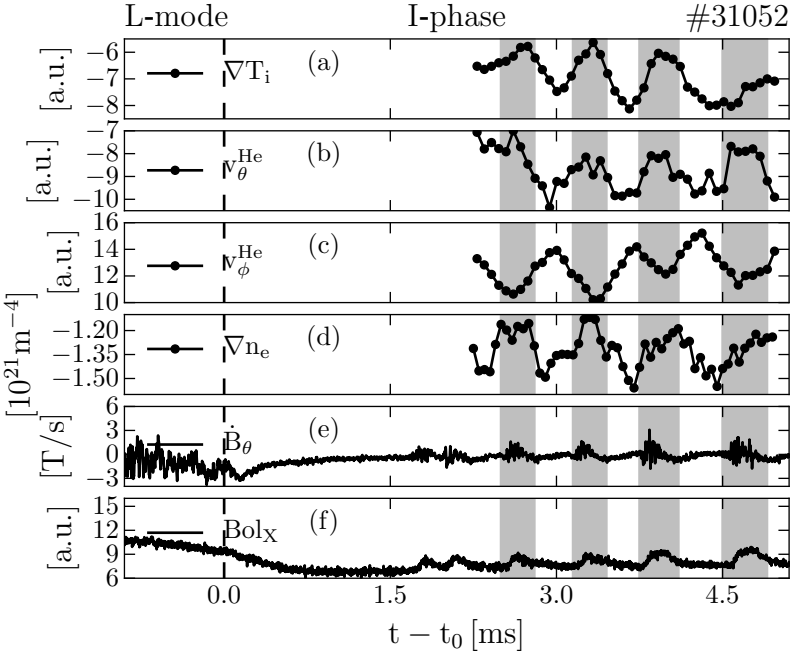

Figure 6.4: Initial I-phase pulsations: (a) T_i, (b) v_θ^{He}, (c) v_ϕ^{He}, (d) n_e, (e) $\dot{B}_\theta$, (f) X-point bolometer channel. T_i, v_θ^{He}, v_ϕ^{He} are reported as in arbitrary units since they are the result of the fit of the active and passive radiation together. The time traces do not cover the entire L–I transition due to the intrinsic bursting acquisition of both fast CXRS and Li-BES diagnostics.

[68, 70, 71, 76, 156]. Several possible reasons could lead to the discrepancy between these measurements and the previous results published in [66], among which: (i) The range of electron density in which the experiments have been performed in [66] was in the range of 2-3 $\times 10^{19}\,\mathrm{m}^{-3}$ and in this work varied in between 4 and 5 $\times 10^{19}\,\mathrm{m}^{-3}$, (ii) the presence of Geodesic Acoustic Modes (GAMs) in [66] whereas no clear sign of GAMs was found in the discharges presented here most likely due to the higher density [165], (iii) the possible loss of signal during the low turbulence level phase of the Doppler reflectometry employed in [66]. Note that the frequency scaling in [77] collects all the I-phases from this work and from [66] and all the different regimes could be fit with the same regression parameters suggesting that the physics governing the I-phase might be the same. More investigations are needed to reveal the reasons of this discrepancy.

Analysis of the initial I-phase pulsations

The analysis presented in this section so far was focussed on a time window relatively far from the onset the I-phase, i.e. roughly 40 ms. Although macroscopically the LCO

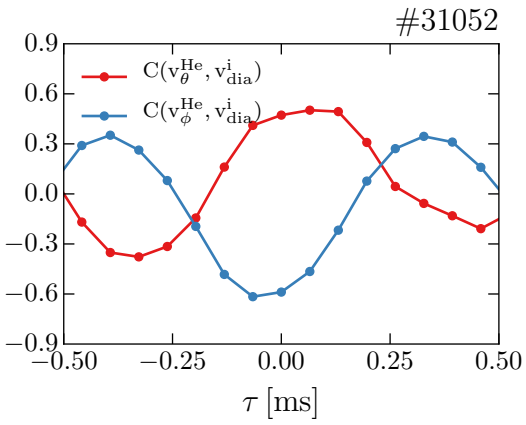

Figure 6.5: Cross-correlation analysis during the initial I-phase pulsations of ≈ 2 ms (see figure 6.4) between the poloidal (red) and the toroidal (blue) helium velocity with $\mathbf{v}^{\mathrm{i}}_{\mathrm{dia}}$, here approximated as $v^i_{\mathrm{dia}} = \nabla(n_e T_i)/n_e$.

pulsations do not change during the evolution of the I-phase, i.e. the magnetic signature and the mechanism which regulates the frequency remains the same (see section 5.1.1), the findings presented here might not apply to the pulsations close to the L–I transition. In [70], probe measurements in the HL-2A tokamak reported two different types of LCO: (i) type-Y LCO, where the turbulence–flow interaction is dominated by ZF and (ii) type-J LCO, in which the turbulence intensity lags behind the $\mathbf{E}\times\mathbf{B}$ velocity contradicting the causality of the turbulence-driven flow mechanism. The $\mathbf{E}\times\mathbf{B}$ flow oscillations in the type-J I-phase are supposed to be maintained by perturbations in the pressure gradient as concluded in the previous section which would also induce the magnetic fluctuations. Note that zonal flows are mostly electro-static fluctuations with very low magnetic components and therefore are unlikely to be the origin of such magnetic fluctuations [166]. The type-J LCO is found to chronologically follow the type-Y LCO in the dynamics when transiting from L- to H-mode, supporting the idea that ZFs are active only in the first part of the I-phase. The I-phase window analysed in this section represents the characteristics of the type-J LCO since the Lissajous-diagram in figure 6.3 shows a time evolution in the anticlockwise direction. This is consistent with the observation that this time window of the I-phase is mostly dominated by the pressure gradient dynamics. However, in DIII-D, the time sequences during the I-phase were found to be consistent with the type-J rather than with the type-Y LCO dynamics although zonal flows are reported to be the main actuators [75, 121, 167]. Therefore, it is difficult to assess whether the criteria proposed in [70] can really help in discriminating between zonal flow or pressure gradient dominated LCOs.

In the discharges presented in this work, the initial bursts of the I-phase are difficult

to diagnose with the fast CXRS diagnostic due to their high frequency, which is rapidly changing and therefore not allowing conditional synchronization analysis (see figures 5.1 and 5.4). Moreover, they are often smaller in amplitude (see figure 6.1) and therefore more difficult to detect. Still, one can fit the passive and active CX radiation together and obtain an estimation of the profile evolution. This is highly sensitive to any change of the profiles at the plasma edge since it does not rely on the synchronization procedure which intrinsically averages over small events. The results of the fit are not accurate in terms of the absolute value, although close to it. Therefore, here and in the following section they are reported in arbitrary units. Note that this approach is particularly sensitive to changes in the poloidal velocity since, for a certain E_r, the He^{1+} ions rotate faster in the poloidal direction compared to the He^{2+} ions because of their smaller diamagnetic term. Thus, the CX measurements of the T_i, v_θ and v_ϕ together with the n_e evaluation from the IDA algorithm can be used to detect possible time delays between the evolution of the edge profile gradients and the flows which, as discussed previously, would directly point to an influence of zonal flows on the edge **E**×**B** velocity. Note that this method cannot exclude the possibility of the presence of zonal flows if these are phase locked to the neoclassical flows, i.e. they have the same temporal evolution. Figure 6.4 shows the evolution of the edge profile gradients and the measured poloidal and toroidal rotation during the initial bursts just after the L–I transition denoted by the vertical dashed line. The edge ion temperature gradient (figure 6.4a) is compared to the helium poloidal (b) and toroidal (c) velocity and to the electron density gradient (d). The I-phase pulsations, visible in the $\dot{B}_\theta$ and in the bolometer signals (figure 6.4e-f), affect close to the beginning not only the flows but also the edge n_e and T_i profile gradients (see highlighted area). This observation was already mentioned in the very first publication on the dithering H-mode [9, 62] where the electron temperature was observed to fluctuate together with the D_α signal and this triggered the idea of the dithering H-mode. This effect, while neglected in the early predator-prey models [37], has recently been included in the so-called 2-predator (zonal and diamagnetic flows) prey models [72].

The cross-correlations between the helium poloidal and toroidal velocity with the main ion diamagnetic velocity, here approximated as $v^i_{\mathrm{dia}} = \nabla(n_e T_i)/n_e$, are shown in figure 6.5 in red and blue, respectively. Within the error bars and the time resolution, the cross-correlation is peaked at zero indicating that the edge flows and the gradients show similar evolution confirming the impression from figure 6.4. Note that the correlation $C(v^{He}_\phi, v^i_{\mathrm{dia}})$ peaks at negative values at $\tau = 0$ since v^{He}_ϕ and $\mathbf{v}^{\mathrm{i}}_{\mathrm{dia}}$ are both reduced in absolute value at the I-phase pulsations, but $\mathbf{v}^{\mathrm{i}}_{\mathrm{dia}}$ is negative (see figure 6.5). The time-resolution of the measurements used in this analysis is 67 µs which combined with the uncertainties of the fits and of the calculation of the gradients cannot exclude time

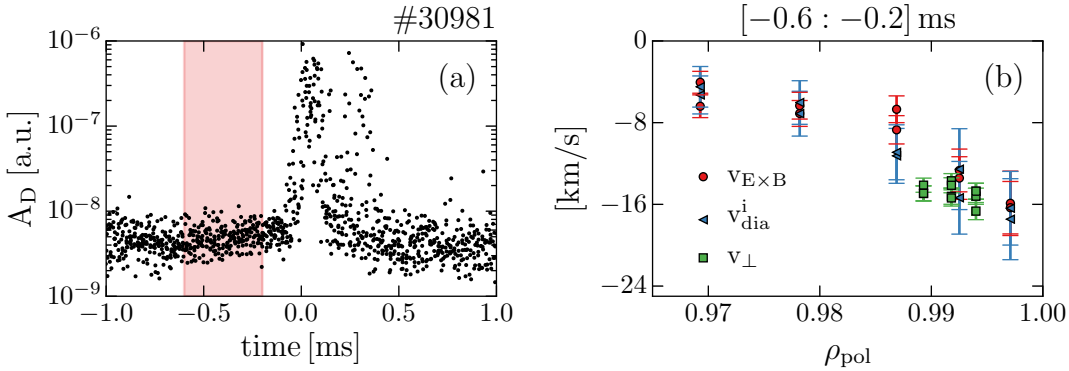

Figure 6.6: Comparison of the fast CXRS and the Doppler reflectometry measurements of the **E**×**B** velocity during the I-phase: (a) synchronized to the magnetic signal C09-23 turbulence level at the plasma edge, (b) comparison between the CX measurements of $\mathbf{v}_{E\times B}$ (red), the Doppler reflectometry measurements of $v_\perp$ (green) and the calculation of the main ion diamagnetic velocity (blue). The comparison is carried out in the time window from −0.6 to −0.2 ms relative to the LCO onset. This is highlighted in red in figure (a). The CXRS time resolution is in this case 300 µs, while for the Doppler reflectometry a window of 100–200 µs has been averaged to obtained good signal to noise ratio.

delays of the order of 100-200 µs, i.e. roughly 15–20% of the LCO duty cycle.

Comparison with Doppler reflectometry

No evaluation of the **E**×**B** velocity could be obtained from Doppler reflectometry during the I-phase in this discharge due to the reduced turbulence level between the LCO bursts, resulting in a low signal to noise ratio. At the burst itself, due to the rapid change of the electron density gradient and therefore of the microwave scattering layer, a reliable localization of the Doppler reflectometry measurements is not possible. In some cases, a Doppler peak could be identified for a few hundreds of µs just before the onset of the turbulence burst allowing the estimation of the **E**×**B** velocity. This usually appears only in the late I-phase, when the frequency is reduced and the pulsations are stronger. The cross-check between the fast CXRS measurements and the Doppler reflectometry system is of fundamental importance. This comparison was possible at the point where the $\mathbf{v}_{E\times B}$ shear reaches its maximum and hence, where a strongest contribution of a ZF might be expected. Figure 6.6b shows the comparison between the measured $\mathbf{v}_{E\times B}$ profile from the fast CXRS diagnostic (red), the Doppler reflectometry measurements of $v_\perp$ (green) and the predicted main ion diamagnetic velocity $\mathbf{v}^i_{dia}$ (blue) in the time window from −0.6 to −0.2 ms relative to the LCO onset. The time window is highlighted in red in figure 6.6a where the synchronized turbulence level is shown. The radial coverage of Doppler reflectometry measurements is limited by the range of

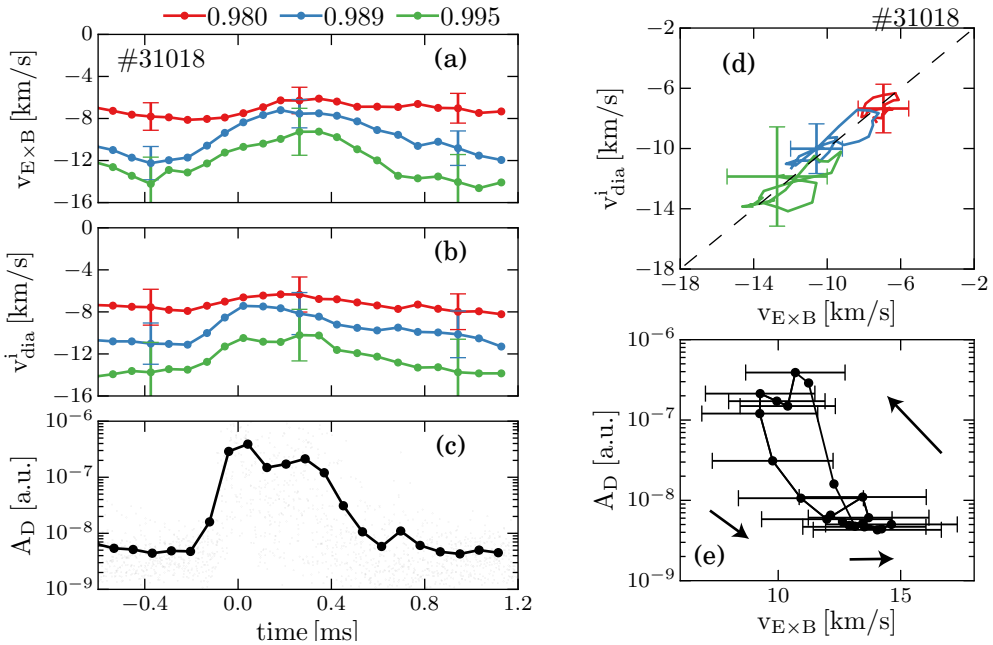

Figure 6.7: Time evolution during an I-phase pulsation at the H–L transition of: (a) **E**×**B** velocity profile, (b) the main ion diamagnetic velocity profiles and (c) the turbulence at the plasma edge measured by Doppler reflectometry. Lissajous-diagram of: (d) the main ion diamagnetic velocity as a function of the **E**×**B** velocity, (e) the turbulence level at the plasma edge as a function of the **E**×**B** shear. The velocity profiles are shown at three different radial position indicated by the different colors and reported in ρ_{pol}.

frequency scanned during the analysed phase. A good agreement between $\mathbf{v}_{E\times B}$, $\mathbf{v}^i_{dia}$ and $v_\perp$ profiles is found within the error bars. However, the comparison is very limited in the spatial and in the temporal extension, since it was only possible for this small time window and for a limited region. More extensive comparison are foreseen due to the installation of an additional reflectometry channel which allows to probe the plasma using two different frequencies and hence, two distinct radial positions, at the same time.

6.2.2 H–L transition

The same type of analysis performed for the I-phase at the L–I–H transition (see section 6.2.1) is presented here for the I-phase at the H–I–L transition. The results are consistent with the analysis of the I-phase close to the L–H transition. Figure 6.7 shows the comparison between the measured profiles of $\mathbf{v}_{E\times B}$ (a) and $\mathbf{v}^i_{dia}$ (b). The profiles are reported at three different radial positions (in ρ_{pol}) indicated by the different colors. At the rise of the turbulence burst (figure 6.7c), both the diamagnetic and the **E**×**B**

velocity are found to be reduced, consistent with the analysis in section 6.2.1. Within the error bars, a quantitative agreement is found between the measurements of the $\mathbf{E}\times\mathbf{B}$ velocity and main ion diamagnetic velocity suggesting that the contribution of the ZFs to the $\mathbf{E}\times\mathbf{B}$ velocity is small. Their maximal magnitude is of the order of a few km/s. The comparison is better presented in the Lissajous diagram in figure 6.7d, where $\mathbf{v}^{\mathrm{i}}_{\mathrm{dia}}$ is shown as a function of $\mathbf{v}_{\mathrm{E}\times\mathrm{B}}$ for the entire LCO duty cycle. The Lissajous diagram between the edge turbulence level A_D and the $\mathbf{v}_{\mathrm{E}\times\mathrm{B}}$ velocity shows again a limit-cycle like behavior where the time evolution is described by a counterclockwise rotation indicating a type-J LCO [70].

6.3 The relation between flows and gradients during the L–I–L oscillations

The findings presented in the previous section are challenging some aspects of the predator-prey model, the widest accepted model for the L–H transition. The LCOs during the I-phase could be analysed in detail in a conditional synchronization approach and the measurements of $\mathbf{v}_{\mathrm{E}\times\mathrm{B}}$ are in good agreement with the main ion diamagnetic velocity on the timescales of 200 µs (see figures 6.3 and 6.7) suggesting that, in the investigated time windows, the ZFs might only be important on much shorter timescales, consistent with [71]. This analysis was only possible relatively far from the L–I (I–L) transition and therefore might not apply to the initial (final) I-phase. This phase could only be investigated in terms of the temporal evolution of the edge gradients and the flows. The main ion diamagnetic velocity is found to evolve with the poloidal and toroidal velocity (see figure 6.4) within a time scale of 150 µs indicating that zonal flows are phase locked into the neoclassical flows within this time scale. This contradicts the early predator-prey models where a phase shift of $\pi/2$ between the evolution of the flows and the gradients has been predicted [38]. More recent models do not necessary predict this time delay [72, 168].

Following the argument that zonal flows might be more significant close to the L–I transition, one would expect that at the L–I transition itself their effect is the strongest. The L–I transition is often considered simply as a limit cycle oscillation within only one cycle [9, 72]. This interpretation comes from the initial definition of the dithering H-mode where every dithering was identified as a single L–H–L transition. Under certain circumstances, the evolution from L-mode to H-mode might not develop any I-phase where consequently the only LCO is the L–H transition itself [161, 169–171]. These are called single-step transitions and were successfully incorporated into the predator-prey model. The energy transfer between the turbulence and the flows through the turbulence stresses normalized to the turbulence growth rate [171] has been proved

experimentally to be a good figure of merit for the onset of the L–H transitions [161, 169, 171, 172]. This emerges as a natural criterion for the turbulence suppression and hence, for the H-mode onset and is often related to the presence of zonal flows since the edge pressure gradient is observed to steepen up on different timescales compared to the $\mathbf{v}_{\mathrm{E}\times\mathrm{B}}$ flows. However, as discussed in [172], if the time scale separation between the evolution of the pressure gradient and the flows would be reduced, the gradients themselves could contribute to the turbulence stress. In this section, this time separation is investigated.

Every L–I–L transition shows slightly different features, for instance the number of bursts during the short I-phase or the evolution just before the onset of the I-phase where sometimes small amplitude limit cycle oscillations appear (see figures 5.5 and 5.1). Hence, it is not possible to use any conditional synchronization algorithm and no quantitative evaluation of T_i, v_θ^{He}, v_ϕ^{He} and n_{He} can be obtained from the CX spectra. However, as described in the previous section, the relative evolution between the profile can be investigated and a test for detecting delays between the edge profile gradients and the flows can be applied. Figure 6.8 presents the time evolution of the edge profiles during the L–I–L dithers of the (a) ion temperature, (b) electron density, (c) helium poloidal velocity and (d) time trace of $\dot{B}_\theta$ measured by the poloidal Mirnov coil C09-23. The three colours indicate the different radial positions in ρ_{pol} of the measurements. The grey shaded area in figure 6.8b denotes the time interval when the Li-BES is switched off for measuring the background radiation. No evaluation of the $\mathbf{E}\times\mathbf{B}$ velocity could be obtained from Doppler reflectometry during the I-phase due to the reduced turbulence level between the LCO bursts, resulting in a low signal to noise ratio. A strong modulation of the gradients in T_i and n_e is observed, coherent with the increase of confinement associated to the LCOs. In particular, the steepening of the edge gradients is established by a reduction of density and temperature close to the separatrix and initially extends $1.0-1.5\,\mathrm{cm}$ just inside the separatrix. These substantial changes in the edge v_θ^{He} and T_i profiles are not due to movements of the plasma because its position only oscillates by $1.0-1.5\,\mathrm{mm}$ ($\approx 20\,\%$ of the spatial resolution) in between L-mode and the I-phase. The zoom in of one L–I–L transition presented in figures 6.8e-h shows that during the I-phase, every turbulence burst is accompanied by a reduction of the edge flows and gradients (see dashed lines) implying that the background flow changes in phase with the total $\mathbf{v}_{\mathrm{E}\times\mathrm{B}}$ and the turbulence itself. This is consistent with the results discussed in the previous section (see figure 6.4).

Since the active and the passive emission have to be fitted together, a quantitative comparison of $\mathbf{v}_{\mathrm{E}\times\mathrm{B}}$ and $\mathbf{v}_{\mathrm{dia}}^{\mathrm{i}}$ is not possible. Therefore, as discussed in the previous section, only the relative evolution of flows and gradient can be investigated during this phase. The time evolution during the L–I–L dithers of the main ion diamagnetic velocity

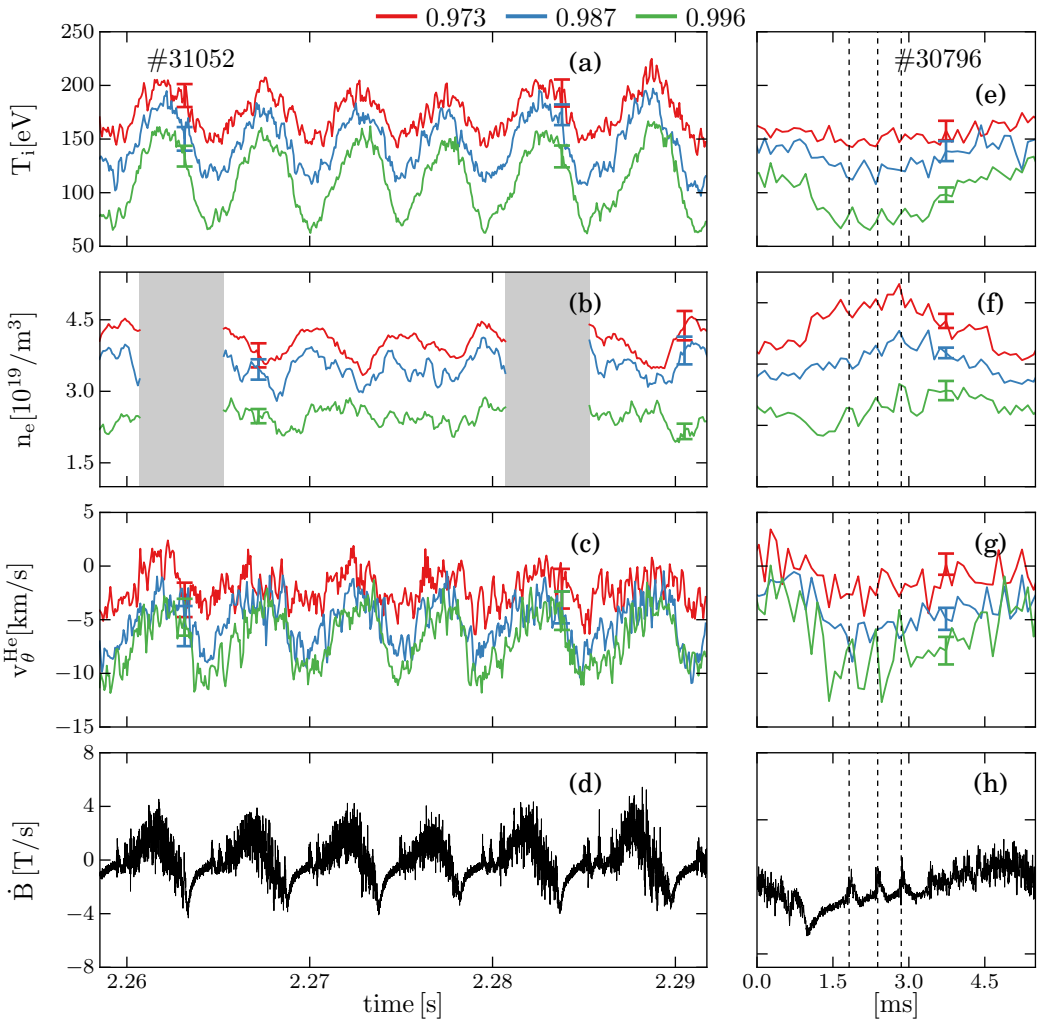

Figure 6.8: Time-traces during the L–I–L oscillations: signals from different radial positions (a,e) T_i, (b,f) n_e, (c,g) v_θ^{He}, and from (d,h) $\dot{B}_\theta$. The shaded time windows in (b) indicates when the Li-BES is switched off for background subtraction. In the left-hand plots (a,b,c,d) six L–I–L transitions from discharge #31052 are shown whereas in (e,f,g,h) a zoom-in in one transition from discharge #30796 is shown and the LCO bursts are highlighted by the dashed lines. The profiles are shown at three different radial locations in ρ_{pol} and are indicated by different colors.

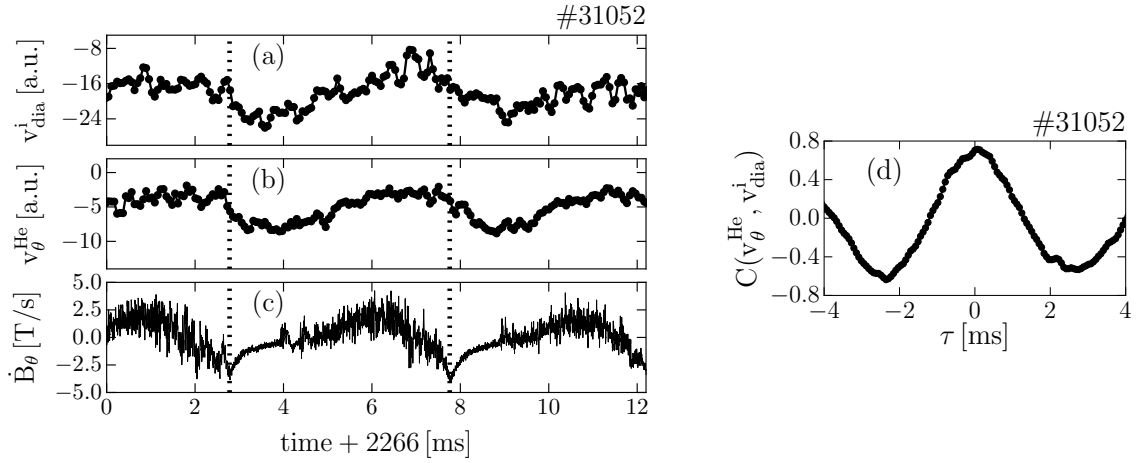

Figure 6.9: Comparison of the evolution during the L–I–L dithers of (a) the main ion diamagnetic velocity, (b) the helium poloidal velocity, (c) $\dot{B}_\theta$. In subfigure (d), cross-correlation between the helium poloidal velocity and the main ion diamagnetic velocity during the L–I–L oscillations.

approximately calculated as $v^i_{\text{dia}} = \nabla(n_e T_i)/(en_e)$ and the helium poloidal velocity at the position of the minimum of E_r are shown in figures 6.9a and 6.9b respectively. These are compared to the $\dot{B}_\theta$ signal which helps identifying the L–I transition time point (figure 6.9c). As discussed in chapter 5, the high frequency fluctuations in $\dot{B}_\theta$ disappear when the turbulence at the edge is strongly reduced (see dotted lines in figure 6.9). At roughly this time point and within the error bars, the edge v^{He}_θ and v^i_{dia} speed up, i.e. in roughly 400–600 µs both velocities are observed to change by 60−70 %. The increase of the v^{He}_θ and v^i_{dia} observed here is larger than the one due to the initial LCOs where the edge profile and velocities are modulated by 10−20 % (see figure 6.4). This might suggest that the underlying physics is different for the L–I transition and the early I-phase bursts. A high cross-correlation is found between v^{He}_θ and v^i_{dia} peaked at zero time delay indicating that the edge flows and gradients have similar trends and evolve within 100−200 µs on the same timescales (see figure 6.9d). This analysis does not provide any information about the absolute values of $\mathbf{v}_{\text{E}\times\text{B}}$ and $\mathbf{v}^{\text{i}}_{\text{dia}}$ and therefore, does not exclude a possible contribution from ZFs to the total $\mathbf{v}_{\text{E}\times\text{B}}$. These, however, must be phase locked into the neoclassical flows within 100–200 µs which seems contrary to the initial idea of how ZFs trigger the L–H transition. In [169], for instance, a strong change of the Reynold stress gradient resulting in the development of ZFs is observed triggering the L–H transition and lasting ≈ 150 µs. This observation is not in contrast with the measurements presented here.

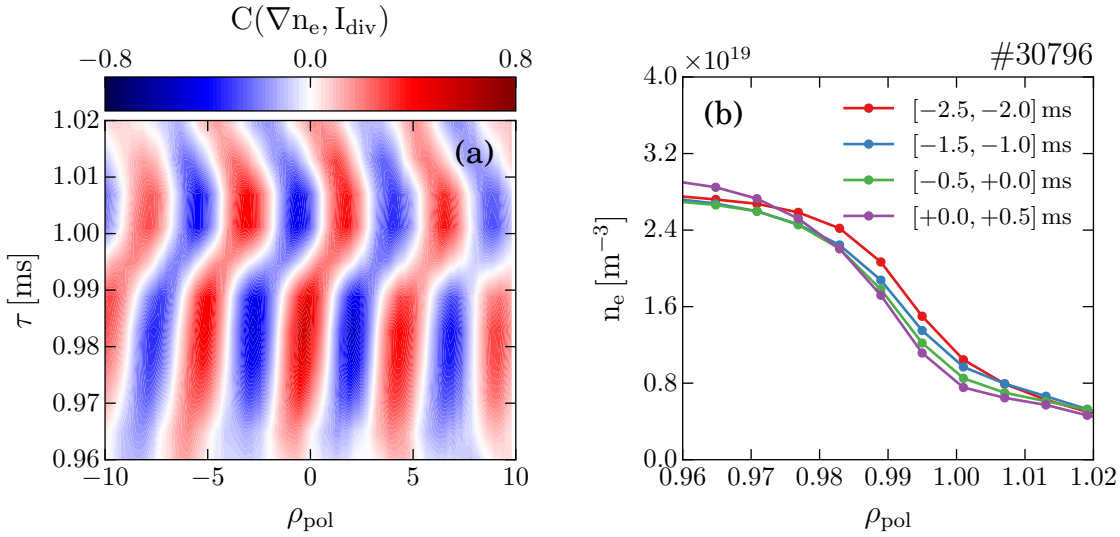

Figure 6.10: Identification of the radial position of the L–H transition: (a) radially resolved cross-correlation between ∇n_e and I_{div}, red colors indicate a high level of cross-correlation whereas blue ones indicate anti-correlation; (b) evolution of the edge electron density profiles during one L–I transition. The different colors indicate different times relative to the L–I transition.

Spatial localization of the L–H transition

As discussed in chapter 5, it is not yet clear whether the positive or the negative gradient of the $\mathbf{E}\times\mathbf{B}$ velocity (or eventually both) is responsible for turbulence suppression at the L–H transition. In this section, a new method for radially localizing the L–H transition is presented and preliminary results are reported.

As presented in chapter 2, given a certain heat flux, a reduction of the turbulent transport leads to a steepening of the gradients. Therefore, by analysing the evolution of the gradients just inside the separatrix and in the scrape-off layer the spatial localization of the L–H transition can be investigated. Note that this method is independent of the cause of the turbulence shear. To this end, the measurements of the Li-BES diagnostic have been used which can resolve the electron density profile from the edge of the plasma out into the SOL. The evolution of the density gradient ∇n_e was analysed during the L–I–L dithers where repetitive L–I transitions in similar conditions could be analysed. Similarly to the analysis performed in [77] for the n_e evolution during the I-phase pulsation, the electron density gradient was cross-correlated with the measurements of I_{div} during a stationary phase of the L–I–L oscillations. Figure 6.10a shows the radially resolved cross-correlation between ∇n_e and I_{div} for discharge #30796. Here, red colors indicate a high level of correlation whereas blue ones show anti-correlation.

The changes of the electron density gradient at the L–I–L transition seems to propagate from inward to outward, which indicates that the transport reduction is first visible further inside and then propagates outward. This might suggest that at the L–H transition the turbulence suppression happens at the inner E_r shear layer and then propagates outward. The same propagation can be directly identified in the evolution across one L–I transition of the n_e profile shown in figure 6.10b. Here, the different colors indicate different time points relative to the L–I transition. As in figure 6.10a, the steepening of the edge ∇n_e seems to take place further inside and then propagates outward. This would be consistent with the observations of the outward propagation of E_r presented in [156, 173].

This type of analysis have been performed only for few cases so far, however, it may indicate a way to unravel the roles of the inner and outer shear layer at the L–H transition. Two possible problems can limit the applicability of this test: (i) the radial alignment of the ∇n_e profile and (ii) the accuracy of the Li-BES n_e profile towards the pedestal top. In particular, at the densities at which the L–I–L transitions were observed ($n_{e,\mathrm{edge}} \approx 3.5 \times 10^{19}\,\mathrm{m}^{-3}$) the maximum of the deconvolved emissivity profile of the Li-BES is often located around $\rho_{\mathrm{pol}} = 0.99$. At radial positions further inside, the accuracy of the n_e profile reconstruction is strongly reduced (for more details see [87]). One solution would be to repeat the analysis with the newly installed ultra fast sweep reflectometry systems (for details about the diagnostic see [174]).

6.4 Discussion

To summarize this chapter, at AUG the transition from L- to H-mode is accompanied by an intermediate phase (I-phase) characterized by limit cycle like oscillations, which are thought to be driven by energy transfer from turbulence to the zonal flows. During a phase with strong zonal flows the E_r profile should deviate from the neoclassical prediction [16, 38]. However, on the timescale of the measurement ($\approx 200\,\mu\mathrm{s}$) in AUG substantial deviations are not found and the role of the zonal flows may only be important on shorter time scales. Direct comparisons between $\mathbf{E}\times\mathbf{B}$ and neoclassical flows have been carried out during stable I-phases with a constant frequency, but relatively far (of the order of 20 ms) from the L–I or the I–L transition. Therefore, these conclusions might not apply to the initial (final) I-phase bursts [70]. However, even close to the L–I or I–L transitions of the discharges presented here, the increase of turbulence is always accompanied by weaker gradients and lower $\mathbf{E}\times\mathbf{B}$ flow and the time lag between the evolution of these quantities is shorter than 150 µs. The same relation has been found at the L–I transition itself where $\mathbf{v}^{\mathrm{i}}_{\mathrm{dia}}$ and $\mathbf{v}_{\mathrm{E}\times\mathrm{B}}$ are observed to

speed up by 60–70 % in approximately 400-600 µs. These observations suggest that at AUG the temporal scales of the flows and the gradients assumed in the zonal flow based models for the L–H transition might not be well separated, and the gradient evolution could also contribute to the evolution of the turbulent stress. Additionally, the effect of the L–I transition on the edge gradients and the flows is much stronger than the one of the I-phase bursts, which only modulate $\mathbf{v}_{\mathrm{E\times B}}$ by 10–20 %. This might suggests that the I-phase bursts do not bring the plasma edge back to L-mode and thus the L–I is the important step into the improved confinement. Finally, a method to spatially localize the L–H transition is proposed based on the evolution of the electron density gradient during the L–I–L dithers. The measurements suggest an outward propagation of the gradient, which might indicate that the inner $\mathbf{v}_{\mathrm{E\times B}}$ gradient, i.e. the negative $\mathbf{E}\times\mathbf{B}$ shear gradient, is the one responsible for the turbulence suppression at the L–H transition.

7 The evolution of E_r throughout an ELM cycle

Since the discovery of the high confinement mode, significant research has focused on characterizing the dynamics of edge-localized modes (ELMs). As discussed in chapter 2, ELMs are one of the most serious technical challenge for future devices due to expulsion of high energy and particle losses onto plasma facing surfaces. Moreover, the fusion performance projections for ITER are predicted to be bound to the pedestal characteristics [175]. It is therefore fundamental to study the evolution and recovery of the edge profiles throughout the entire ELM cycle. In particular, the dynamics of the $\mathbf{E}\times\mathbf{B}$ velocity in the edge region is of fundamental interest since its shear is believed to play an important role in the reduction of the edge transport.

The evolution of flows and ions at the plasma edge before, during, and after the ELM has been, so far, poorly documented due to the required high spatial and temporal resolution to resolve the profile response adequately. Previous studies indicate that the response to the ELM onset is a rapid increase in the temperature and velocity in the high gradient region followed by a drop with a longer timescale [176]. However, a comparison between the recovery of the electron and ion profiles was not performed due to the limited time resolution (550 µs). A faster recovery of the ion temperature compared to the electron temperature was suggested in previous work [57] but, so far, not experimentally verified. Similar studies were also performed previously at ASDEX Upgrade where a collapse of the edge E_r is observed at the ELM crash [29, 177]. Here, however, the time resolution was limited to 2.3 ms. At the MAST tokamak, the dynamic evolution of the edge E_r profile during the ELM cycle was studied with a time resolution of 200 µs [178]. The edge radial electric field is observed to recover within 2 ms after the ELM crash.

In this chapter, using the new set of edge diagnostics installed at ASDEX Upgrade, a full characterization of the evolution of the edge density, temperature, poloidal and toroidal flows with a time resolution of 100 µs is presented. The dynamics of the ions and electrons are compared and the evolution of the helium as impurity is investigated. Moreover, a comparison between the measured radial electric field and its neoclassical prediction during the ELM cycle is performed.

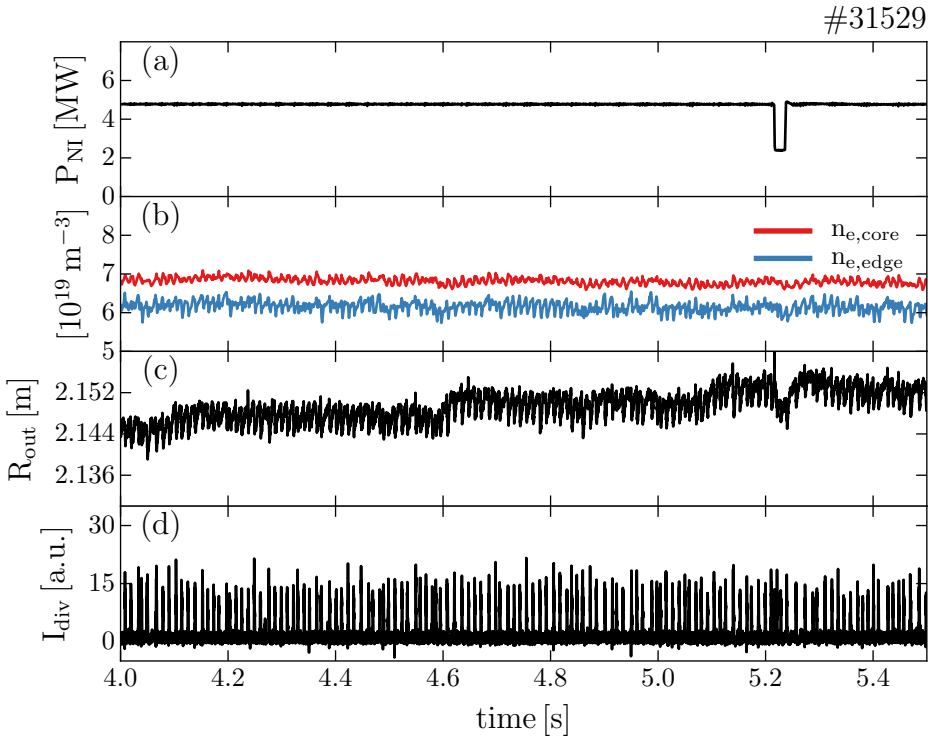

Figure 7.1: Discharge setup for edge localized mode studies: (a) neutral beam input power, (b) line averaged edge (blue) and core (red) electron densities, (c) radial position of the plasma at the outer midplane, (d) divertor shunt current.

7.1 Experimental setup and methodology

Specific discharges have been designed to fulfill the requirements for obtaining fast measurements using the upgraded edge CXRS system. As described in chapter 4, external helium seeding is necessary to improve the signal to noise ratio. Moreover, only nine lines of sight can be acquired with the fast spectrometer and therefore, a rigid scan of the plasma position in front of the LOS is required to improve the radial coverage of the measurements. Figure 7.1 shows the time traces of the NBI input power (a), the line averaged edge (blue) and core (red) electron densities (b), the outer midplane plasma position (c) and the divertor shunt current (d). The plasma is radially scanned through the views of the LOS while the other plasma parameters are kept constant. A rather constant ELM behaviour is observed in this time window with a frequency of around 80 Hz. Every ELM perturbs not only the edge profiles (see the edge density in figure 7.1b), but also the position of the plasma itself by about 5–6 mm (see figure 7.1c). This has to be taken into account when mapping the CXRS measurements onto flux coordinates, since these are performed at a fixed geometric position. To do this, a

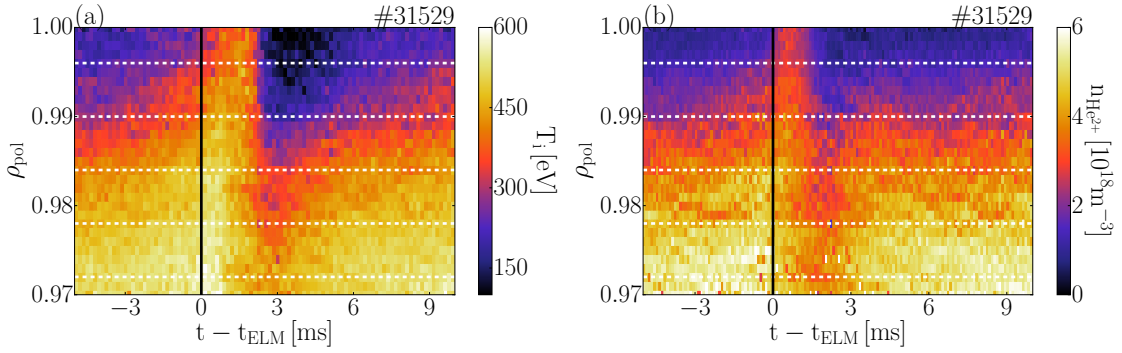

Figure 7.2: Scatter plot of ELM synchronized profile of: (a) T_i, (b) $n_{\mathrm{He}^{2+}}$. Here, brighter colors indicate higher temperature (density) whereas darker ones lower values. The white horizontal lines indicate the radial positions used in the analysis in the next section.

rigid shift based on R_{out} of the entire plasma equilibrium, reconstructed every 1 ms, is applied. This method has been compared with the results from the reconstruction of the plasma equilibrium with a time resolution of 100 µs and no systematic deviations have been found. Note that during the I-phase pulses the plasma does not show any movement, therefore in the analysis in chapter 6 this was not considered.

By combining the fast mapping and the conditional synchronization based on the I_{div} signal, detailed profiles can be extracted from the CX measurements. Note that in these discharges the direct subtraction of the passive CX radiation is not possible because no modulation of the beam was applied. Therefore, both active and passive radiation have been fitted as separated components by imposing prior conditions to the passive, such as a fixed Doppler broadening or Doppler shift. The robustness of the regression has been tested by changing the constraints to the passive radiation and within the uncertainties the same results have been obtained. The combined fit of active and passive radiation together is, however, less critical in H-mode due to the steeper edge temperature profile and therefore more localized passive emission. A cross-check of the results presented here with measurements based on beam modulation experiments is foreseen. Figure 7.2 presents the scatter plot of the ELM synchronized profile of T_i (a) and $n_{\mathrm{He}^{2+}}$ (b). Here, brighter colors indicate higher temperature (density). The white horizontal lines indicate the radial positions used in the analysis presented here. The CX measurements were performed with a time resolution of 70 µs. At the ELM onset, i.e. $t - t_{\mathrm{ELM}} = 0$, a rapid increase of T_i and n_{He} around the separatrix is observed which propagates outward. This corresponds to the ELM crash itself where particles, in this case the He^{2+} impurity, are expelled. The ELM crash presented here lasts roughly 1.5-2.0 ms but this depends on the specific plasma conditions [179]. After the ELM, a strong reduction of both T_i and $n_{\mathrm{He}^{2+}}$ is observed.

To characterize the evolution of the edge T_i and $n_{\mathrm{He}^{2+}}$ profiles and their gradients, the synchronized profiles have been fitted with a spline function. The advantage of the spline fit in comparison with the direct 2D – time and space – binning of the data is the determination of the gradients. The splines are C^2 piecewise-polynomial functions which constrain the derivative to be continuous and derivable. This is not possible if the gradients are calculated simply as differences between the binning points which then results in an unphysical scatter. The resulting T_i and $n_{\mathrm{He}^{2+}}$ profiles from the spline fit were cross-checked with binned data showing good agreement. The spline fits are only necessary for the evaluation of T_i and $n_{\mathrm{He}^{2+}}$, while for $v_\theta^{\mathrm{He}^{2+}}$ and $v_\phi^{\mathrm{He}^{2+}}$ standard 2D binning can be used since the gradients are not required. As discussed in chapter 3, the IDA algorithm is also based on spline functions thus providing the gradients automatically. This also allows the application of 2D binning of the n_e and T_e and their gradients.

A time resolution of 20 µs for the binning and the fitting has been chosen which is shorter than the acquisition time of the system, i.e. 70 µs for the CX measurements and 100 µs for the IDA algorithm. The time window used for the synchronization of the data is 1.5 s long and it is shown in figure 7.1. This approach was used in order to investigate the statistical scatter of the measurements without having to evaluate the uncertainties of the spline fits and the gradients of the profiles which are not straightforward to asses. This was only possible due to the large amount of data points available.

7.2 Edge profile evolution through the entire ELM cycle

Figure 7.3 shows the evolution of the edge profiles throughout the entire ELM cycle: (a) T_i, (b) T_e, (c) n_{He}, (d) n_e, (e) $v_\theta^{\mathrm{He}^{2+}}$ and (f) $v_\phi^{\mathrm{He}^{2+}}$. The time traces are shown relative to the ELM onset defined by the rise of the divertor shut current (see figure 7.3g). The different colors indicate four different radial locations as shown in figure 7.2. These are focussed only on the outermost ≈ 4 cm of the plasma edge. The collapse of T_i at the ELM onset is found to differ substantially from the behaviour of the electron temperature. As reported in [176], the response to the ELM onset is a rapid increase in the ion temperature close to the separatrix (green and magenta time traces in figure 7.3a) followed by a drop. This behaviour is not observed in the electron temperature measurements where close to $\rho = 1$ the profile remains almost unperturbed. This might be an effect due to the lack of information in the ECE measurements close to the separatrix owing to the shine through effect (see chapter 3). In order to avoid that, the electron cyclotron emission forward modelling fails during the ELM crash, a fixed separatrix electron temperature condition of 100 eV is set throughout the entire

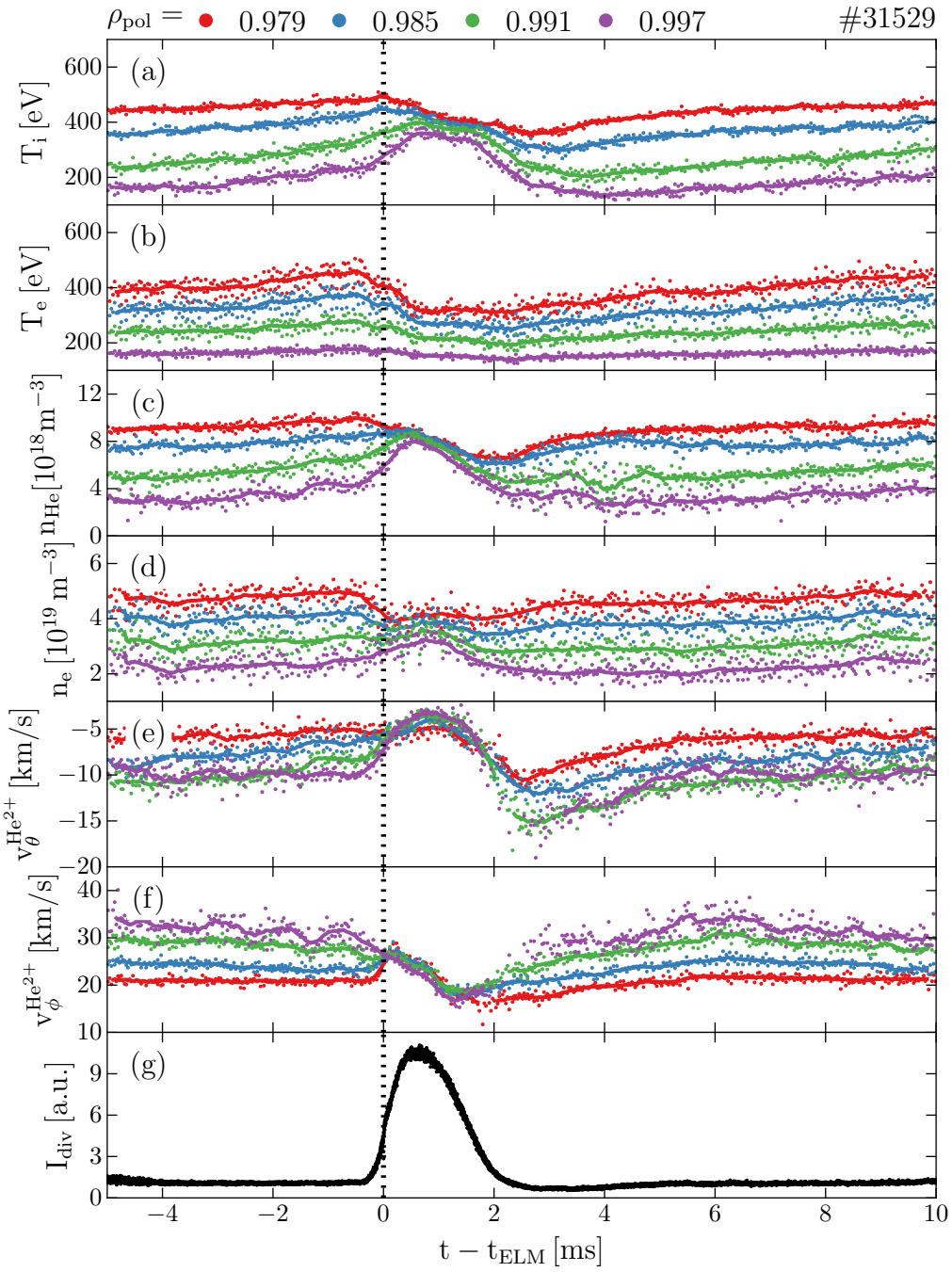

Figure 7.3: Evolution of the edge profiles relative to the ELM onset through the entire ELM cycle: (a) ion temperature, (b) electron temperature, (c) He^{2+} density, (d) electron density, (e) He^{2+} poloidal velocity, (f) He^{2+} toroidal velocity, (g) divertor shunt current. The four different colors indicate the different radial positions, reported in ρ_{pol}. The synchronized profile are binned every 20 µs to show their statistical scatter but the actual time resolution is 70 µs for the CX measurements, i.e. T_i, $v_\theta^{He^{2+}}$ and $v_\phi^{He^{2+}}$, while 100 µs for the IDA reconstruction, i.e. T_e and n_e.

ELM cycle. This allows to avoid the influence of unphysical behaviour more inside the plasma. This condition, however, is based on physics assumptions on the parallel transport in the SOL which might hold also during an ELM [180]. Thomson scattering measurements show no big changes of T_e at the real edge of the plasma ($0.98 < \rho < 1.0$) as reported in [176], supporting this hypothesis. Further inside the plasma, towards the pedestal top region, T_i and T_e show a similar behaviour (blue and red time traces in figures 7.3a,b). The electron density during the ELM crash shown in figure 7.3d has been calculated using the conditional synchronization approach described in chapter 3. The evolutions of n_e and n_{He} throughout the entire ELM cycle are similar: after the ELM crash which flattens the edge gradient, the pre-ELM conditions are re-established on a shorter time window compared to T_e and T_i, as already reported in [181]. The behaviour of the poloidal and toroidal velocities appear more puzzling (figures 7.3e,f): the gradient of $v_\theta^{\mathrm{He}^{2+}}$ shows a collapse at the ELM onset similar to the other profiles but, just after it, a fast poloidal spin-up is observed and the pre-ELM profile is re-established by its slowing down. Note that these discharges were performed in deuterium and helium is only an impurity species. Therefore, the behaviour of $v_\theta^{\mathrm{He}^{2+}}$ might be specific only to He^{2+} as impurity ion and could be different from the main ion poloidal rotation. The effect of such a trend of the helium poloidal velocity on E_r is discussed later in section 7.4. The helium toroidal velocity presents a reversed shear moving towards the separatrix, as reported in [182]. At the ELM crash, the shear suddenly collapses to an average value and shortly after the whole edge profile drops. Later, $v_\phi^{\mathrm{He}^{2+}}$ recovers to the pre-ELM profile on similar timescales as the poloidal velocity.

7.3 Edge temperature and density gradient dynamics during the ELM cycle

The study of the edge density and temperature gradient during the ELM cycle allows investigating the evolution of the heat and particle transport processes. In particular, due to the improved capabilities of the edge CXRS diagnostics, the recovery of ∇T_i and ∇T_e can be compared on AUG for the first time.

Figure 7.4 shows the evolution of the edge ∇T_i (a), ∇T_e (b), ∇n_{He} (c) and ∇n_e (d) during the entire ELM cycle. The profiles are reported at four different radial positions indicated by the different colors and synchronized relative to the increase in the divertor shunt current (figure 7.4e). The ion and electron temperature gradients show a different evolution during the ELM cycle: the ∇T_e recovery after the ELM crash lasts almost the entire inter-ELM period while ∇T_i is re-established on much shorter time scales. In particular, the maximum of ∇T_i is recovered already $\approx 4\,\mathrm{ms}$ after the ELM crash.

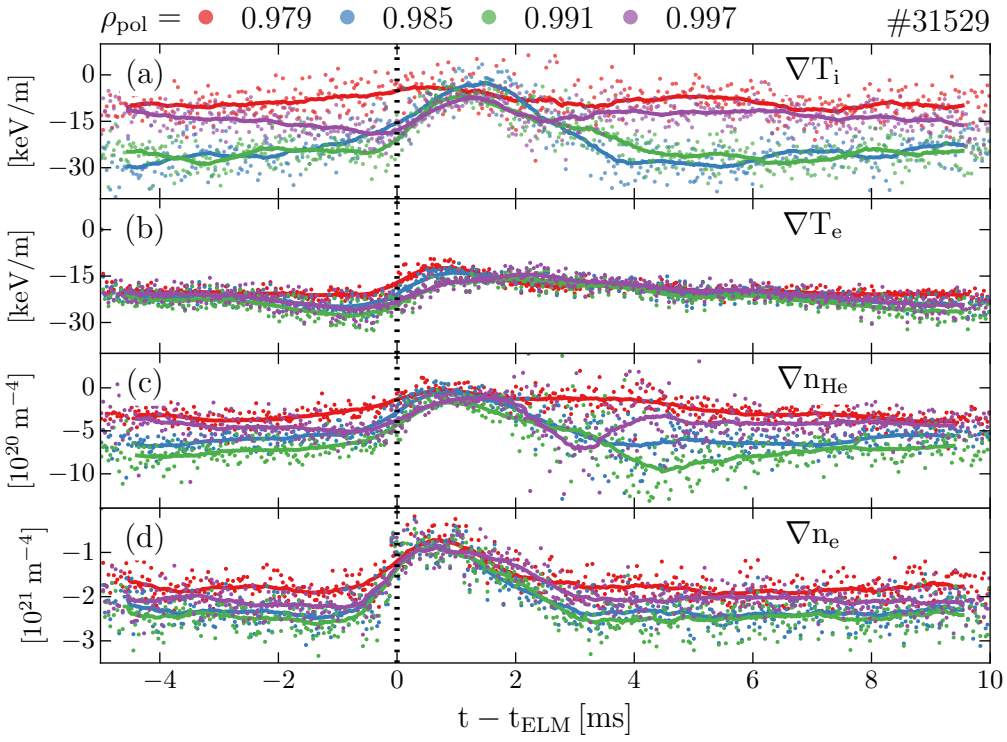

Figure 7.4: Evolution of the edge profile gradients during the entire ELM cycle: (a) ∇T_i, (b) ∇T_e, (c) ∇n_{He}, (d) ∇n_e. The gradients are synchronized to the increase of the divertor shunt current, shown in 7.1g. The profiles are shown at four different radial positions indicated by the different colors.

As already reported in [181], the electron density gradient is re-established on a shorter timescale than ∇T_e but, in this case, it does not shows any negative bump as $v_{\mathrm{pol}}^{\mathrm{He}}$ although it is often present [181]. In the discharge presented here it was not possible to assess whether the n_e measurements are not accurate enough to detect such a feature or if it really is not present at all. Within the uncertainties, ∇n_e and ∇n_{He} show a similar evolution, but ∇n_{He} has a slightly more negative gradient just after the ELM crash. Note that the ion temperature and the electron density gradients recover on similar timescales. But, once the gradients are recovered, i.e. roughly 4 ms after the ELM crash, the electron density is already at the pre-ELM levels (figure 7.3d) while T_i keeps constantly rising up to the next ELM (see figure 7.3). This suggests that the pedestal might be slightly getting wider while the maximum gradient remains constant. Also at 4 ms, high frequency magnetic fluctuations ($\nu \approx 200-500$ Hz) set on which might be responsible for the clamping of the edge gradients [183]. Further considerations on the stability of the pedestal are out of the scope of this thesis and will be performed during future investigations.

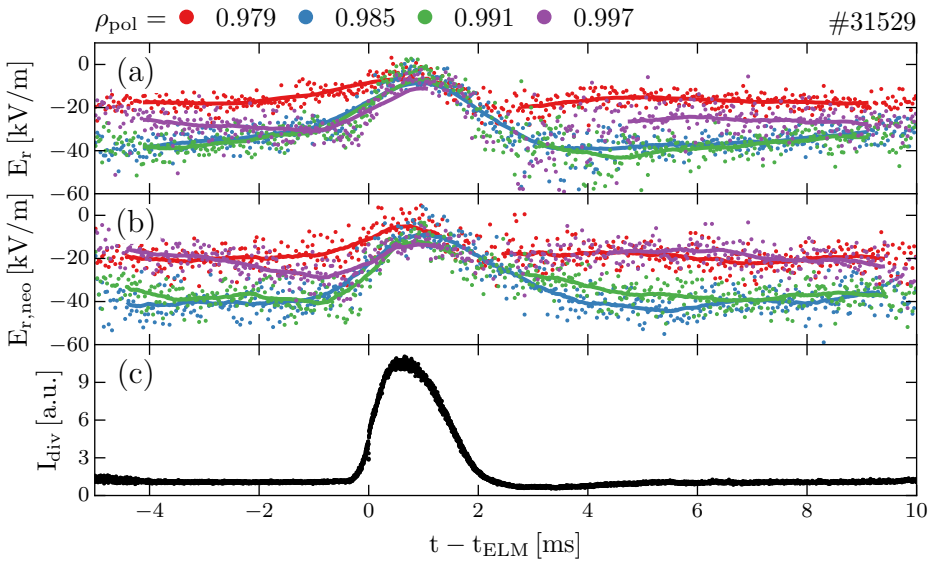

Figure 7.5: Comparison between the evolution of the edge radial electric field (a) and its neoclassical prediction (b) during the entire ELM cycle. The temporal evolution of E_r and $E_{r,\mathrm{neo}}$ are shown at four different radial positions indicated by the different colors. The time traces are synchronized relative to the onset of the divertor shunt current shown in figure (c).

7.4 The evolution of E_r during the ELM cycle and comparison with neoclassical prediction

So far the dynamics of the **E**×**B** velocity in the edge region in H-mode has been poorly documented due to the demanding diagnostics requirements. However, this is of fundamental interest since its shear is believed to play an important role in the reduction of the edge transport. In particular, earlier results at AUG clearly demonstrated that in H-mode E_r at the plasma edge is well described by neoclassical theory, consistent with results from Alcator C-Mod [31, 184]. These observations are in contrast to the findings from the DIII-D tokamak where additional contributions to E_r are suggested [185]. So far, these comparisons were however restricted to the inter-ELM phase due to limited time resolution. The improved capabilities of the edge CXRS diagnostics, now allow for a detailed investigation of E_r during the entire ELM cycle for the first time.

Figure 7.5 compares the evolution of the radial electric field measurements E_r (a) to its neoclassical prediction $E_{r,\mathrm{neo}}$ (b) during the entire ELM cycle. The values are shown at four different radial positions indicated by the different colors. The time traces are synchronized relative to the onset of the divertor shunt current, shown in figure 7.5c. The shaded regions in figures 7.5a,b highlight the time point of the re-establishment of the E_r profiles. The radial electric field gradient and its associated

shear show a strong collapse at the ELM onset which leads, for a short time (≤ 1 ms), to values close to typical L-mode profiles. The pre-ELM E_r profile is re-established in approximately 3–4 ms as already indicated by the evolution of T_i, n_{He}, v_θ^{He} and v_ϕ^{He} (figure 7.3), consistent with [176]. Within the uncertainties, the E_r and $E_{r,\mathrm{neo}}$ profiles do not show any significant deviations throughout the entire ELM cycle. In particular, just before the ELM onset, the profiles are in good agreement, consistent with previous observations [120, 184].

7.5 Discussion

In this chapter the evolution of the edge ion and electron profiles is analysed during the entire ELM cycle with unprecedented time resolution. At the ELM onset, all the edge profile gradients flatten including also the helium flows (figure 7.3). In particular, the helium poloidal velocity exhibits an unexpected negative spin up right after the ELM crash and is then slowed down to the pre-ELM values (figure 7.3e). The reversed shear of the helium toroidal flow instead flattens to one average constant value at the ELM crash and then slows down before the recovery starts. The comparison of the dynamics between the ion and electron temperatures reveals a clearly different recovery time after the ELM onset: the maximum of the ion temperature gradient is re-established in approximately 3.5 to 4 ms after the ELM crash, similar to the electron density temperature gradient whereas the electron temperature gradient recovery takes much longer, 7 to 8 ms (figure 7.4a,b). The edge radial electric field is reduced to values close to typical L-mode profiles at the ELM crash and recovers to pre-ELM values within 4 ms. From this time point on, the ion temperature and the electron density gradients remain fixed while the ion temperature keeps increasing. At the same time, i.e. 4 ms, high frequency magnetic fluctuations set on which might be responsible for the clamping of the gradients [183]. Finally, the measurements and the neoclassical prediction of E_r have been compared, showing no large discrepancies within the error bars, suggesting that the edge $\mathbf{v}_{\mathrm{E}\times\mathrm{B}}$ velocity is dominated by the edge pressure gradient during the entire ELM cycle.

8 Summary and Outlook

The success of the commercial use of the energy produced in the magnetically confined fusion reaction is constrained by the capability of confining high temperature particles. In 1982 a regime of improved confinement, the high confinement mode (H-mode), was described for the first time [6]. The H-mode shows an energy confinement time which is about a factor of two higher compared to that in the low-confinement mode (L-mode) making this regime highly desirable for future devices. The access to the H-mode in fusion plasmas occurs through the generation of an edge transport barrier in which plasma turbulence is reduced by the shear of the edge $\mathbf{E}\times\mathbf{B}$ velocity. Since about 20 years it is disputed whether the electric field is created through collisional "neoclassical" processes or by turbulence driven zonal flows (ZFs). The goal of this thesis was to characterize the dynamics of the radial electric field and its associated $\mathbf{E}\times\mathbf{B}$ velocity shear before and during the L–H transition in the ASDEX Upgrade (AUG) tokamak. The understanding of the physics underlying the L–H transition is of fundamental importance as the strength of the edge transport barrier (ETB) determines the boundary conditions for the core plasma performance. In addition, the upgrade of the edge charge exchange recombination spectroscopy (CXRS) diagnostic enabled the investigation of the edge profiles and flows during the edge localized mode (ELM) cycle.

Summary

The edge charge exchange recombination spectroscopy (CXRS) system has been upgraded during this work. The CXRS diagnostic provides temporally and radially resolved measurements of the ion temperature, density and fluid velocity from the analysis of spectroscopic emission in the visible range. By combining the poloidal and the toroidal views, the radial electric field E_r and its associated $\mathbf{E}\times\mathbf{B}$ velocity can be determined via radial force balance. During this thesis, a new design of the toroidal edge CXRS system has been developed and installed in the AUG tokamak and the poloidal system was refurbished with new lines of sight. Both systems are now equipped with a total of 52 lines of sight viewing the outermost 6 cm of the confined plasma where the transport barrier develops. The diagnostics enable fully resolved radial measurements of the plasma edge in one acquisition without the necessity of sweeping the plasma to improve the radial resolution (≈ 5 mm). The upgrade was fundamental for investigating

transient phenomenas such as the L–H transition. Furthermore, a new concept for a Czerny-Turner like spectrometer has been designed which allows to acquire up to 9 channels with a repetition time of 15 µs. A good signal to noise ratio has been obtained in discharges with external impurity seeding with a time resolution down to 70 µs. This unprecedented temporal resolution opens up for the first time the possibility to directly address the dynamics of the $\mathbf{E}\times\mathbf{B}$ flow and its neoclassical and turbulent contributions during fast transient events, such as the L–H transition and edge localized modes.

In order to address the condition for the H-mode onset which possibly exists in the $\mathbf{E}\times\mathbf{B}$ velocity shear, it is necessary to understand the dynamics of the L–H and H–L transition process and to define a time point where the plasma changes its confinement. In particular, a correlation between the E_r profile just before the confinement change and the heating power P_{thr} required to access the H-mode has been investigated in order to experimentally relate the macroscopic effects of P_{thr} to the microscopic $\mathbf{E}\times\mathbf{B}$ shear and the turbulence properties. To this end, a series of discharges at various toroidal magnetic fields, different electron densities in both hydrogen and deuterium plasmas has been performed. Within the error bars, a critical $\mathbf{E}\times\mathbf{B}$ velocity minimum, i.e. a proxy of the $\mathbf{E}\times\mathbf{B}$ flow shear, has been found of around $\min(v_{\mathrm{E}\times\mathrm{B}}) = 6.8 \pm 1.0$ km/s. The E_r minimum is found to scale approximately linear with the magnetic field B_ϕ indicating that the $\mathbf{E}\times\mathbf{B}$ velocity itself is the important player for the L–H transition onset rather than E_r itself. This was indeed expected because the actual turbulence shear is due to $\mathbf{v}_{\mathrm{E}\times\mathrm{B}} \approx E_r/B_\phi$ and not due to E_r alone. The findings presented in this work combined with [82, 83, 150, 151] point to a fundamental role of the main ion pressure profile in the L–H transition physics. Assuming that the edge turbulence characteristics are similar for the different plasma parameters investigated here, one might extrapolate that the L–H transition power threshold dependencies on plasma control parameters can be interpreted as a requirement for reaching the critical ion pressure gradient and thus, a critical $\mathbf{E}\times\mathbf{B}$ shear.

The spatio-temporal interplay between turbulence, neoclassical and zonal flows has been investigated at the L–H and H–L transitions in the edge region of the ASDEX Upgrade tokamak. Close to both transitions, an intermediate phase (I-phase) characterized by "limit cycle like oscillations" (LCOs) is observed, in which periodic bursts of turbulence correlate with the reduction of the $\mathbf{E}\times\mathbf{B}$ flow and the relaxation of the temperature and density gradients. In the "late" I-phase the $\mathbf{E}\times\mathbf{B}$ velocity is dominated by the neoclassical flows within the error bars, indicating that turbulence driven flows are small. The comparison has been performed with an unprecedented time resolution of the measurements of the neoclassical flows, i.e. down to 100 µs. Therefore, the zonal flows may only be important on shorter timescales. Periodic dithers between L-mode

and the I-phases with LCOs are also observed just before the H-mode onset. The E_r dynamics of the L–I transitions seems to be different from that in between the I-phase bursts. The steepening of the edge profiles and flows at the L–I transitions is larger than the reduction due to the I-phase pulses, which suggests a different physics process behind the LCOs and the transition from L-mode to the I-phase. Within the experimental uncertainties, no time delay is found in between the neoclassical flow and the measured $\mathbf{E}\times\mathbf{B}$ flow during the complete evolution from L-mode to H-mode, suggesting the fundamental role of the neoclassical flow in the fast dynamics of the L–H transition. These observations indicate more an ELM-like behaviour of the plasma during the I-phase. Moreover, they help in restricting the models for the zonal flows which need to include the fast response of the neoclassical flows in which the ZFs may be phase locked.

The steep gradients associated with ETBs provide a source of free energy for magneto-hydrodynamic (MHD) instabilities. Therefore, H-mode plasmas are usually accompanied by the appearance of so-called edge localised modes (ELMs) which periodically expel particles and energy from the plasma edge limiting the plasma performance and eventually damaging the first wall. Hence, the dynamics of the edge profiles and flows throughout the ELM cycle is of fundamental interest for understanding the mechanisms which control the pedestal. In this work, for the first time, the temperature, density, and the flow profiles at the plasma edge have been characterized throughout the entire type-I ELM cycle with a time resolution of 70 µs. At the ELM onset, all the edge profiles are observed to collapse including the poloidal and the toroidal flows. The relaxation lasts about 2 ms. For the first time, the recovery of both the ion and electron temperatures after the ELM crash could be investigated. The ion temperature gradient is re-established in approximately 4 ms after the ELM crash similar to the electron density while the electron temperature gradient recovery takes much longer, 7 to 8 ms. The resulting radial electric field is observed to recover within 4 ms after the ELM crash. Within the experimental uncertainties, E_r is in agreement with the neoclassical prediction. This means that the main ion pressure gradient controls the edge $\mathbf{E}\times\mathbf{B}$ flow, which plays an important role in determining the strength of the edge transport barrier. Moreover, the rapid recovery of the ion temperature gradient contributes significantly to the edge current density shortly after the ELM crash, stabilizing the ballooning modes which are thought to be one of the dominant mechanisms regulating the pedestal characteristics in H-mode.

Outlook

As presented in this thesis, a threshold of the $\mathbf{E}\times\mathbf{B}$ velocity shear for the H-mode onset has been found, which is independent of the electron density, the toroidal magnetic field and the plasma isotope mass (deuterium or hydrogen). However, the L–H transition power threshold shows other dependencies, for instance the ∇B drift direction or the X-point position. Hence, in the future a detailed characterization of the E_r profile in plasmas where the ∇B drift direction or the X-point position is varied might shed more light on these dependences of P_{thr}. In addition, it is fundamental to investigate the characteristics of the edge turbulence close to the H-mode onset in order to link the macroscopic changes of P_{thr} not only to the $\mathbf{E}\times\mathbf{B}$ flow shear but also to the turbulence behaviour.

The findings on the interaction between turbulence, zonal and neoclassical flows presented in this work can be best confirmed in helium plasmas in which the charge exchange diagnostic can measure the main ions. This allows a direct comparison of the diamagnetic velocity of the main ions and the $\mathbf{E}\times\mathbf{B}$ velocity without using the measurements of the electron density. Moreover, the time resolution can be decreased further, down to the hardware limit due to the enhanced signal to noise ratio.

The high acquisition rate spectrometer developed in this work can also be employed to study the behaviour of the flows in the scrape-off layer by measuring the emission of passive impurity lines in the visible light range. This could be an additional source of information to understand the physics of the L–H transition.

Finally, this work opened up the possibility to study both the ion and electron channels and the behaviour of E_r throughout the entire ELM cycle. This investigation can be extended to different types of ELMs. In particular, correlations between the recovery of the edge profiles and the ELM characteristics can be investigated.

Bibliography

[1] J. D. Lawson. “Some Criteria for a Power producing thermonuclear reactor”, *Atomic Energy Research Establishment* GP/R 1807, (1955).

[2] E. I. Moses. “Ignition on the National Ignition Facility: a path towards inertial fusion energy”, *Nucl. Fusion* 49, 10 (2009), p. 104022.

[3] J. P. Freidberg. *Plasma Physics and Fusion Energy*. Cambrige University Press, 2007.

[4] U. Stroth. *Plasmaphysik*. Vieweg+Teubner Verlag, 2011. ISBN: 9978-3-8348-1615-3 780199592234.

[5] T. Happel et al. “The optimized steerable W-band Doppler reflectometer on ASDEX Upgrade: possibilities and issues,” Palaiseau, France: Proc. 11$^{\text{th}}$ International Reflectometry Workshop, 2013.

[6] F. Wagner et al. “Regime of Improved Confinement and High Beta in Neutral-Beam-Heated Divertor Discharges of the ASDEX Tokamak”, *Phys. Rev. Lett.* 49, (1982), pp. 1408–1412.

[7] H. Biglari et al. “Influence of sheared poloidal rotation on edge turbulence”, *Phys. of Fluids B: Plasma Phys.* 2, 1 (1990), p. 1. ISSN: 08998221.

[8] E. Viezzer. “Radial electric field studies in the plasma edge of ASDEX upgrade.” PhD thesis. LMU München, 2012.

[9] H. Zohm. “Dynamic behavior of the L-H transition”, *Phys. Rev. Lett.* 72, (1994), pp. 222–225.

[10] P. Manz. *Lectures on turbulent transport in fusion*. Technische Universität München, 2015.

[11] J. Wesson. *Tokamaks*. International Series of Monographs on Physics. OUP Oxford, 2011. ISBN: 9780199592234.

[12] J. Hugill. “Transport in tokamaks – a review of experiment”, *Nucl. Fusion* 23, 3 (1983), p. 331.

[13] F. Wagner et al. “Transport in toroidal devices-the experimentalist’s view”, *Plasma Phys. and Contr. Fusion* 35, 10 (1993), p. 1321.

[14] U. Stroth et al. “On the interaction of turbulence and flows in toroidal plasmas”, *Plasma Phys. and Cont. Fusion* 53, 2 (2011), p. 024006. ISSN: 0741-3335.

[15] L. Prandtl. “Z. angew”, *Math. Mech.* 5, (1925), pp. 136–139.

[16] P. Manz et al. “Physical Mechanism behind Zonal-Flow Generation in Drift-Wave Turbulence”, *Phys. Rev. Lett.* 103, 16 (2009), p. 165004. ISSN: 0031-9007.

[17] P. Terry. “Suppression of turbulence and transport by sheared flow”, *Rev. Mod. Phys.* 72, (2000), pp. 109–165.

[18] S. Kida. “Motion of an Elliptic Vortex in a Uniform Shear Flow”, *J. Phys. Soc. Jpn.* 50, 10 (1981), pp. 3517–3520.

[19] S. I. Braginskii. “Transport Processes in a Plasma”, *Rev. of Plasma Phys.* 1, (1965), p. 205.

[20] P. Helander et al. *Collisional Transport in Magnetized Plasmas*. Cambridge Monographs on Plasma Physics. Cambridge University Press, 2005. ISBN: 9780521020985.

[21] F. L. Hinton et al. “Theory of plasma transport in toroidal confinement systems”, *Rev. Mod. Phys.* 48, (1976), pp. 239–308.

[22] A. Peeters. *Some remarks on neo-classics*. Lecture. 2015.

[23] V. Shafranov. *Reviews of Plasma Physics*. Reviews of Plasma Physics Bd. 24. Springer Berlin Heidelberg, 2008. ISBN: 9783540745761.

[24] P. H. Diamond et al. “Zonal flows in plasma – a review”, *Plasma Phys. and Contr. Fusion* 47, 5 (2005), R35.

[25] K. C. Shaing et al. “Neoclassical theory inside transport barriers in tokamaks”, *Phys. of Plasmas* 19, 2, 022502 (2012), p. 10.

[26] C. S. Chang et al. “X-transport: A baseline nonambipolar transport in a diverted tokamak plasma edge”, *Phys. of Plasmas* 9, 9 (2002), pp. 3884–3892.

[27] Y. B. Kim et al. “Neoclassical poloidal and toroidal rotation in tokamaks”, *Phys. of Fluids B: Plasma Phys.* 3, 8 (1991), p. 2050. ISSN: 08998221.

[28] S. Hirshman et al. “Neoclassical transport of impurities in tokamak plasmas”, *Nucl. Fusion* 21, 9 (1981), p. 1079.

[29] E. Viezzer et al. “High-accuracy characterization of the edge radial electric field at ASDEX Upgrade”, *Nucl. Fusion* 53, 5 (2013), p. 053005.

[30] A. G. Peeters. "Reduced charge state equations that describe Pfirsch Schlüter impurity transport in tokamak plasma", *Phys. of Plasmas* 7, 1 (2000), pp. 268–275.

[31] E. Viezzer et al. "Evidence for the neoclassical nature of the radial electric field in the edge transport barrier of ASDEX Upgrade", *Nucl. Fusion* 54, 1 (2014), p. 012003.

[32] A. Fujisawa. "A review of zonal flow experiments", *Nucl. Fusion* 49, 1 (2009), p. 013001.

[33] F. H. Busse. "Convection driven zonal flows and vortices in the major planets", *Chaos* 4, 2 (1994), pp. 123–134.

[34] P. H. Diamond et al. "Theory of mean poloidal flow generation by turbulence", *Phys. of Fluids B* 3, 7 (1991), pp. 1626–1633.

[35] S. V. Novakovskii et al. "The radial electric field dynamics in the neoclassical plasmas", *Phys. of Plasmas* 4, 12 (1997), pp. 4272–4282.

[36] K. Itoh et al. "The impact of improved confinement on fusion research", *Fusion Eng. Des.* 15, 4 (1991), pp. 297–308. ISSN: 0920-3796.

[37] P. H. Diamond et al. "Self-Regulating Shear Flow Turbulence: A Paradigm for the *L* to *H* Transition", *Phys. Rev. Lett.* 72, (1994), pp. 2565–2568.

[38] E.-j. Kim et al. "Zonal Flows and Transient Dynamics of the *L*-*H* Transition", *Phys. Rev. Lett.* 90, (2003), p. 185006.

[39] K. Itoh et al. "Physics of zonal flows", *Phys. of Plasmas* 13, 5, 055502 (2006).

[40] F. Ryter et al. "Experimental Characterization of the Electron Heat Transport in Low-Density ASDEX Upgrade Plasmas", *Phys. Rev. Lett.* 86, (2001), pp. 5498–5501.

[41] X. Garbet et al. "Profile stiffness and global confinement", *Plasma Phys. and Contr. Fusion* 46, 9 (2004), p. 1351.

[42] F. Ryter et al. "Experimental Evidence for Gradient Length-Driven Electron Transport in Tokamaks", *Phys. Rev. Lett.* 86, (2001), pp. 2325–2328.

[43] D. Mikkelsen et al. "Stiff temperature profiles in JT-60U ELMy H-mode plasmas", *Nucl. Fusion* 43, 1 (2003), p. 30.

[44] F. Ryter et al. "H-mode threshold and confinement in helium and deuterium in ASDEX Upgrade", *Nucl. Fusion* 49, 6 (2009), p. 062003.

[45] F. Ryter et al. "H mode power threshold database for ITER", *Nucl. Fusion* 36, 9 (1996), p. 1217.

[46] Y. R. Martin et al. "Power requirement for accessing the H-mode in ITER", *J. Phys.: Conference Serires* 123, (2008), p. 012033. ISSN: 1742-6596.

[47] C. Maggi et al. "L–H power threshold studies in JET with Be/W and C wall", *Nucl. Fusion* 54, 2 (2014), p. 023007.

[48] Y. Ma et al. "Scaling of H-mode threshold power and L–H edge conditions with favourable ion grad- B drift in Alcator C-Mod tokamak", *Nucl. Fusion* 52, 2 (2012), p. 023010.

[49] S. J. Fielding et al. "H-modes on COMPASS-D with high-power ECRH", *Plasma Phys. and Contr. Fusion* 40, 5 (1998), p. 731.

[50] T. Fukuda et al. "Reduction of L-H transition threshold power under the W-shaped pumped divertor geometry in JT-60U", *Plasma Phys. and Contr. Fusion* 42, 5A (2000), A289.

[51] E. Righi et al. "Isotope scaling of the H–mode power threshold on JET", *Nucl. Fusion* 39, 3 (1999), p. 309.

[52] A. Hubbard et al. "Threshold conditions for transitions to I-mode and H-mode with unfavourable ion grad B drift direction", *Nucl. Fusion* 52, 11 (2012), p. 114009.

[53] Y. Andrew et al. "JET divertor geometry and plasma shape effects on the L–H transition threshold", *Plasma Phys. and Contr. Fusion* 46, 5A (2004), A87.

[54] P. Gohil et al. "Dependence of the H-mode power threshold on toroidal plasma rotation in the DIII-D tokamak", *J. Phys.: Conference Serires* 123, 1 (2008), p. 012017.

[55] H. Zohm. "Edge localized modes (ELMs)", *Plasma Phys. and Contr. Fusion* 38, 2 (1996), p. 105.

[56] A. Herrmann. "Overview on stationary and transient divertor heat loads", *Plasma Phys. and Contr. Fusion* 44, 6 (2002), p. 883.

[57] M. Dunne. "Inter-ELM evolution of the edge current density profile on the ASDEX Upgrade tokamak." PhD thesis. National University of Ireland, Cork, 2013.

[58] J. Connor et al. "A review of theories of the L-H transition", *Plas. Phys. and Cont. Fusion* 1, (2000).

[59] K. C. Shaing et al. "Bifurcation theory of poloidal rotation in tokamaks: A model for L - H transition", *Phys. Rev. Lett.* 63, (1989), pp. 2369–2372.

[60] S.-I. Itoh et al. "Model of L to H-Mode Transition in Tokamak", *Phys. Rev. Lett.* 60, (1988), pp. 2276–2279.

[61] R. J. Groebner et al. "Role of edge electric field and poloidal rotation in the L - H transition", *Phys. Rev. Lett.* 64, (1990), pp. 3015–3018.

[62] H. Zohm et al. "Investigation of the bifurcation character of the H-mode in ASDEX Upgrade", *Plas. Phys. and Cont. Fusion* 37, 4 (1995), pp. 437–446. ISSN: 0741-3335.

[63] R. Colchin et al. "Slow L-H Transitions in DIII-D Plasmas", *Phys. Rev. Lett.* 88, 25 (2002), p. 255002. ISSN: 0031-9007.

[64] S. J. Zweben et al. "Quiet periods in edge turbulence preceding the L-H transition in the National Spherical Torus Experiment", *Phys. of Plasmas* 17, 10, 102502 (2010).

[65] T. Estrada et al. "L-H Transition Experiments in TJ-II", *Contr. Plasma Phys.* 50, 6-7 (2010), pp. 501–506. ISSN: 1521-3986.

[66] G. D. Conway et al. "Mean and Oscillating Plasma Flows and Turbulence Interactions across the L-H Confinement Transition", *Phys. Rev. Lett.* 106, 6 (2011), p. 065001. ISSN: 0031-9007.

[67] G. S. Xu et al. "First Evidence of the Role of Zonal Flows for the *L-H* Transition at Marginal Input Power in the EAST Tokamak", *Phys. Rev. Lett.* 107, (2011), p. 125001.

[68] L. Schmitz et al. "Role of Zonal Flow Predator-Prey Oscillations in Triggering the Transition to H-Mode Confinement", *Phys. Rev. Lett.* 108, 15 (2012), p. 155002. ISSN: 0031-9007.

[69] E. R. Solano et al. "M-mode : axi-symmetric magnetic oscillation and ELM-less H-mode in JET," *EPS*. 2012, pp. 4–7.

[70] J. Cheng et al. "Dynamics of Low-Intermediate-High-Confinement Transitions in Toroidal Plasmas", *Phys. Rev. Lett.* 110, 26 (2013), p. 265002. ISSN: 0031-9007.

[71] T. Kobayashi et al. "Spatiotemporal Structures of Edge Limit-Cycle Oscillation before L-to-H Transition in the JFT-2M Tokamak", *Phys. Rev. Lett.* 111, 3 (2013), p. 035002. ISSN: 0031-9007.

[72] K. Miki et al. "Spatio-temporal evolution of the L–I–H transition", *Phys. of Plasmas* 19, 9, 092306 (2012).

[73] M. A. Malkov et al. "Linking the micro and macro: L-H transition dynamics and threshold physics", *Phys. of Plasmas* 22, 3, 032506 (2015).

[74] B. D. Scott. "Energetics of the interaction between electromagnetic ExB turbulence and zonal flows", *New J. Phys.* 7, 1 (2005), p. 92.

[75] G. Xu et al. "Dynamics of L-H transition and I-phase in EAST", *Nucl. Fusion* 54, 10 (2014), p. 103002.

[76] Y. Xu et al. "Dynamics of low–intermediate–high-confinement transitions in the HL-2A tokamak", *Plasma Phys. and Contr. Fusion* 57, 1 (2015), p. 014028.

[77] G. Birkenmeier et al. "Characterisation and frequency scaling of limit-cycle oscillations close to L- to H-transitions", *Plasma Phys. and Contr. Fusion* (2015).

[78] F. L. Hinton. "Thermal confinement bifurcation and the L- to H-mode transition in tokamaks", *Phys. of Fluids B* 3, 3 (1991), pp. 696–704.

[79] C.-S. Chang et al. "Can the H-mode be sustained by neoclassical mechanisms?" *TTF Conference*. 2007.

[80] B. Scott. *Gyrokinetic Theory and Dynamics of the Tokamak Edge*. 2015.

[81] K. Miki et al. "Physics of Stimulated L→H Transitions", *Phys. Rev. Lett.* 110, 19 (2013), p. 195002.

[82] F. Ryter et al. "Experimental evidence for the key role of the ion heat channel in the physics of the L–H transition", *Nucl. Fusion* 54, 8 (2014), p. 083003. ISSN: 0029-5515.

[83] P. Sauter et al. "L- to H-mode transitions at low density in ASDEX Upgrade", *Nucl. Fusion* 52, 1 (2012), p. 012001. ISSN: 0029-5515.

[84] E. Delabie et al. "Overview and Interpretation of L-H Threshold experiments on JET with the ITER-like Wall," *IAEA*. 2014.

[85] L. M. Shao et al. "On the role of the edge density profile for the L–H transition power threshold in ASDEX Upgrade", *Plasma Phys. and Contr. Fusion* 58, 2 (2016), p. 025004.

[86] R. Fischer et al. "Integrated Data Analysis of Profile Diagnostics at ASDEX Upgrade", *Fusion Sci. Technol.* 58, 2 (2010), pp. 675–684.

[87] M. Willensdorfer et al. "Characterization of the Li-BES at ASDEX Upgrade", *Plasma Phys. and Contr. Fusion* 56, 2 (2014), p. 025008.

[88] W. Suttrop. *Practical Limitations to Plasma Edge Electron Temperature Measurements by Radiometry of Electron Cyclotron Emission*. Tech. rep. IPP Report 1/306. Max-Planck-Institute for Plasma Physics, 1997.

[89] S. K. Rathgeber et al. "Estimation of profiles of the effective ion charge at ASDEX Upgrade with Integrated Data Analysis", *Plasma Phys. and Contr. Fusion* 52, 9 (2010), p. 095008.

[90] B. Kurzan et al. “Edge and core Thomson scattering systems and their calibration on the ASDEX Upgrade tokamak”, *Rev. Sci. Instrum.* 82, 10, 103501 (2011).

[91] C. De Boor. *A Practical Guide to Splines*. Applied Mathematical Sciences Bd. 27. Springer-Verlag, 1978. ISBN: 9783540903567.

[92] J. Schweinzer et al. “Reconstruction of plasma edge density profiles from Li I (2s-2p) emission profiles”, *Plasma Phys. and Contr. Fusion* 34, 7 (1992), p. 1173.

[93] R. Fischer et al. “Probabilistic lithium beam data analysis”, *Plasma Phys. and Contr. Fusion* 50, 8 (2008), p. 085009.

[94] A. Mlynek et al. “Design of a digital multiradian phase detector and its application in fusion plasma interferometry”, *Rev. Sci. Instrum.* 81, 3, 033507 (2010).

[95] S. K. Rathgeber et al. “Estimation of edge electron temperature profiles via forward modelling of the electron cyclotron radiation transport at ASDEX Upgrade”, *Plasma Phys. and Contr. Fusion* 55, 2 (2013), p. 025004.

[96] D. Sheffield et al. *Plasma Scattering of Electromagnetic Radiation (Second Edition)*. Second Edition. Boston: Academic Press, 2011, pp. i–ii. ISBN: 978-0-12-374877-5.

[97] G. D. Conway et al. “Interaction of Mean and Oscillating Plasma Flows Across Confinement Mode Transitions”, *Plasma and Fusion Research* 5, S2005 (2010).

[98] M. Hirsch et al. “Doppler reflectometry for the investigation of propagating density perturbations”, *Plasma Phys. and Contr. Fusion* 43, 12 (2001), p. 1641.

[99] T. Happel et al. “Core turbulence behavior moving from ion-temperature-gradient regime towards trapped-electron-mode regime in the ASDEX Upgrade tokamak and comparison with gyrokinetic simulation”, *Phys. of Plasmas* 22, 3, 032503 (2015).

[100] T. Estrada et al. “Sheared flows and transition to improved confinement regime in the TJ-II stellarator”, *Plasma Phys. and Contr. Fusion* 51, 12 (2009), p. 124015.

[101] S. Mirnov et al. “The nature of large-scale instabilities in the tokamak”, *Soviet Physics JETP* 33, 6 (1971), p. 1134.

[102] M. Maraschek et al. “Active control of MHD instabilities by ECCD in ASDEX Upgrade”, *Nucl. Fusion* 45, 11 (2005), p. 1369.

[103] M. Maraschek et al. “Measurement and impact of the n=1 intrinsic error field at ASDEX Upgrade,” *EPS Helsinki,* 2013.

[104] N. Peacock. “Fusion spectroscopy”, English, *Astrophysics and Space Science* 237, 1-2 (1996), pp. 341–399. ISSN: 0004-640X.

[105] M. G. von Hellermann et al. “Complex Spectra in Fusion Plasmas”, *Phys. Scr.* 2005, T120 (2005), p. 19.

[106] R. Fonck et al. “Determination of plasma-ion velocity distribution via charge-exchange recombination spectroscopy”, *Phys. Rev. A* 29, (1984), pp. 3288–3309.

[107] R. Isler. “A review of charge-exchange spectroscopy and applications to fusion plasmas”, *Phys. Scr.* 650, (1987).

[108] M. von Hellermann et al. “Analytical approximation of cross-section effects on charge exchange spectra observed in hot fusion plasmas”, *Plasma Phys. and Contr. Fusion* 37, 2 (1995), p. 71.

[109] B. Geiger. “Fast-ion transport studies using FIDA spectroscopy at the ASDEX Upgrade tokamak.” PhD thesis. LMU, 2013.

[110] Atomic Data and Analysis Structure (ADAS). http://open.adas.ac.uk/.

[111] J. Huba. *NRL Plasma Formulary.* Naval Research Laboratory, 2007.

[112] A. Lebschy et al. “Indirect measurement of the poloidal rotation velocity in the core of ASDEX Upgrade plasmas with charge exchange recombination spectroscopy,” *42nd EPS Conference on Plasma Physics.* 2015.

[113] R. M. McDermott, *in preparation* (2016).

[114] T. Pütterich. “Fast CXRS-Measurements in the Edge Transport Barrier of ASDEX Upgrade,” *35th EPS Conference on Plasma Physics.* 2008.

[115] Leica. http://us.leica-camera.com/.

[116] Princeton Instruments. http://www.princetoninstruments.com/.

[117] R. E. Bell. “Exploiting a transmission grating spectrometer”, *Rev. Sci. Instrum.* 75, 10 (2004), p. 4158. ISSN: 00346748.

[118] National Institute of Standards and Technology. http://www.nist.gov/.

[119] FARO. http://ww.faro.com/.

[120] E. Viezzer et al. “Parameter dependence of the radial electric field in the edge pedestal of hydrogen, deuterium and helium plasmas”, *Plasma Phys. and Cont. Fusion* 56, 7 (2014), p. 075018. ISSN: 0741-3335.

[121] L. Schmitz et al. "The role of zonal flows and predator-prey oscillations in triggering the formation of edge and core transport barriers", *Nucl. Fusion* 54, 7 (2014), p. 073012.

[122] A. B. Williams et al. *Electronic Filter Design Handbook, Fourth Edition*. McGraw-Hill, 2006.

[123] S. H. Müller et al. "Direct observations of L-I-H and H-I-L transitions with the X-point reciprocating probe in ASDEX Upgrade", *Phys. of Plasmas* 21, 4 (2014), p. 042301. ISSN: 1070-664X.

[124] G. Xu et al. "Study of the L–I–H transition with a new dual gas puff imaging system in the EAST superconducting tokamak", *Nucl. Fusion* 54, 1 (2014), p. 013007. ISSN: 0029-5515.

[125] T. Kass et al. "Characteristics of type I and type III ELM precursors in ASDEX upgrade", *Nucl. Fusion* 38, 1 (1998), p. 111.

[126] R. Sartori et al. "Study of Type III ELMs in JET", *Plasma Phys. and Contr. Fusion* 46, 5 (2004), p. 723.

[127] G. Xiang et al. "Observation of Pedestal Plasma Turbulence on EAST Tokamak", *Plasma Science and Technology* 15, 8 (2013), p. 732.

[128] J. Cheng et al. "Low–intermediate–high confinement transition in HL-2A tokamak plasmas", *Nucl. Fusion* 54, 11 (2014), p. 114004.

[129] A. Silva et al. "Recent improvements of the broadband FMCW reflectometry system for density profile measurements on ASDEX Upgrade", *Rev. Sci. Instrum.* 77, 10, 10E932 (2006).

[130] S. C. da Graca. "MHD and fast particle mode studies using fast frequency hopping reflectometers on the ASDEX Upgrade tokamak." PhD thesis. Universidade Técnica de Lisboa, 2009.

[131] S. Potzel et al. "Characterization of the fluctuating detachment state in ASDEX Upgrade", *J. Nucl. Mater.* 438, Supplement, (2013). Proceedings of the 20th International Conference on Plasma-Surface Interactions in Controlled Fusion Devices, S285–S290. ISSN: 0022-3115.

[132] L. Shao et al. "Oscillating plasma states around the L-H transition at ASDEX Upgrade", *in preparation* (2015).

[133] R. Wenninger et al. "Solitary magnetic perturbations at the ELM onset", *Nucl. Fusion* 52, 11 (2012), p. 114025.

[134] M. Cavedon et al. "Fast edge charge exchange measurements at the L-H transition in ASDEX Upgrade," *19th Joint EU-US Transport Task Force Meeting*. 2014.

[135] E. Delabie et al. "L-H transitions on JET with the ITER-like Wall," *19th Joint EU-US Transport Task Force Meeting*. 2014.

[136] A. Loarte et al. "Self-Sustained Divertor Plasma Oscillations in the JET Tokamak", *Phys. Rev. Lett.* 83, (1999), pp. 3657–3660.

[137] S. Potzel. "Experimental classification of divertor detachment." PhD thesis. 2012.

[138] P. C. Stangeby et al. *The plasma boundary of magnetic fusion devices*. Vol. 224. 2000.

[139] E. Delabie. "The relation between divertor conditions and the L–H threshold on JET," *42nd EPS Conference on Plasma Physics*. 2015.

[140] S. Potzel. "Private comunication."

[141] S. Potzel et al. "On the fluctuating detachment state at ASDEX Upgrade," *40th EPS Conference on Plasma Physics, Espoo, Finland*. 2013.

[142] F. Ryter et al. "Survey of the H-mode power threshold and transition physics studies in ASDEX Upgrade", *Nucl. Fusion* 53, 11 (2013), p. 113003. ISSN: 0029-5515.

[143] JFT-2M Group, *3rd H-mode Workshop Vol. 1*. 1991.

[144] P. Gohil et al. "L–H transition studies on DIII-D to determine H-mode access for operational scenarios in ITER", *Nucl. Fusion* 51, 10 (2011), p. 103020.

[145] J. Connor et al. "Scaling laws for plasma confinement", *Nucl. Fusion* 17, 5 (1977), p. 1047.

[146] P. Hennequin et al. "Comprehensive experimental study of plasma turbulence structure and its scaling with ρ^*", *submitted to Plasma Phys. and Contr. Fusion* (2016).

[147] L. Schmitz et al. "H-mode transition dynamics; role of flow-turbulence interaction," *15th International workshop on H-mode physics and transport barriers*. 2015.

[148] Y. Xu et al. "Isotope Effect and Multiscale Physics in Fusion Plasmas", *Phys. Rev. Lett.* 110, (2013), p. 265005.

[149] J. Cordey et al. "Plasma confinement in JET H–mode plasmas with H, D, DT and T isotopes", *Nuclear Fusion* 39, 3 (1999), p. 301.

[150] F. Ryter et al. "L-H transition physics in hydrogen and deuterium: key role of the edge radial electric field and ion heat flux", *Plasma Phys. and Contr. Fusion* 58, 1 (2016), p. 014007.

[151] M. Willensdorfer et al. "Electron density evolution after L–H transitions and the L–H/H–L cycle in ASDEX Upgrade", *Nucl. Fusion* 52, 11 (2012), p. 114026.

[152] K. H. Burrell et al. "Physics of the L to H transition in the DIII-D tokamak", *Phys. of Fluids B* 2, 6 (1990), pp. 1405–1410.

[153] P. Gohil et al. "The phenomenology of the L-H transition in the DIII-D tokamak", *Nucl. Fusion* 34, 8 (1994), p. 1057.

[154] K. H. Burrell et al. "Role of the radial electric field in the transition from L (low) mode to H (high) mode to VH (very high) mode in the DIII-D tokamak", *Phys. of Plasmas* 1, 5 (1994), pp. 1536–1544.

[155] K. H. Burrell et al. "Constraints on theories provided by fast time response measurements across the L to H transition on DIIID", *Plas. Phys. and Cont. Fusion* 38, 8 (1996), p. 1313.

[156] T. Estrada et al. "Spatiotemporal Structure of the Interaction between Turbulence and Flows at the L-H Transition in a Toroidal Plasma", *Phys. Rev. Lett.* 107, (2011), p. 245004.

[157] A. Lotka. "Contribution to the Theory of Periodic Reaction", *J. Phys. Chem.* 14, 217-274 (1910).

[158] G. M. Staebler et al. "H-mode transitions and limit cycle oscillations from mean field transport equations", *Plasma Phys. and Contr. Fusion* 57, 1 (2015), p. 014025.

[159] P. Manz et al. "Poloidal asymmetric flow and current relaxation of ballooned transport during I-phase in ASDEX Upgrade", *in preparation for Physics of Plasmas* (2016).

[160] D. Constantinescu et al. "A low-dimensional model system for quasi-periodic plasma perturbations", *Phys. of Plasmas* 18, 6, 062307 (2011).

[161] I. Cziegler et al. "Zonal flow production in the L–H transition in Alcator C-Mod", *Plasma Phys. and Contr. Fusion* 56, 7 (2014), p. 075013.

[162] G. Tynan et al. "Turbulent-driven low-frequency sheared ExB flows as the trigger for the H-mode transition", *Nucl. Fusion* 53, 7 (2013), p. 073053.

[163] L. Chôné et al. “L-H transition dynamics in fluid turbulence simulations with neoclassical force balance”, *Phys. of Plasmas* 21, 7 (2014), p. 070702. ISSN: 1070-664X.

[164] X. Wu et al. “One-dimensional modelling of limit-cycle oscillation and H-mode power scaling”, *Nucl. Fusion* 55, 5 (2015), p. 053029.

[165] G. D. Conway et al. “Amplitude behaviour of geodesic acoustic modes in the ASDEX Upgrade tokamak”, *Plasma Phys. and Contr. Fusion* 50, 8 (2008), p. 085005.

[166] L. Wang et al. “Electromagnetic effects of kinetic geodesic acoustic mode in tokamak plasmas”, *Phys. of Plasmas* 18, 5, 052506 (2011).

[167] D. Hill et al. “DIII-D research towards resolving key issues for ITER and steady-state tokamaks”, *Nucl. Fusion* 53, 10 (2013), p. 104001.

[168] A. Nielsen et al. “Simulation of transition dynamics to high confinement in fusion plasmas”, *Physics Letters A* 379, 47-48 (2015), pp. 3097–3101. ISSN: 0375-9601.

[169] Z. Yan et al. “Observation of the L–H Confinement Bifurcation Triggered by a Turbulence-Driven Shear Flow in a Tokamak Plasma”, *Phys. Rev. Lett.* 112, (2014), p. 125002.

[170] L. Schmitz et al. “Connecting Microscopic L-H Transition Physics to the Power Threshold,” *EPS*. 2015.

[171] P. Manz et al. “Zonal flow triggers the L-H transition in the Experimental Advanced Superconducting Tokamak”, *Physics of Plasmas (1994-present)* 19, 7, 072311 (2012).

[172] G. R. Tynan et al. “Recent progress towards a physics-based understanding of the H-mode transition”, *Plasma Physics and Controlled Fusion* 58, 4 (2016), p. 044003.

[173] S. Klenge. “Dynamik magnetisch eingeschlossener Plasmen am L-H Übergang : Untersuchung mit Hilfe von Doppler-Reflektometrie im Tokamak ASDEX Upgrade.” ger. PhD thesis. Holzgartenstr. 16, 70174 Stuttgart: Universität Stuttgart, 2005. ISBN: 3-933893-36-4.

[174] A. Medvedeva et al. “Density fluctuations measurements with an ultra-fast-swept reflectometer in ASDEX Upgrade,” Proc. 12$^{\text{th}}$ International Reflectometry Workshop, 2015.

[175] J. Kinsey et al. "ITER predictions using the GYRO verified and experimentally validated trapped gyro-Landau fluid transport model", *Nucl. Fusion* 51, 8 (2011), p. 083001.

[176] M. R. Wade et al. "Edge impurity dynamics during an edge-localized mode cycle on DIII-D", *Phys. Plasmas* 12, 5 (2005), p. 056120. ISSN: 1070664X.

[177] T. Pütterich et al. "ELM flushing and impurity transport in the H-mode edge barrier in ASDEX Upgrade", *Journal of Nuclear Materials* 415, 1, Supplement (2011), S334–S339. ISSN: 0022-3115.

[178] H. Meyer et al. "L-H transition and pedestal studies on MAST", *Nucl. Fusion* 51, 11 (2011), p. 113011.

[179] P. A. Schneider et al. "Observation of different phases during an ELM crash with the help of nitrogen seeding", *Plasma Physics and Controlled Fusion* 56, 2 (2014), p. 025011.

[180] J. Neuhauser et al. "Transport into and across the scrape-off layer in the ASDEX Upgrade divertor tokamak", *Plasma Physics and Controlled Fusion* 44, 6 (2002), p. 855.

[181] A. Burckhart et al. "Inter-ELM behaviour of the electron density and temperature pedestal in ASDEX Upgrade", *Plasma Physics and Controlled Fusion* 52, 10 (2010), p. 105010.

[182] T. Pütterich et al. "Evidence for Strong Inversed Shear of Toroidal Rotation at the Edge-Transport Barrier in the ASDEX Upgrade", *Phys. Rev. Lett.* 102, (2009), p. 025001.

[183] F. M. Laggner et al. "High frequency magnetic fluctuations correlated with the inter-ELM pedestal evolution in ASDEX Upgrade", *accepted for pubblication in Plasma Phys. and Cont. Fusion* (2016).

[184] R. M. McDermott et al. "Edge radial electric field structure and its connections to H-mode confinement in Alcator C-Mod plasmas", *Physics of Plasmas* 16, 5, 056103 (2009).

[185] J. Kim et al. "Rotation characteristics of main ions and impurity ions in H -mode tokamak plasma", *Phys. Rev. Lett.* 72, (1994), pp. 2199–2202.

Acknowledgments

This work is the result of the effort and the ideas of many people. The most important outcome of the last three years was, for me, to meet all of them.

I firstly would like to thank my academic supervisor Prof. Ulrich Stroth who enabled this work. His interest and expertise on the topic of this thesis were for me a great source of motivation.

Dr. Thomas Pütterich has guided me throughout the whole thesis. I am most grateful to him for being there to answer my questions and to discuss my results. I really appreciated to have someone who spotted the weaknesses of my analysis. I wish to extend my gratitude to Dr. Eleonora Viezzer. I will be always in debt to her for the unconditional support she never stopped to give to me.

I would like to thank the whole spectroscopy group, especially Dr. Benedikt Geiger, Dr. Rachael McDermott, Dr. Athina Kappatou and Alexander Lebschy. Special thanks go to my group leader Dr. Ralph Dux who developed the new spectrometer and helped me in understanding how visible spectroscopy works.

I would also like to thank Dr. François Ryter and Dr. Elisabeth Wolfrum whose ideas were the foundations of this work. I would like to extend my thanks to Dr. Gregor Birkenmeier for the enormous time he spent with me in comparing our analysis to any other paper around.

I am gratful to Dr. Tim Happel, Dr. Gerrard Conway and Dr. Pascal Hennequin who introduced me to the world of turbulence and Doppler reflectometry. Furthermore, I want to express my appreciation to Florian Laggner and Dr. Rainer Fischer for providing extremely sophisticated electron and density profiles.

The design and installation of the new diagnostics would have never be possible without the help of Wolfgang Zeidner, Michael Rolffs, Andreas Bolland and Bertram Brucker. Special thanks to Sven Martinov, Helmut Blank, Roland Merkel who helped in the installation and maintenance of the computers.

I would also like to extend my appreciation to Dr. Peter Manz, Dr. Matthias Willensdorfer, Dmitrii Prisiazhniuk, Anna Medvedeva, Dr. Steffen Potzel, Dr. Mike Dunne, Alexander Bock, Dr. Andreas Burckhart and Dr. Hendrik Meyer for their input and contributions to this work.

Finally, I would like to thank the whole IPP staff and in particular the (PhD) students for their continuous help and for the nice working atmosphere. In particular, I am grateful to my office mates Alexander Lebschy, Florian Laggner, Dmitrii Prisiazhniuk, Anna Medvedeva, Dr. Sina Fietz, Dr. Mike Dunne and Ivan Paradela Perez. They were always ready to help me, to have a relaxed chat, to play darts or eventually to eat bakery products. Thank you for the time we spent together.